Investigation of Structure and Li Dynamics in New Li Ion Conductors using Solid State NMR Spectroscopy

Thesis submitted in accordance with the requirements of the University of Liverpool for the degree of Master of Philosophy by Kenneth Kazuya Inglis

May 2020

Investigation of Structure and Li Dynamics in New Li Ion Conductors using Solid State NMR Spectroscopy

Kenneth Kazuya Inglis

Abstract

Developing solid state ionic conductors to replace liquid electrolytes for next generation Li^+ ion battery technologies are of high interest due to their major impact resulting from the combination of increased safety, lifetime and power output. Potential candidates are constantly studied by research groups worldwide to obtain such material, however issues such as electrochemical stability with lithium and low ionic conductivity hinder the target to be achieved.

Solid state nuclear magnetic resonance (NMR) spectroscopy is an invaluable technique in solid state ionic conductor research with its ability to investigate both local structure and follow the dynamics of the charge carrier. It has been used widely to identify Li^+ dynamics and diffusion pathways on time scales inaccessible by other experimental techniques, allowing deeper understanding in what key features are present in achieving high performance Li^+ ion conductors.

In this thesis, the solid state NMR investigation of three Li^+ ion conductors from three distinct crystallographic families are reported.

1. A new class of ABO_3 perovskite with composition $La_3Li_3W_2O_{12}$ is identified, it is the first perovskite material where Li is present on both A- and B-sites. Solid state NMR deduced the ratio of the two sites as 1:2, consistent with DFT calculations. The activation barrier for Li^+ diffusion between neighbouring sites was found to be ~0.29 eV and is comparable to the best oxide based Li^+ ion conductors reported.

2. The effect of Ca^{2+} doping in the NASICON Li^+ ion conductor $LiTaAl(PO_4)_3$ to increase Li^+ content was studied. Doping resulted in slower Li^+ dynamics compared to the undoped material with significantly higher activation barrier to Li^+ diffusion. The anisotropic nature of the thermal expansion of the NASICON framework and Li^+ diffusion are also observed by variable temperature ^7Li NMR spectroscopy.

3. A new structural family of sulfide Li^+ ion conductors with compositions $Li_{4.4}Al_{0.4}Ge_{0.6}S_4$ and $Li_{4.4}Al_{0.4}Sn_{0.6}S_4$ were identified. These new phases consisted of a two-dimensional Li^+ diffusion pathway with activation barriers as low as ~0.17 eV, similar to the $Li_{10}GeP_2S_{12}$ family, the best solid state sulfide Li^+ ion conductor series reported.

These findings signify the importance of solid state NMR as a technique complementary to other methods to understanding the properties of newly synthesised phases.

Acknowledgements

I would first like to acknowledge both my PhD supervisors Prof. Matthew J. Rosseinsky and Dr. Frédéric Blanc for giving me the opportunity for my PhD and extremely helpful guidance throughout its duration. I am especially grateful to Frédéric for his patience, encouragement and immense knowledge in the field of research, helping me grow as a researcher, along with giving me the opportunities to present my work at both national and international conferences.

I would also like to express my appreciations to the research coordinators in the Rosseinsky group, especially Dr. Michael J. Pitcher and Dr. Matthew S. Dyer, for very fruitful discussions over the years for various research projects.

I would also like to thank all the facility managers and researchers I have collaborated with, especially the following people: Dr. Dinu Iuga (The UK 850 MHz Solid State NMR Facility, Warwick), Dr. Aydar Rakhmatullin and Prof. Pierre Florian (CEMTHI-CNRS, Orléans).

Special gratitude is required for the researchers in the Blanc group, for constant motivation, discussion and encouragement over the years.

Finally, I would like to thank my friends and family who have supported me throughout my PhD studies.

Table of Contents

18 D. Lin, Y. Liu and Y. Cui, *Nat. Nanotechnol.*, 2017, **12**, 194–206.

19 M. K. Y. Chan, C. Wolverton and J. P. Greeley, , DOI:10.1021/ja301766z.

20 B. A. Boukamp, G. C. Lesh and R. A. Huggins, *J. Electrochem. Soc.*, 1981, **128**, 725.

21 B. Hertzberg, A. Alexeev and G. Yushin, *J. Am. Chem. Soc.*, 2010, **132**, 8548–8549.

22 P. . Stallworth, J. . Fontanella, M. . Wintersgill, C. D. Scheidler, J. J. Immel, S. . Greenbaum and A. . Gozdz, *J. Power Sources*, 1999, **81**–**82**, 739–747.

23 J. Y. Song, Y. Y. Wang and C. C. Wan, *J. Electrochem. Soc.*, 2000, **147**, 3219.

24 S. S. Zhang, *J. Power Sources*, 2006, **162**, 1379–1394.

25 N. Kamaya, K. Homma, Y. Yamakawa, M. Hirayama, R. Kanno, M. Yonemura, T. Kamiyama, Y. Kato, S. Hama, K. Kawamoto and A. Mitsui, *Nat. Mater.*, 2011, **10**, 682–686.

26 S. S. Zhang, *J. Power Sources*, 2007, **164**, 351–364.

27 D. B. McWhan, S. J. Allen, J. P. Remeika and P. D. Dernier, *Phys. Rev. Lett.*, 1975, **35**, 953–956.

28 S. Stramare, V. Thangadurai and W. Weppner, *Chem. Mater.*, 2003, **15**, 3974–3990.

29 P. Knauth, *Solid State Ionics*, 2009, **180**, 911–916.

30 A. B. Santibáñez-Mendieta, C. Didier, K. K. Inglis, A. J. Corkett, M. J. Pitcher, M. Zanella, J. F. Shin, L. M. Daniels, A. Rakhmatullin, M. Li, M. S. Dyer, J. B. Claridge, F. Blanc and M. J. Rosseinsky, *Chem. Mater.*, 2016, **28**, 7833–7851.

1. Introduction

Lithium ion batteries are widely used in a variety of areas including portable devices such as mobile phones to electric vehicles. Commercial batteries currently in use contain organic liquid-state electrolytes, where the lithium incorporated polymers are dispersed in organic solvents or ionic liquids, which consists of many disadvantageous factors. During charge or discharge of the battery, the lithium salt in the electrolyte react with Li metal electrodes, forming a thin film on the Li surface. These films break off and Li dendrites are deposited in the solution.[1] These dendrites lead to batteries short circuiting, and combining this with the severely flammable materials used, this increases the possibility of massive harm caused to the user. Therefore, the importance of replacing these liquid electrolytes is high for user safety. One of the alternatives proposed is to replace the liquid electrolytes in favour of lithium conducting solid ceramics. These solid-state Li^+ ion conductors are growing rapidly in interest not only for their reduction of handling flammable and toxic materials, but also with the increase in lifetime, higher power outputs and energy densities.[2]

1.1 Lithium Ion Batteries

Lithium ion batteries consists of three main components – an anode, a cathode and an electrolyte (Figure 1.1). The two electrodes – the anode and cathode – are connected by an external circuit and are separated by the electrolyte. During discharge, the Li inside the anode are oxidised and released into the electrolyte. The Li^+ ions travel through the electrolyte towards the cathode, where it is incorporated. As the Li^+ ion travels, a current is passed

through an external circuit connecting the electrodes. During charge, the Li^+ ions are released from the cathode and back into the anode. The mobility of the ion is much smaller than the electronic conductivity in metals, which is compensated by using large electrodes separated by a thin electrolyte.[3]

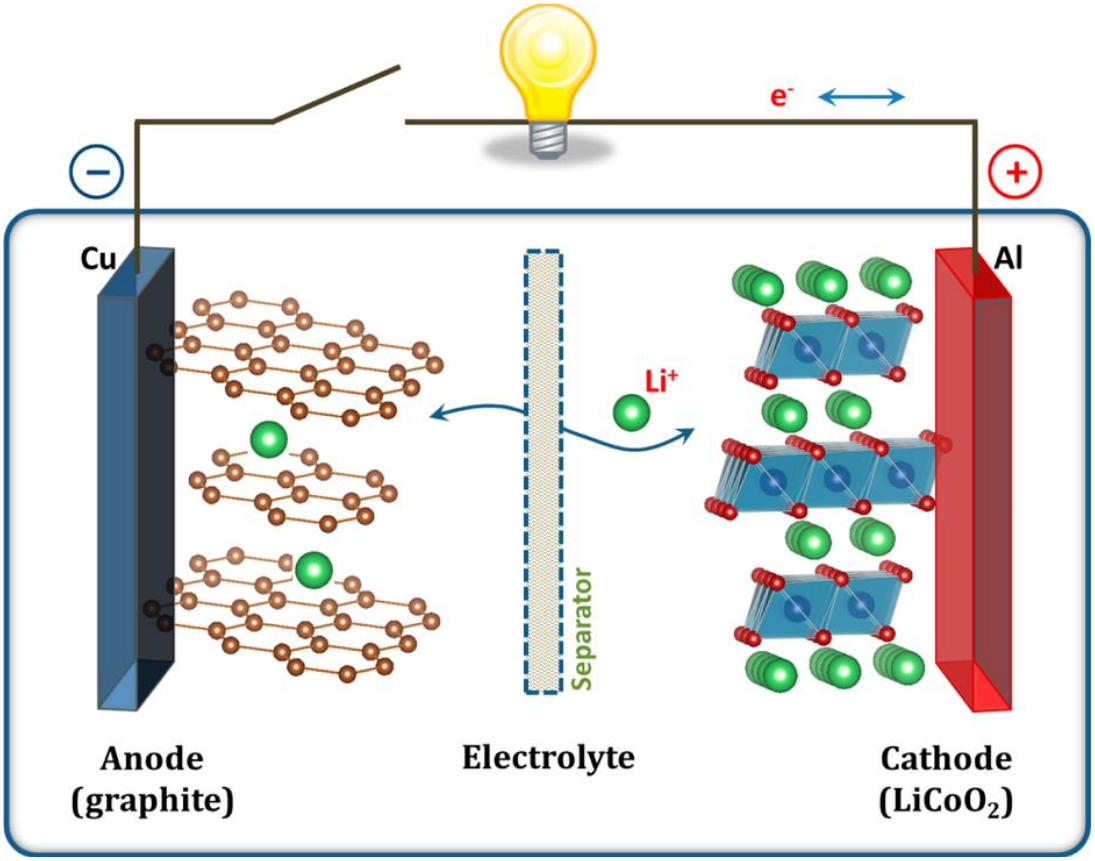

Figure 1.1. Schematic illustration of a liquid-state Li^+ ion battery. Figure reprinted with permission from Goodenough and Park, *J. Am. Chem. Soc.*, **2013,** *135*, 1167–1176.[3] Copyright 2013 American Chemical Society.

1.2 Cathodes

The cathode is the positive electrode and incorporates cations during discharge to stabilise its structure. Cathodes are often intercalation compounds containing transition metals to enable structural integrity during Li^+ ion charge/discharge between itself and the electrolyte. The most common

cathode used commercially is $LiCoO_2$ (Figure 1.2a).

$LiCoO_2$ has a layered structure consisting of edge sharing CoO_6 layers with lithium ions in between each layer and is commonly used with its high electrochemical potential of 4.2 V vs. Li/Li^+ and cycle stability.[4,5] Although the theoretical capacity of $LiCoO_2$ is 274 mAh g^{-1}, the actual capacity is low at around 130 mAh/g, as the lower threshold of delithiation is $Li_{0.5}CoO_2$. If further delithiation is attempted, the structure changes and capacity is lost.[4]

Other cathode materials such as the spinel $LiMn_2O_4$ are also used (Figure 1.2b). $LiMn_2O_4$ consists of mixed valent edge sharing MnO_6 octahedra containing both Mn^{3+} and Mn^{4+} ions (sometimes labelled as $Mn^{3.5+}$ as they occupy the same site in equal amounts), with Li^+ in the tetrahedral site and after full delithiation, it becomes MnO_2 of the same structure.[6,7] $LiMn_2O_4$ has higher initial capacity compared to $LiCoO_2$ at 148 mAh/g when synthesised at 800 ^oC, but diminishes after cycling. Synthesis of $LiMn_2O_4$ at different temperatures give lower capacitance, highlighting its temperature sensitive nature.[8]

$LiFePO_4$ (Figure 1.2c) is another cathode material used widely in Li^+ ion battery application since its discovery of reversible Li^+ insertion and extraction.[9,10] Its high theoretical capacitance of 170 mAh/g and ordered olivine crystal structure consisting of corner sharing FeO_6 octahedra and PO_4 tetrahedra with edge sharing LiO_6 octahedra, making it an attractive material for use as a cathode. However, its low electrochemical potential of ~3.4 V vs. Li^+ and sharp decline in reversible capacity at high charge/discharge rates gives $LiFePO_4$ limited application in commercial usage compared to $LiCoO_2$.[11]

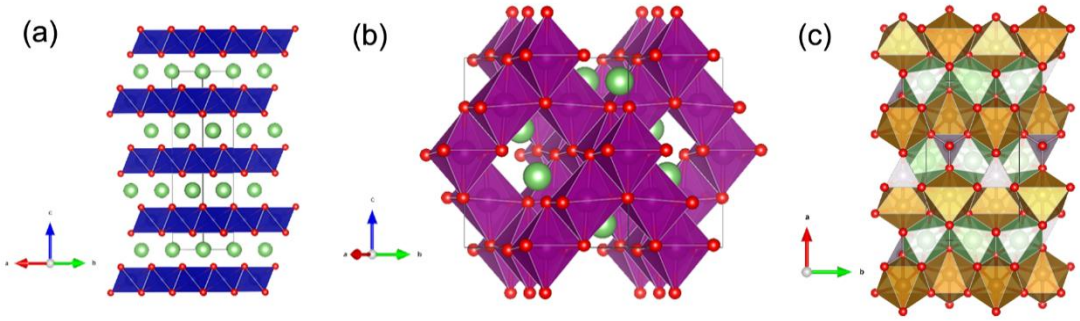

Figure 1.2. Crystal structure of (a) $LiCoO_2$, (b) $LiMn_2O_4$ and (c)$LiFePO_4$. The structural models are taken from Holzapfel *et al*.,[12] Berg *et al*.[13] and Amador *et al.*,[14] respectively and is plotted with VESTA.[15] Atom colours: Green – Li, Blue – Co, Purple – Mn, Brown – Fe, Lilac – P, Red – Oxygen. Grey lines denote the unit cell of the crystal structure.

1.3 Anodes

Anodes are the negative electrode in a battery. These materials incorporate and release Li^+ ions during charge and discharge cycles, and be a good electronic conductor to enable electron transport between the external circuit and the Li^+ ions. The performance of an anode is determined by its cycling capabilities and is closely related to the rate of Li^+ self diffusion in the material.

The ideal choice for anodes would be Li metal which has the highest Li capacity and low density; however the formation of Li dendrites during cycling can cause short circuits and start a thermal runaway reaction on the cathode which ultimately causes the battery cell to combust.[16–18] These safety hazards are critical problems which restricts the application of Li metal and other anode materials are therefore required.

Many anode materials are carbon-based consisting of graphite or

honeycomb based structures. One of the most commonly used anode materials is graphite-based with a theoretical capacity of 372 mAh g^{-1} and a general composition of LiC_6 when fully lithiated. There are two main advantages in graphene anodes: 1. its low change in size between fully lithiated and delithiated states, enabling use in a variety of batteries,[1] 2. low delithiation potential required for anode operation.[17] These properties make it an ideal choice for use as an anode.

Ceramic materials are also researched as safer and less toxic alternatives to carbon-based anodes. One example is silicon-based materials which have extremely high specific capacity – a factor of 10 larger compared to carbon-based anodes.[17,19] The problem arises on the large change of volume through Li insertion and the loss of capacity through cycling with the various Li_xSi_y compositions,[20,21] which makes it an unfavourable choice as an anode.

1.4 Electrolytes

Electrolytes are the component in between the two electrodes. It must have high ionic conductivity to allow transport of Li^+ ions between the electrodes, have no electronic conductivity to avoid self-discharge and be chemically stable against both electrodes to avoid degradation of the battery cell. They are split into two groups – liquid and solid.

1.4.1 Liquid State Lithium Electrolytes

The most commonly used Li^+ ion electrolyte is liquid-based. Li^+ ion transport in liquid electrolytes involve moving solvated Li^+ ions in a solvent

medium where the potential energy required for ion transport is considered to be flat due to fast salt/solvent ion exchange (Figure 1.3a).[2] The conductivity of these electrolytes are enhanced by increasing the number of mobile Li^+ ions as well as decreasing the viscosity of the medium. One such example of a liquid electrolyte is a mixture of a Li salt, such as $LiPF_6$, dissolved in a mixed organic solution, such as a 50:50 vol% ratio ethylene carbonate–propylene carbonate mixture.[22] Often, polymerised additives such as polyvinylidene fluoride is added to increase safety during operation.[23–25] A porous polymeric layer consisting of polyethylene and/or polypropylene are also added in liquid electrolytes as a separator layer to avoid contact between the anode and cathode. The pore sizes of these separators are smaller than the particle sizes of the electrodes, while allowing Li^+ ions to travel through. They also contain shut down mechanisms to prevent thermal runaway reactions at temperatures below the melting point of the polymers to prevent loss in mechanical integrity which would lead to electrodes coming into contact.[26] These electrolytes have high ionic conductivity of 10^{-2} S cm^{-1} at room temperature and are ideal for use in batteries.

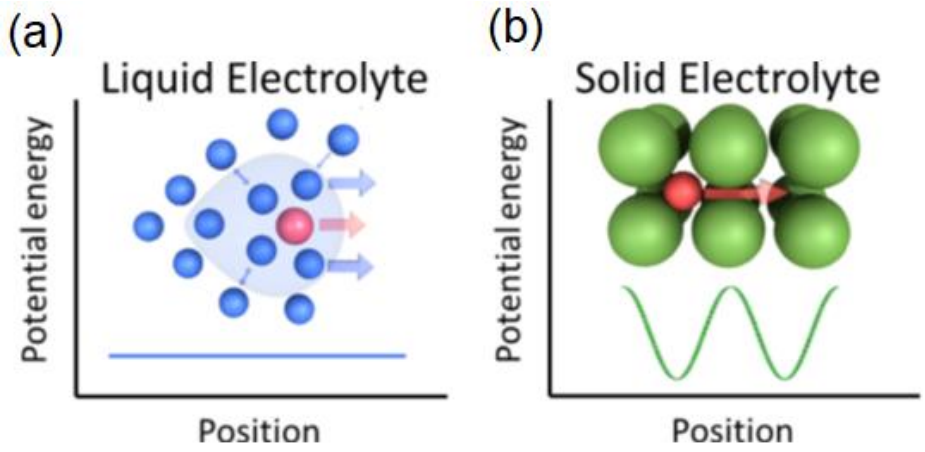

Figure 1.3. Potential energy of Li^+ migration within (a) a liquid electrolyte and (b) a solid electrolyte. Red sphere denotes the mobile Li^+ ion. Figure reprinted

with permission from Bachman *et al*., *Chem. Rev.*, **2016,** *116*, 140–162.[3] Copyright 2016 American Chemical Society.

1.4.2 Solid-State Lithium Electrolytes

Even with the inclusion of a flame retardant material, the organic mixture used to dissolve the Li salt is toxic and not completely non-flammable. One approach to approach this issue is to replace the liquid electrolyte with solid-state ceramics which do not contain flammable content. These solid-state Li^+ ion conducting materials are also said to have other major advantages over liquid electrolytes, including higher Li^+ ion transfer number, increased battery life and stability.[2] These benefits also give opportunities to redesign the current battery cell by minimising or removing the current fail-safe measures.

One of the most challenging aspect for development of solid-state conductors is its low Li^+ ion conductivity at room temperature whilst negating the electron conductivity, with many materials having conductivities magnitudes lower than their liquid counterparts (10^{-2}–10^{-4} S cm^{-1}),while those that have similar conductivities to liquids are unstable against Li metal.[2] Mobile Li^+ ions in solid state electrolytes must pass through periodic “bottlenecks” to move between two energy minima, i.e. the crystallographic Li sites, which pose an energetic barrier (Figure 1.3b). The ion must overcome this energy barrier with an activation energy (E_a) for migrate between two sites. The activation energy and ion conductivity of solid state electrolytes are determined by the defect chemistry of the material, e.g. the number of interstitial sites, vacancies and partial occupancies of the sites.

1.4.2.1 **Crystallographic Defects**

Defects in crystallographic materials are known as point defects, i.e. a point that disturbs the ideal structure. These point defects formed when an atom deviates from its ideal position are defined as intrinsic defects, such as Frenkel and Schottky defects, or by aliovalent ion substitution, known as extrinsic defects (Figure 1.4).

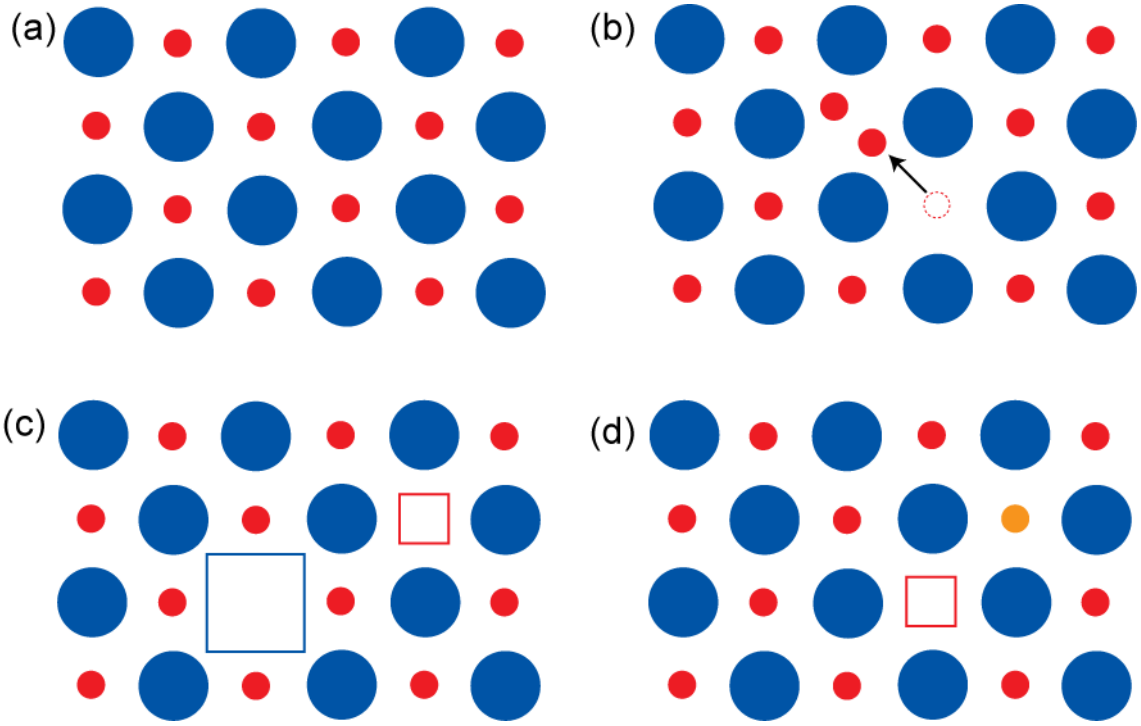

Figure 1.4. (a) The ideal crystal structure of a rocksalt. (b) A rocksalt crystal structure with a Frenkel defect. (c) A rocksalt crystal structure with a Schottky defect. (d) A rocksalt crystal structure with aliovalent substitution of the cation. Atoms colours: +1 charge cation (red), +2 charge cation (orange), -1 charge anion (blue). Filled symbols denote occupied sites, dotted circle denotes the vacant site due to migration of the cation (arrow), empty squares denotes vacant site due to missing ions.

Frenkel defects, also known as a dislocation defect, arises when an atom in a crystalline material dislocates to an interstitial site, leaving its own lattice site vacant. This effect occurs when the size of the cation is substantially smaller than the anions and are usually found in materials such as ZnS and Ag-halide series. Schottky defects are formed by missing ions in their lattice sites. These vacancies are formed in stoichiometric amounts, to keep charge balance of the material. These defects form when the size difference between cation and anions are small and can be observed in NaCl, KCl and KBr.

Extrinsic defects are formed by aliovalent substitution of an atom in the structure with a foreign atom. The charge difference is then compensated by a change in ion concentration forming defects such as vacancies or interstitial sites, i.e. multiple atoms sharing a single site.

1.4.2.2 **Ion Conductivity**

Li^+ ion conduction in solid state electrolytes are mediated by Li^+ ions migrating to the neighbouring defect site in the structure. Defects in Li^+ ion conductors are often formed by aliovalent substitution of ions rather than using intrinsic defects, as the number of defects formed by intrinsic effects are extremely low compared to the number possible by extrinsic means. Aliovalent substitution would be tuned to increase the number of mobile Li^+ ions, by means of introducing interstitial Li^+ sites or increasing vacant sites, which in turn increasing the conductivity of the material. Attempting to increase the conductivity with this approach, however, may reduce the overall conductivity as the increased Li^+ ions interact with the surrounding lattice or local distortion of the crystal structure.[2,27] The choice of cation is also important, as observed

in the $La_{2/3-x}Li_{3x}TiO_3$ family, where Ti^{4+} reduces to Ti^{3+} when in contact with Li metal,[28,29] introducing electronic conductivity. Therefore, care must taken when creating defects in the crystal structure to obtain the optimum Li^+ ion concentration and high ionic conductivity.

1.5 Aims of the Thesis

In order to develop safe and high power next generation Li^+ ion batteries, all of the components in a battery cell must be researched. The cathode must have high capacity and high Li/Li^+ electrochemical potential, the anode must have high capacity with high stability and fast Li^+ diffusion, and electrolytes must have negligible electrical conductivity with comparable ionic conductivity to liquid electrolytes with values of 10^{-2} S cm^{-1}. This thesis focuses on newly developed solid state Li^+ ion electrolytes synthesised by researchers in the Rosseinsky group. These new electrolytes are studied using solid-state nuclear magnetic resonance (NMR) for its ability to identify their local structure and measure their Li^+ dynamic properties at multiple time scales to identify the best candidate for use in batteries.

Chapter 2 discusses the theory behind NMR experimental methods and its application to measure Li^+ ion diffusion.

Chapter 3 consists of a literature review of the main families of solid Li^+ ion conductors. The background of each crystal structure and their solid state NMR studies will be discussed, followed by a brief description on the properties required for battery application.

Chapter 4 contains the NMR studies on $La_3Li_3W_2O_{12}$, the first perovskite material where Li is present on both the A-site and B-site of the crystal

structure. This chapter is based on the paper "$La_3Li_3W_2O_{12}$: Ionic Diffusion in a Perovskite with Lithium on both A- and B-Sites" by A. Santibáñez-Mendieta *et al.*, published in *Chemistry of Materials* in 2016.[30]

Chapter 5 contains the solid state NMR studies on two new NASICON compounds $Li_{0.925}Ta_{1.062}Al_{0.938}P_{3.16}O_{12+x}$ and $Li_{0.734}Ta_{1.187}Ca_{0.108}Al_{0.705}P_3O_{12}$, synthesised by Dr. Chris Collins and Dr. Leopoldo Enciso-Maldonado in the Rosseinsky group. Details regarding synthesis procedures, diffraction and AC impedance data are available in Dr. Leopoldo Enciso-Maldonado's thesis.[31]

Chapter 6 consists of the NMR studies of two new sulphide conductors $Li_{4.4}Al_{0.4}Ge_{0.6}S_4$ and $Li_{4.4}Al_{0.4}Sn_{0.6}S_4$. These phases were found to be stable against Li metal, with no significant changes to the diffraction patterns measured before and after testing. This chapter is based on the paper "Lithium transport in $Li_{4.4}M_{0.4}M'_{0.6}S_4$ (M= Al^{3+}, Ga^{3+} and M'= Ge^{4+}, Sn^{4+}): Combined crystallographic, conductivity, solid state NMR and computational studies" by B. Leube *et al.*, published in *Chemistry of Materials* in 2018.[32]

1.6 References

1 D. Aurbach, E. Zinigrad, Y. Cohen and H. Teller, *Solid State Ionics*, 2002, **148**, 405–416.

2 J. C. Bachman, S. Muy, A. Grimaud, H.-H. Chang, N. Pour, S. F. Lux, O. Paschos, F. Maglia, S. Lupart, P. Lamp, L. Giordano and Y. Shao-Horn, *Chem. Rev.*, 2016, **116**, 140–162.

3 J. B. Goodenough and K. S. Park, *J. Am. Chem. Soc.*, 2013, **135**, 1167–1176.

4 M. S. Whittingham, *Chem. Rev.*, 2004, **104**, 4271–4301.

5 V. Etacheri, R. Marom, R. Elazari, G. Salitra and D. Aurbach, *Energy Environ. Sci.*, 2011, **4**, 3243.

6 P. G. Bruce, *Chem. Commun.*, 1997, 1817.

7 R. J. Gummow, A. de Kock and M. M. Thackeray, *Solid State Ionics*, 1994, **69**, 59–67.

8 W. Liu, K. Kowal and G. C. Farrington, *J. Electrochem. Soc.*, 1998, **145**, 459–465.

9 A. K. Padhi, K. S. Nanjundaswamy and J. B. Goodenough, *J. Electrochem. Soc.*, 1997, **144**, 1188–1194.

10 K. Zaghib, A. Guerfi, P. Hovington, A. Vijh, M. Trudeau, A. Mauger, J. B. Goodenough and C. M. Julien, *J. Power Sources*, 2013, **232**, 357–369.

11 R. Malik, A. Abdellahi and G. Ceder, *J. Electrochem. Soc.*, 2013, **160**, A3179–A3197.

12 M. Holzapfel, C. Haak and A. Ott, *J. Solid State Chem.*, 2001, **156**, 470–479.

13 H. Berg, J. O. Thomas, W. Liu and G. C. Farrington, *Solid State Ionics*, 1998, **112**, 165–168.

14 O. García-Moreno, M. Alvarez-Vega, J. García-Jaca, J. M. Gallardo-Amores, M. L. Sanjuán and U. Amador, *Chem. Mater.*, 2001, **13**, 1570–1576.

15 K. Momma and F. Izumi, *J. Appl. Crystallogr.*, 2011, **44**, 1272–1276.

16 W. Xu, J. Wang, F. Ding, X. Chen, E. Nasybulin, Y. Zhang and J. G. Zhang, *Energy Environ. Sci.*, 2014, **7**, 513–537.

17 N. Nitta, F. Wu, J. T. Lee and G. Yushin, *Mater. Today*, 2015, **18**, 252–264.

31 L. Enciso-Maldonado, University of Liverpool, 2017.

32 B. T. Leube, K. K. Inglis, E. J. Carrington, P. M. Sharp, J. F. Shin, A. R. Neale, T. D. Manning, M. J. Pitcher, L. J. Hardwick, M. S. Dyer, F. Blanc, J. B. Claridge and M. J. Rosseinsky, *Chem. Mater.*, 2018, **30**, 7183–7200.

2. Nuclear Magnetic Resonance and its use in Lithium Diffusion

In this section, the principles of nuclear magnetic resonance spectroscopy will be introduced, followed by the techniques used in the thesis to identify local environments and Li^+ dynamics of Li^+ ion conductors. All NMR experiments which are stated in this chapter and performed in this thesis are done solely by the author.

2.1 Nuclear Magnetic Resonance (NMR) Spectroscopy[1,2]

2.1.1 Basics of NMR

Nuclear magnetic resonance (NMR) spectroscopy is a very powerful and versatile technique used in a variety of research fields for local structure investigation, utilising the interactions between the nucleus' magnetic moment μ and the external magnetic field B_0. Magnetic moments occur in nuclei with the intrinsic property of angular momentum, which are referred to as nuclear spin. The magnetic moment of a nucleus is proportional to its gyromagnetic ratio γ and spin quantum number I, both which are nuclei dependent.

For NMR use, the studied nuclei must be "NMR active"; i.e. have a non-zero nuclear spin. Outside of a magnetic field, the magnetic moments are oriented randomly in all directions. When the nucleus is placed in a magnetic field B_0, the magnetic moments orient either with or against the magnetic field due to the Zeeman effect, and form $2I+1$ spin states while rotating around the B_0 axis at the Larmor frequency ν_0. The energy difference ΔE between the spin states are defined as:

$$\Delta E = h\upsilon_0 = \frac{h\gamma B_0}{2\pi} \qquad (2.1)$$

where γ is the gyromagnetic ratio of the nuclei (rad s^{-1} T^{-1}), h is the Planck constant and B_0 is the strength of the magnetic field the nuclei are affected by (henceforth external magnetic field). In a nuclei with a spin of ½, the spin state where the nuclei spins aligns and opposes the magnetic field is defined as the α and β state, respectively.

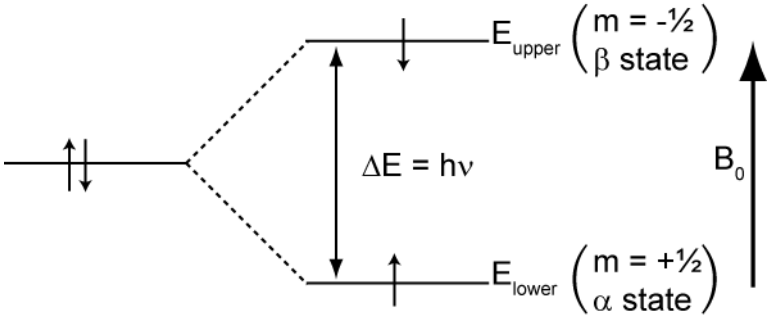

Figure 2.1. Relative energy levels of a spin ½ nuclei. The energy levels are split when the sample is placed in an external magnetic field B_0 by energy ΔE..

In an actual sample placed in a magnetic field, the number of spins is far larger, which must be taken into consideration. When multiple spins are placed into a magnetic field, the spins will align with or against the field and the distribution of the spins will reach a thermal equilibrium established using the Boltzmann equation:

$$\frac{N_\beta}{N_\alpha} = e^{-\Delta E/k_B T} \qquad (2.2)$$

where N_x is the number of spins in spin state *x*, k_B is the Boltzmann constant and T is temperature in K.

The population difference of each spin state is small, but nonetheless exists (e.g. N_α/N_β = 1.000064 for ^1H at B_0 = 9.4 T and T = 298 K). Therefore,

the net magnetisation of all spins is aligned with the field and is termed the bulk magnetisation M_0 (Figure 2.2). Note that each individual spin is precessing around the z-axis at the Larmor frequency.

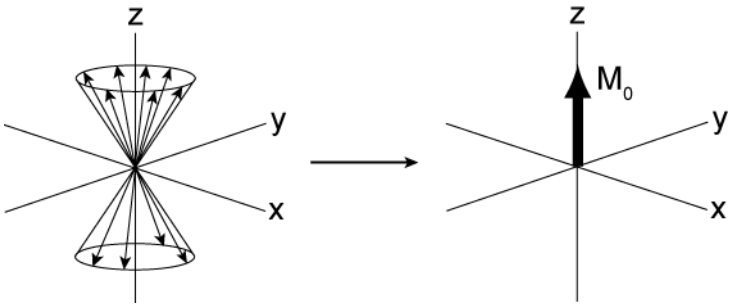

Figure 2.2. Vector model of a collection of spin-½ nuclei aligned with and against the field (left), which leads to bulk magnetisation (M_0). The circle at the end of each arrow vector denotes the precessing path of each spin.

As the population difference is very small, the intensity of NMR signals are inherently weak. The combination of equations (2.1) and (2.2) shows the population difference is proportional to the magnetic field, hence larger magnetic fields are essential to maximise NMR signal.

To acquire an NMR signal, one must flip the bulk magnetisation into the xy-plane. A small radio frequency (rf) pulse is applied along the xy-plane, and the magnetisation precesses about that field (i.e.; if the applied pulse is along the y-axis, the magnetisation precesses around the xz-axis), moving the magnetisation away from the z-axis. After the rf pulse, the bulk magnetisation then precesses around the z-axis at the Larmor frequency, and the NMR signal is recorded. This signal decays due to dephasing of the magnetisation arisen from spin-spin relaxation (magnetisation transfer between spins) and is termed as the free induction decay (FID). The FIDs are recorded and then Fourier

transformed into commonly known NMR spectra.

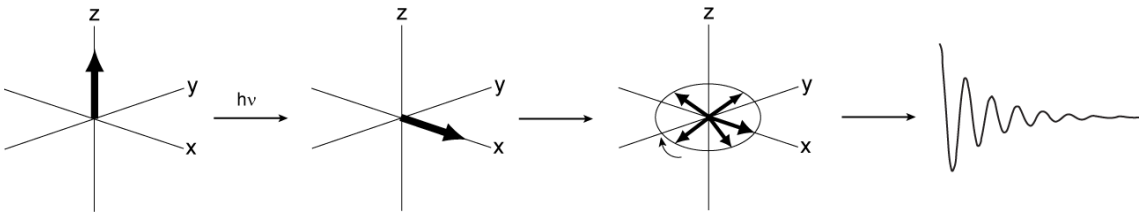

Figure 2.3. Vector model of the bulk magnetisation flipped about the xz-plane with a 90º rf pulse along the y-axis. After the rf pulse, the magnetisation precesses about the z-axis at the Larmor frequency. The magnetisation dephases over time due to spin-spin relaxation, generating an signal that decays over time, termed the FID.

Nuclei in different environments resonate at different frequencies, which arise from the difference in local magnetic fields B_{local}, defined as:

$$B_{local} = B_0 + B_{induced} \qquad (2.3)$$

where

$$B_{induced} = -\sigma B_0 \qquad (2.4)$$

where σ is the chemical shielding arising from the orbiting electrons. Combining equations (2.3) and (2.4) gives:

$$B_{local} = B_0(1 - \sigma) \qquad (2.5)$$

We see from equation (2.1) that $\nu = \gamma B_0/2\pi$, so the resonance condition of each nuclei is expressed as:

$$\upsilon = \frac{\gamma B_0}{2\pi}(1 - \sigma) \qquad (2.6)$$

These resonant frequencies are quoted with respect to an agreed reference compound, e.g. trimethylsilane for ^{1}H and ^{13}C NMR. As the differences in frequency are small and is dependent on the external magnetic

field (equation (2.1)), it is standard practice to convert these values into frequency independent units i.e. parts per million (ppm), normalised to the resonating frequency of the reference compound ν_{ref}, defined as the chemical shift δ. Overall, the chemical shift of a peak is calculated using the following expression:

$$\delta = 10^6 \left(\frac{\nu - \nu_{ref}}{\nu_{ref}} \right) \qquad (2.7)$$

2.1.2 Interactions in NMR

The shift and line shape of NMR signals result from the following interactions:

$$H_{NMR} = H_Z + H_J + H_{CS,iso} + H_{CS,aniso} + H_D + (H_Q) \qquad (2.8)$$

where each, from left to right, are the Hamiltonians for the Zeeman splitting (explained above), J-coupling, isotropic chemical shift, anisotripic chemical shift (arising from chemical shielding), dipolar interaction and quadrupolar interactions (only for quadrupolar nuclei, spin > ½) with their magnitude represented in Table 2.1.

Table 2.1. Relative magnitudes of NMR interactions.

Hamiltonian	Interaction	Magnitude
H_Z	Zeeman	MHz
H_J	J-coupling	Hz
H_D	Dipolar interactions	kHz
$H_{CS,iso}$	Isotropic chemical shift	kHz
$H_{CS,aniso}$	Anisotropic chemical shift	kHz
H_Q	Quadrupolar interactions	MHz

Each Hamiltonian consists of two parts – a spin part that relates to spin-magnetic field interactions, and a geometric part which relates to spatial interactions between spins. The strength of the geometric part consists of an orientation dependent function of form of $3\cos^2\theta-1$ where θ is the angle of the interaction with respect to the external magnetic field B_0.

In solution-state NMR, only H_Z, $H_{CS,iso}$ and H_J are observed in the spectra as the other interactions are orientation dependant and is averaged to 0 by molecular tumbling, resulting in a high resolution spectrum with a sharp isotropic chemical shift peak δ_{iso}. In solid-state NMR, molecules do not exhibit molecular tumbling and therefore the resulting NMR spectra are broader due to these interactions, explained below.

H_{CS} is the sum of the isotropic chemical shift $H_{CS,iso}$ and anisotropic chemical shift $H_{CS,aniso}$ and arises from the interaction between the nuclear spin with the external magnetic field B_0 via electrons. In solids, where no molecular tumbling happens, shifts for all molecular orientations are observed with respect to the magnetic field and is termed the chemical shift anisotropy (CSA) (Figure 2.4). CSA consists of the principal shifts δ_{xx}, δ_{yy} and δ_{zz} and a broad spectrum arises from the sum of the principal shifts and the shifts of the molecule in all other orientations in between. The isotropic chemical shift $\delta_{iso,CS}$ is the mean value of the principle shifts.

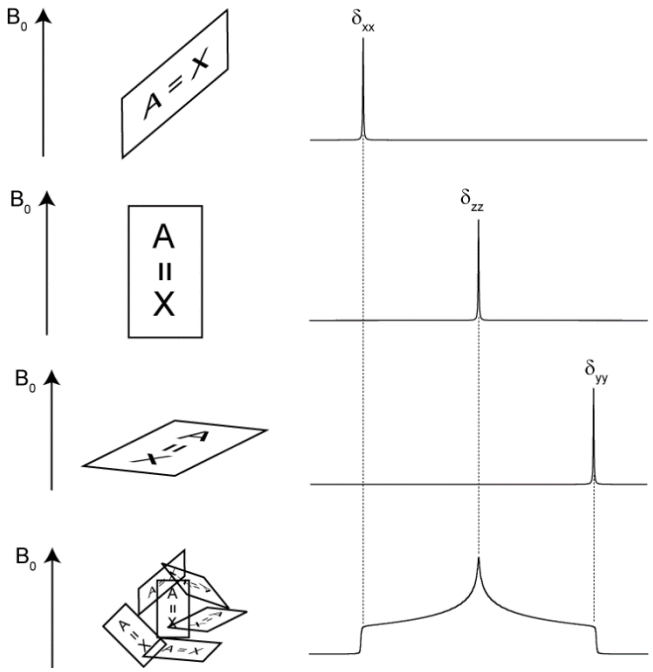

Figure 2.4. Schematic representation of principle values of chemical shift anisotropy δ_{xx}, δ_{yy} and δ_{zz} on a A=X group and the resulting powder NMR pattern arising from the sum of all shifts from all orientations. The peak position is dependent on the orientation of the group with respect to the magnetic field.

Dipolar interactions H_D arise from the interaction between two nearby different nuclear spins. The degree of interaction is defined as follows:

$$|d_{ij}| = \frac{\mu_0}{4\pi}\frac{\hbar\gamma_i\gamma_j}{r_{ij}^3} \qquad (2.9)$$

where $|d_{ij}|$ is the dipolar coupling of constant between nuclei i and j (rad s^{-1}), μ_0 is the vacuum permeability (H m^{-1}), ħ is the reduced Planck constant (J s), γ_i and γ_j is the Larmor frequency of nuclei i and j, and r is the distance between nuclei i and j (m).

Quadrupolar interactions H_Q are present in nuclei with spin > ½. The electric charge distribution in quadrupolar nuclei are not spherically symmetric, and is quantified as the quadrupolar moment Q. This quadrupolar moment

interacts with surrounding electric field gradients and further broaden the resulting spectrum. These interactions are large in the MHz range (but still smaller than the Zeeman interaction) and could make extracting local structural information difficult.

The energy level of the spin states split by Zeeman interaction in quadrupolar nuclei are affected by the first order quadrupolar interactions. This results in the energy difference ΔE between spin states to differ and therefore resonate at different frequencies. The difference between each spin state is proportional to the first order quadrupolar coupling constant $\omega_Q^{[1]}$.[3]

$$\omega_Q{}^{[1]} = \frac{3e^2 Q V_{ZZ}}{2I(I-1)\hbar} \qquad (2.10)$$

where e is the electron charge, Q is the quadrupole moment of the nuclei, and V_{ZZ} is the largest principal component of the electric field gradient.

For nuclei with large ω_Q, a second quadrupolar term, denoted the second order quadrupolar coupling $\omega_Q^{[2]}$, exists and is given by the following expression:[3]

$$\omega_Q{}^{[2]} = \frac{\omega_Q{}^{[1]^2}}{2\omega_0} \qquad (2.11)$$

where ω_0 is the Larmor frequency. The second order quadrupolar coupling significantly affects the acquired NMR spectrum, including the central transition (Figure 2.5).[4] This makes all transition levels anisotropic, resulting in a broad and anisotropic NMR spectrum where the peak maximum is displaced from its isotropic shift. These quadrupolar interactions can be characterised by two parameters C_Q and η_Q, which are the quadrupolar coupling constant and quadrupolar asymmetry parameter respectively, and are defined as follows:

$$C_Q = \frac{eQV_{ZZ}}{h} \qquad (2.12)$$

$$\eta_Q = \frac{V_{YY} - V_{XX}}{V_{ZZ}} \qquad (2.13)$$

where V_{XX}, V_{YY}, and V_{ZZ} are the three principle components of the EFG tensor.

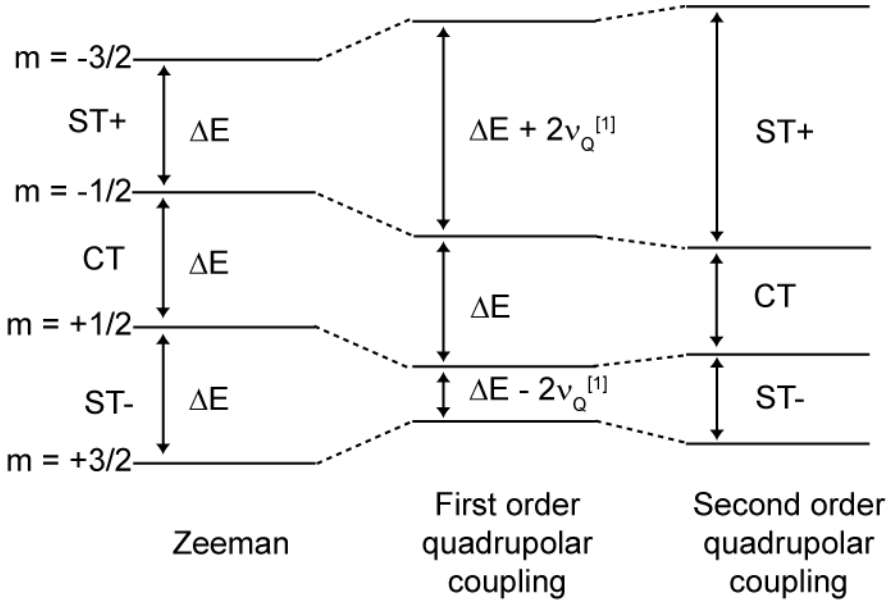

Figure 2.5. Schematic representation of the effect of quadrupolar couplings to the Zeeman split spin states in a spin 3/2 nuclei.[3,4] CT and ST are the central transition and satellite transitions with +/- denoting the resonances appearing at higher and lower frequency, respectively.

2.1.3 Magic Angle Spinning (MAS)

For one to obtain a high resolution NMR spectrum in solid-state NMR, one must apply techniques to average out these interactions. One technique to alleviate the lack of resolution is to obtain spectra while spinning the sample in an NMR rotor at the magic angle (Figure 2.6). Magic angle spinning (MAS) manipulates the orientation dependent part of the geometric component in $H_{CS,aniso}$, H_D (and 1st order H_Q, see below) of form $3\cdot\cos^2\theta - 1$, where θ is the

angle where the sample is spun with respect to B_0. Choosing the root of this term will eliminate this term - one of the root is θ 54.74º – this is defined as the magic angle. Spinning the sample at magic angle averages out both the geometric component of $H_{CS,aniso}$ and H_D to 0 and a high resolution spectrum can be obtained.

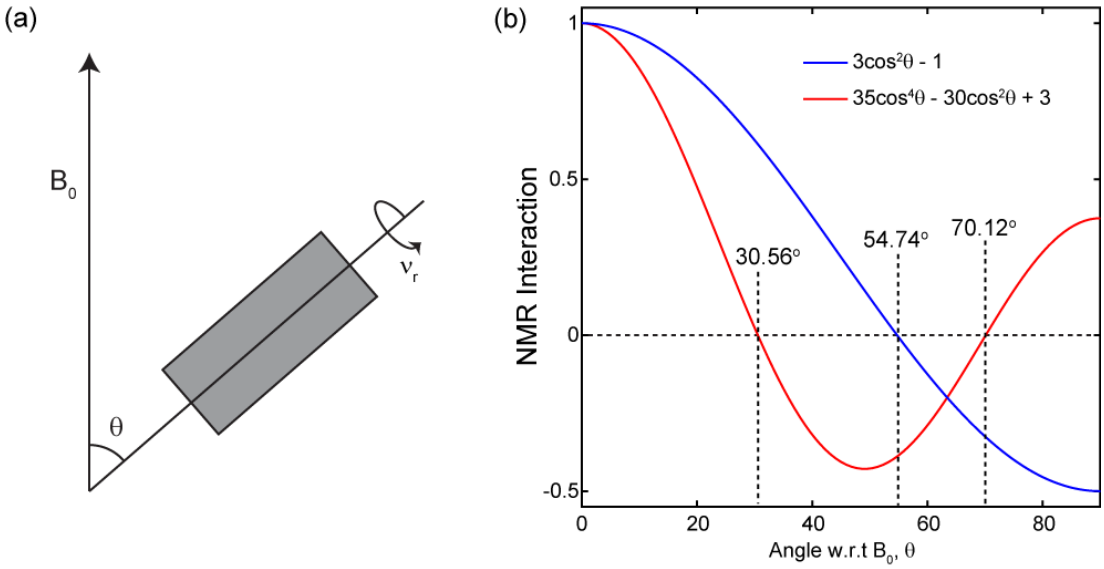

Figure 2.6. (a) Schematic representation of an NMR rotor spinning inside a magnetic field at a spinning rate of ν_r at angle θ with respect to the magnetic field B_0. (b) Angular dependency of NMR interactions. Blue and red lines represents the geometric component of $H_{CS,aniso}/H_D/H_Q$ (first order) and H_Q (second order), respectively.

The rotational rate ν_r at which the sample spins at the magic angle affects the resulting spectrum. If the $H_{CS,aniso}$ and H_D interactions are larger than the rotational rate, peaks appear with a distance equal to integer multiples of the rotational rate, defined as spinning sidebands.[3] If one spins the sample at different rates, the spinning sidebands will change position, however the isotropic peak will not. This allows one to identify the isotropic shift of the nuclei.

For quadrupolar nuclei (nuclei with spin > ½), one must also consider the geometric component in H_Q. The first order quadrupolar coupling $\omega_Q^{[1]}$ can be averaged out similarly to dipolar interactions by spinning at the magic angle as its geometric component is solely $3\cdot\cos^2\theta-1$, however spinning sidebands are likely to show as the magnitude of the interactions is large compared to $H_{CS,aniso}$ and H_D (Table 2.1). The second order quadrupolar coupling $\omega_Q^{[2]}$ consists of two geometric terms of form $3\cdot\cos^2\theta-1$ and $35\cdot\cos^4\theta-30\cdot\cos^2\theta+3$, which do not have the same roots. Therefore, if one spins at the magic angle, the second term averages towards ~0.4, resulting in MAS NMR spectra with residual second order quadrupolar broadening.[3,4]

For quadrupolar nuclei, the MAS NMR spectra are often observed with a "quadrupolar tail" towards higher frequency highlighting the distribution of the residual quadrupolar interactions with the EFG. This can be described using the Czjzek model.[5–7] At the thermodynamic limit (i.e. an infinite number of sites), all interactions are identically distributed according to a Gaussian distribution, termed the Gaussian Isotropic Model. The Czjzek model can then be summarised as the as a probability density function:

$$P(V_{ZZ},\eta_Q)=\frac{1}{\sqrt{2\pi}\sigma^d}V_{ZZ}^4\eta_Q\left(1-\frac{{\eta_Q}^2}{9}\right)\exp\left[-\frac{V_{ZZ}^4\left(1+\frac{{\eta_Q}^4}{9}\right)}{2\sigma^2}\right] \qquad (2.14)$$

where the variables σ and d are defined as the standard deviation of the Gaussian distribution of all quadrupolar interactions and the number of independent EFG tensors (i.e.; 5), respectively.[8,9] These essentially define the shape of the NMR peak and are related to the quadrupolar product P_Q as:

$$P_Q^2 = C_Q^2\left(1 + \frac{{\eta_Q}^2}{3}\right) \approx 5\sigma^2 \qquad (2.15)$$

and therefore can be used to estimate the quadrupolar parameters.

In this thesis, MAS NMR spectra of quadrupolar nuclei with quadrupolar tails are fitted using the CzSimple model in dmfit.[10] This model implements a Czjzek distribution of quadrupolar shift and the Gaussian Isotropic Model with an uncoupled distribution of chemical shift (Equation (2.14)) and extracts the average quadrupolar coupling $\langle C_Q \rangle$ over the P probability.

To obtain high resolution NMR spectra of quadrupolar nuclei, many hardware and software methods have been used to isolate resonances in the resulting NMR spectra to derive their respective C_Q and η_Q values. A selected few are explained below.

2.1.4 Multiple Quantum MAS

One method used to obtain high resolution NMR spectra of quadrupolar nuclei is to use the two-dimensional (2D) multiple quantum MAS (MQMAS) pulse sequence proposed by Frydman et al.[11] by correlating the anisotropic-free NMR spectrum in the vertical F1 dimension and anisotropic-containing NMR spectra in the horizontal F2 dimension. The pulse sequence consisted of three pulses – the first pulse excited all multi-quantum spin states. The second pulse converts all excited quantum states to single quantum, improving efficiency of spin state transitions, before finally refocussing the signal using a soft 90^o selective pulse. To improve the sensitivity and resolution of the resulting spectra, a z-filter sequence was added to the pulse sequence.[12,13] Throughout the thesis, the z-filtered triple quantum MAS (3QMAS) experiment is used – pulse sequence shown in Figure 2.7a.

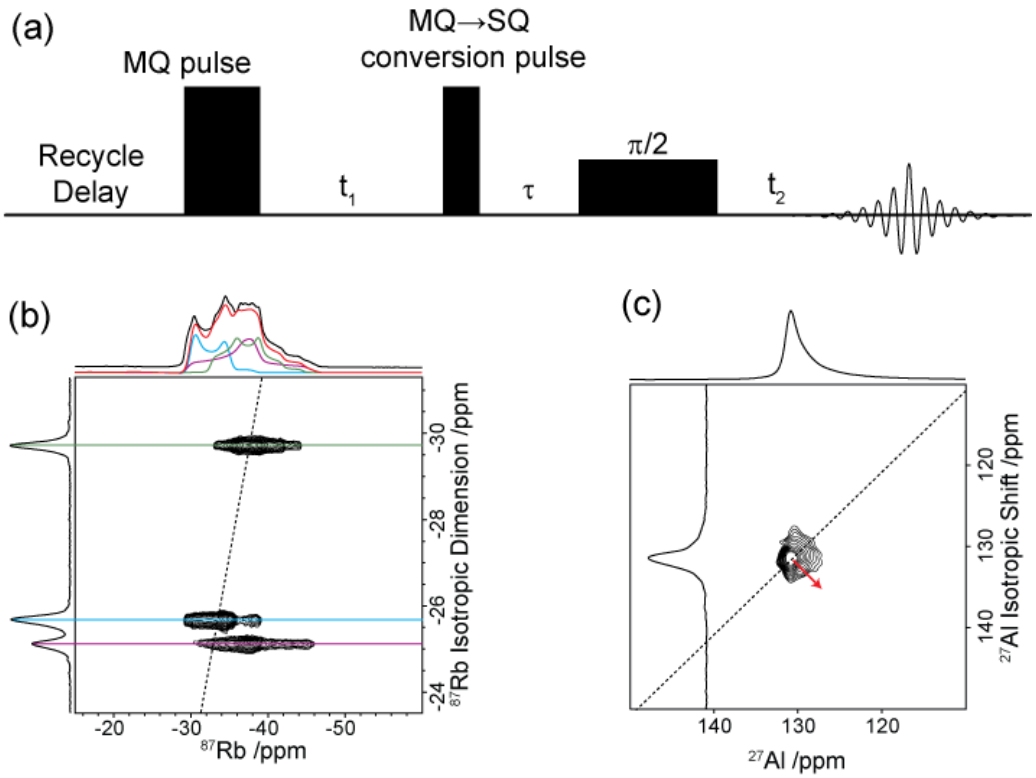

Figure 2.7. (a) Schematic representation of a triple quantum MAS (3QMAS) with z-filtering. t_1 and t_2 are the evolution time in a 2D experiment, set to 1 μs, τ is the z-filter delay, set to 20 μs. (b) A sheared ^{87}Rb 3QMAS NMR spectrum of $RbNO_3$ recorded at 9.4 T at MAS = 10 kHz, showing the three Rb sites. Simulated peaks of each site are green, blue and purple, and the overall fit in red. (c) A sheared ^{27}Al 3QMAS NMR spectrum of $Li_{4.4}Al_{0.4}Sn_{0.6}S_4$ (see Chapter 6 for details). The black dotted line represents the +1 diagonal where different environments are distributed, and the red arrow represents the -1 diagonal where quadrupolar interactions are distributed.

The resulting 2D NMR spectrum is sheared to align the anisotropic axis along the F2 axis (Figure 2.7b and c). The isotropic chemical shift $\delta_{iso,cs}$ of each peak in a z-filtered 3QMAS pulse sequence can then be determined from the centre of gravity of the sheared 2D spectrum using the following expression:[14]

$$\delta_{iso,CS} = \frac{10}{27}\delta_{F2,obs} + \frac{17}{27}\delta_{F1,obs} \quad (2.16)$$

where $\delta_{F2,obs}$ and $\delta_{F1,obs}$ are the observed shifts of the centre of gravity in the F2 and F1 dimensions respectively. Using this expression, the isotropic chemical shift δ_{iso} of the three ^{87}Rb sites are calculated and can be fit to the 1D NMR spectra.

Once the $\delta_{iso,CS}$ of each site is calculated, horizontal slices of each site are extracted and fitted to determine their quadrupolar coupling constant C_Q and the quadrupolar asymmetry parameter η_Q. Furthermore, the distribution of the 2D spectrum gives information on the local environments of the sites. If the distribution occurs diagonally in the +1 direction (Figure 2.7b and c, black dotted line), this is indicative of chemical shift distribution; i.e.; all sites have overlapping isotropic shift. If the distribution occurs in diagonally in the -1 direction, this arises from the distribution of non-averaged quadrupolar interactions in the material arising from structural disorder (Figure 2.7c, red arrow).[15,16] The larger the distribution, the larger the disorder in the material.

2.1.5 Calculation of Isotropic Shift in Quadrupolar Nuclei

The isotropic shift δ_{iso} of quadrupolar nuclei is obtained by summing the field independent isotropic chemical shift $\delta_{iso,CS}$ (Equation 2.16) and the field dependant isotropic quadrupolar shift $\delta_{iso,q}$ as:

$$\delta_{iso} = \delta_{iso,cs} - \delta_{iso,q} \quad (2.17)$$

The isotropic quadrupolar shift $\delta_{iso,q}$ can be obtained by:[14]

$$\delta_{iso,q} = \frac{3C_Q^2\left(I(I+1) - \frac{3}{4}\right)\left(1 + \frac{\eta_Q^2}{3}\right)}{40\nu_0^2 I^2(2I-1)^2} \qquad (2.18)$$

where C_Q is the quadrupolar coupling constant and η_Q is the quadrupolar asymmetry parameter.

2.1.6 Hardware Based Solutions

The second order quadrupolar broadening ω_Q[2] is inversely proportional to the square of the external magnetic field strength B_0, as seen in Equations 2.11 and 2.18.[14,17] Therefore a frequently used technique to increase resolution in NMR on quadrupolar nuclei is to acquire NMR spectra at increasing magnetic field strengths. In this thesis, NMR spectrometers at magnetic field B_0 = 9.4 T (Liverpool, UK), 18.8 T (Lyon, France) and 20 T (Warwick, UK) are used when identifying local environments.

Another hardware based method was proposed is the double rotation (DOR) method by Samoson *et al*.[18] This method uses a double rotor set up and spins at both the magic angle of 54.74° and the angle where the second order quadrupolar coupling averages to zero (30.56°) (Figure 2.6). This method is widely used in materials with overlapping sites where it is difficult to differentiate individual shifts and quadrupolar parameters. This method is not used in this thesis as a DOR probe was not available at the University of Liverpool.

2.1.7 Correlation NMR

To obtain a deeper understanding of the crystal structures, correlation NMR experiments are performed to obtain information surrounding the probe

nuclei. Here, two correlation experiments are described.

2.1.7.1 **Exchange Spectroscopy (EXSY)**

Exchange spectroscopy (EXSY) experiment is a homonuclear 2D NMR experiment which correlates two nearby sites of the same nuclei by the presence of cross peaks in the 2D NMR spectra. After the initial 90^{o} rf pulse, the magnetisation is left to precess around on the xy-plane for time t_1. A second rf pulse is applied along the opposite axis of the initial pulse, which brings the magnetisation back along the z-axis for mixing time τ_m, where sites may interact. Finally, a third rf pulse is applied and NMR signal is acquired. If there is interaction between the sites, a cross peak is observed (Figure 2.8b), as these nuclei resonate at different frequencies during t_1 and t_2.[19] A cross peak signifies the close proximity of the two sites.

Two possible interactions give cross peaks – spin diffusion and chemical exchange. Spin diffusion arises from the magnetisation transfer of the nuclei through dipole-dipole interactions, while chemical exchange originates from physical motion of the nuclei. The two processes can be differentiated by performing EXSY experiments at different MAS rates, as higher MAS averages dipole-dipole interactions reducing intensities of the cross peaks, while cross peaks originating from chemical exchange are unaffected.

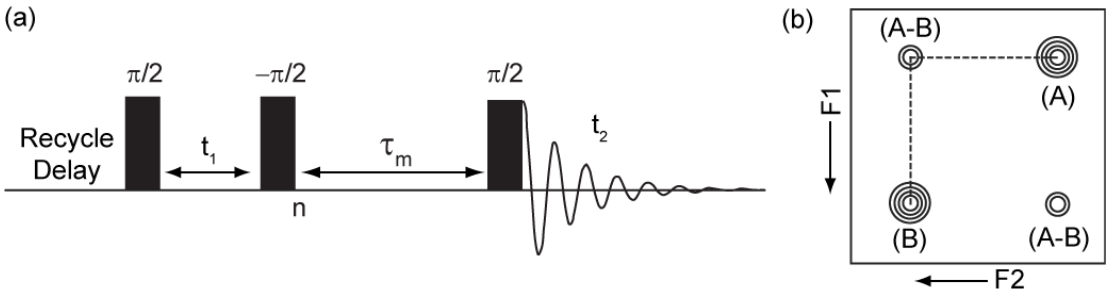

Figure 2.8. (a) Schematic representation the pulse program of a 2D exchange spectroscopy (EXSY) NMR experiment. (b) A 2D EXSY NMR spectrum. (A-B) represents the cross peaks between nuclei A and B.

2.1.7.2 **Heteronuclear Multiple Quantum Correlation (HMQC) NMR**

HMQC is an NMR technique used to correlate the chemical shifts between two different nuclei in close proximity in the sample which allow insight into a large variety of materials, including non-crystalline inorganic structures and porous materials such as zeolites. Correlations could be induced using either J-coupling interactions or dipolar interactions to investigate direct bonding or spatial proximity of the atoms, respectively. In solid state NMR, the J-coupling interaction could be used to investigate bonding, however this interaction is usually very small (Table 2.1) and requires long evolution times to develop, limiting its application.[20] The majority of inorganic Li^+ ion conductors consist of ionic bonds throughout the structures, which does not exhibit J-coupling interactions; therefore HMQC spectra must be obtained using dipolar interactions. Unlike J-coupling interactions, dipolar interactions are averaged out using magic angle spinning, and therefore it must be reintroduced during the NMR experiment.

The HMQC pulse sequence used in this thesis is shown in Figure 2.9. The directly observed nucleus (Nucleus 1) is excited and undergoes a Hahn

echo pulse sequence. During evolution of the magnetisation, a π/2 pulse is performed on the indirectly observed nucleus (Nucleus 2) to convert the signal into multiple quantum coherence signal for period t_1. During this period, a π pulse on Nucleus 1 is flipped. After t_1, a second π/2 pulse is applied to Nucleus 2, refocussing the signal and the coupling between the two nuclei are allowed to rephase, resulting in an NMR spectrum containing dipolar coupling between the two spins. In this thesis, we perform this experiment between two quadrupolar nuclei with spin I > ½, therefore all pulses are selectively excite the central transition to approximate I = ½ spins, widely used in literature in experiments containing quadrupolar nuclei.[20–22]

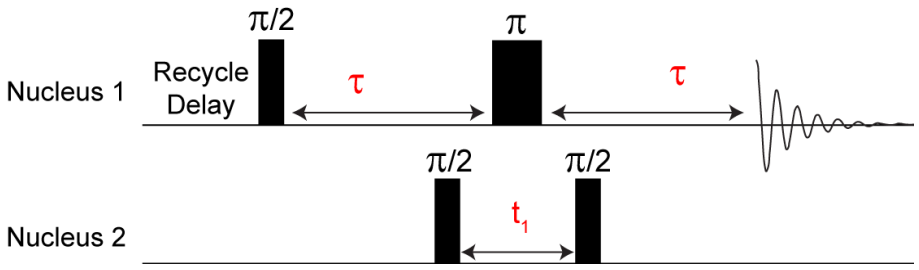

Figure 2.9. Schematic representation of a dipolar-based HMQC pulse sequence.

2.2 Solid-State Lithium NMR

Lithium has two NMR active nuclei – ^{6}Li and ^{7}Li, their properties are stated in Table 2.2. ^{7}Li is often used to probe Li^+ dynamics in solid-state materials due to two reasons: its high natural abundance, and the changes in NMR peak width which are broadened significantly by ^{7}Li–^{7}Li homonuclear dipolar interactions arising from its high gyromagnetic ratio (Equation (2.9)), and by quadrupolar interactions arising from its high quadrupolar moment.[23] These interactions average out with increase in Li^+ mobility and are sensitive

on the NMR time scale of kHz to MHz. However, these large interactions make ^{7}Li an unfavourable choice to obtain local structure information.

^{6}Li, on the other hand, is used largely in local structure investigations. Its smaller gyromagnetic ratio, and a significantly lower quadrupolar moment results in narrower NMR peaks and therefore a high resolution spectrum is acquired. In addition to this, the relationship between ^{6}Li shifts and Li–O coordination number is well knwon,[24–26] and permits the characterisation of local Li environments.

Table 2.2. NMR related properties of ^{6}Li and ^{7}Li. Quadrupolar moments are taken from Stone.[23]

	^{6}Li	**^{7}Li**	**Effect on Spectrum**
Nuclear spin, I	1	3/2	--
Natural abundance	7.59%	92.41%	Sensitivity
Gyromagnetic ratio, γ (10^{6} rad s^{-1} T^{-1})	39.37	103.97	Sensitivity, Li-Li interactions, dipolar broadening
Quadrupolar moment, Q (10^{-30} m^{2})	-0.8	-40.6	Quadrupolar broadening

2.3 Probing Li^{+} Dynamics with Solid-State NMR

In Li^{+} ion conductors, Li^{+} migrates through the material, which is termed solid-state diffusion. NMR can measure the Li^{+} dynamics in these materials on a variety of time scales, ranging from the MHz to sub-Hz using a multitude of techniques, giving information of the Li^{+} diffusion pathway, including

dimensionality, its correlation time, and an activation barrier for ion migration between sites.[27,28] Other techniques that measure Li^+ dynamics, such as impedance spectroscopy, measures long range transport of the Li^+ ions which include defect formation, giving rise to a high activation barrier. Both techniques give complementary information, therefore both must be used to understand Li^+ mobility properties and how the Li^+ ion diffuses between sites, and consequently through the structure. In this thesis, only the solid state NMR studies are reported.

Measuring Li^+ dynamics of solid ion conductors using solid state NMR using various NMR methods have been well documented over the years in a variety of materials from different crystallographic families by probing the temperature dependence of Li^+ jump rate τ^{-1} (information on the main crystallographic families are discussed in Chapter 3).[27,29–36] Here, the main experimental and analytical methods used in this thesis are discussed.

2.3.1 Spin-Lattice Relaxation

Spin-lattice relaxation (SLR) rates (T_1^{-1}) is the rate at which the longitudinal magnetisation of a nuclear spin system returns to thermal equilibrium, called the “lattice”. These are affected by the fluctuation of local magnetic fields caused by the motion of an atom or functional group in the material. The fluctuating fields are described by the correlation function G(t), containing information on the atomic diffusion process and the correlation time τ_c, which is in the same order of magnitude to the mean residual time τ of the spin between jumps.[28,37,38] The correlation function G(t) decays exponentially with the following equation assumed by the Bloembergen-Purcell-Pound

(BPP) theory:

$$G(t) = G(0)\exp\left(-\frac{|t|}{\tau_c}\right) \quad (2.19)$$

The Fourier transform of Equation 2.14 gives the spectral density function $J(\omega_0)$:

$$J(\omega_0) = G(0)\left(-\frac{2\tau_c}{1+\omega_0{}^2\tau_c{}^2}\right) \quad (2.20)$$

The correlation time τ_c, and by extension the mean residual time τ, are temperature dependent according to the Arrhenius relation:

$$\tau_c = \tau_{c,0}\exp\left(\frac{E_a}{k_B T}\right) \quad (2.21)$$

These can hence be used to investigate Li^+ diffusion on the Larmor frequency (ω_0) time scale of MHz by monitoring the change in T_1^{-1}.

T_1^{-1} values are obtained using the saturation recovery pulse sequence shown in Figure 2.10a. The magnetisation is saturated along the xy-plane with multiple pulses with a small delay with respect to the T_1 (for example, n = 50, delay ≈ 1 ms). After the final pulse the saturated magnetisation are allowed to relax for variable time τ, then are pulses by a 90° pulse and an FID signal is recorded.

The recorded signals are normalised and are then fit to an exponential function of form $1–\exp[–(\tau/T_1)]$. In most cases, however, the signals are the distribution of relaxation processes of multiple sites, arising from the fluctuation of the electric field gradient found in quadrupolar nuclei[39] such as ^7Li (I = 3/2), correlative motion of ^7Li during diffusion and multiple Li^+ sites present in the structure, and hence do not have good fits. Therefore, a stretched exponential function of form $1–\exp[–(\tau/T_1)^\alpha]$ is used, where α is the stretch exponent

(Figure 2.10b).

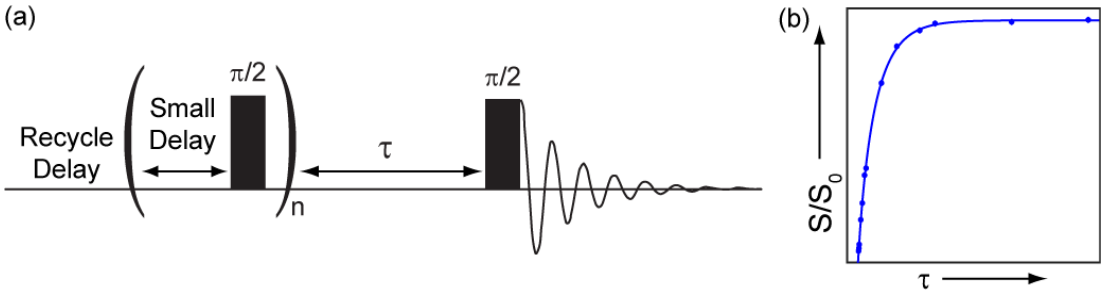

Figure 2.10. (a) Schematic representation of a saturation recovery pulse sequence. (b) Schematic representation of normalised signal intensity S_0/S vs. polarisation time τ plot for data obtained by saturation recovery. The blue line is a fit to the data using the following expression $1–\exp[–(\tau /T_1)^{\alpha}]$. See text for further explanation.

2.3.2 Spin-Lattice Relaxation in the Rotating Frame

As the SLR rates T_1^{-1} are measured on the time scale of MHz, the dynamics of slower processes are not observed, and a more sensitive technique is required to measure on a slower time scale. Spin-lock pulses are used to measure the SLR rate in the rotating frame ($T_{1\rho}^{-1}$), shown in Figure 2.11a, and give information on the dynamics on the spin-lock frequency time scale (ω_1) of kHz. The bulk magnetisation converted into the transverse plane are locked into a single axis with a long pulse of the pulse frequency ω_1 for time τ. During this long pulse, the spins relax on the order of ω_1, then precess freely to form an FID after time τ. The signals are normalised and fit to a stretch exponential of form $\exp[–(\tau/T_{1\rho})^{\alpha}]$.

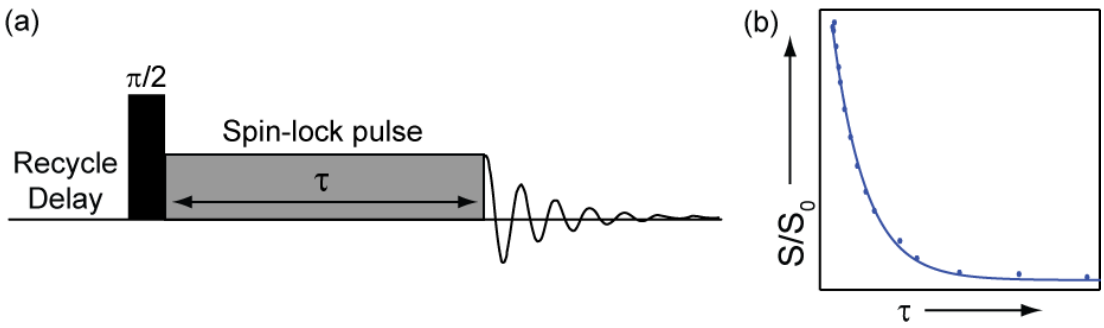

Figure 2.11. (a) Schematic representation of a spin-lock pulse sequence. (b) Schematic representation of normalised signal intensity S/S_0 vs. spin-lock time τ plot for data obtained by the spin-lock pulse sequence. The blue line is a fit to the data using the expression $\exp[-(\tau/T_{1\rho})^{\alpha}]$.

2.3.3 Motional Narrowing

NMR spectra are dominated by the dipolar and quadrupolar interactions arising from the overlap of multiple resonating nuclear spins experiencing different local magnetic fields B_{local} superimposing B_0. As the spin jumps into its neighbouring site, the local magnetic field sensed by the nuclei fluctuates between $\pm B_{local}$ on the time-scale of the mean residual time τ between jumps.[38] If τ is very small ($\tau << T_2$, where T_2 is the spin-spin relaxation time), the spin will jump between many different B_{local} and the net B_{local} of the spin is small. This increases the dephasing between spins, increasing the FID length, resulting in a narrowing of NMR line width. This is termed motional narrowing (Figure 2.12).

At low temperature, the NMR line width is at its maximum as all spins have no mobility. As the system is heated, the mobility of the spin – in our case ^7Li – increases and averages out the dipolar and quadrupolar interactions, resulting in the narrowing of NMR line width. The Li^+ jump rate τ^{-1} is estimated

from the NMR line width at the inflection point of this curve using the relationship $\tau^{-1} = 2\pi \cdot \Delta\nu$, where $\Delta\nu$ is the full width of the NMR peak at half maximum in Hz.[31,40]

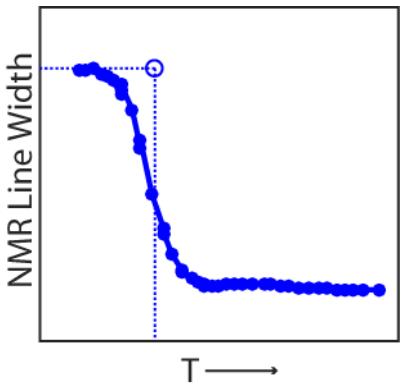

Figure 2.12. Schematic representation of motional narrowing of NMR line width with increase in temperature. Solid line follows the change of NMR line width with change in temperature. Vertical and horizontal dotted line shows the inflection point of the curve and the associated jump rate τ^{-1} of the probed nuclei, respectively.

2.3.4 Extracting Dynamics Information

To extract information regarding Li^+ dynamics, one must first determine the dominant relaxation interaction to know which model of relaxation can be applied for analysis. For Li^+ ion conductors, this can be determined by extracting ratio between ^6Li and ^7Li T_1^{-1} rates.[41] In cases where quadrupolar relaxation is the dominant relaxation mechanism:

$$\frac{T_1(^7Li)}{T_1(^6Li)} \propto \frac{C_Q(^7Li)}{C_Q(^6Li)} \propto \frac{Q^2(^7Li)}{Q^2(^6Li)} \approx 4 \times 10^{-4} \qquad (2.22)$$

The ratio when the dominant relaxation mechanism is dipolar is:

$$\frac{T_1(^7Li)}{T_1(^6Li)} \propto \frac{\gamma^4(^7Li)}{\gamma^2(^6Li)\gamma^2(^7Li)} \frac{1}{I(^7Li)\left[I(^6Li)+I(^7Li)\right]} \approx 0.5 \qquad (2.23)$$

assuming that ^{7}Li and ^{6}Li only interact with ^{7}Li.

For quadrupolar relaxation, the Li^+ correlation time τ_c, and by extension the residual time $\bar{\tau}$ of the spins between jumps, can be extracted directly using the following formula:[42]

$$T_1 = \frac{3}{40}\frac{2I+3}{I^2(2I-1)} C_Q^2 \left(1+\frac{\eta_Q^2}{3}\right)\tau_c \qquad (2.24)$$

For systems where dipolar relaxation is the dominant mechanism, the Bloembergen-Purcell-Pound (BPP) model[37] is applied to extract Li^+ jump rates τ^{-1}. The BPP theory denotes that correlation times τ_c are proportional to the spectral density function $J(\omega)$ of the NMR spectra (Equation (2.20)). When the SLR rates obtained by saturation recovery and spin-lock are plotted against reciprocal temperature using the Arrhenius function, a volcano plot is made (Figure 2.13). The maximum point of this volcano plot denotes where the spectral density $J(\omega)$ is at its maximum, therefore the jump rate τ^{-1} are on the order of the probe frequency and could be extracted: $\omega_0\tau_c \approx 0.62$ for T_1^{-1} values and $2\omega_1\tau_c \approx 0.5$ for $T_{1\rho}^{-1}$ values.[28,43] The τ_c^{-1} values obtained is then expected to follow the Arrhenius behaviour according to the equation:

$$\tau_c^{-1} = \tau_{c,0}^{-1} \exp\left(-\frac{E_a}{k_B T}\right) \qquad (2.25)$$

where $\tau_{c,0}^{-1}$ is the pre-exponential factor (i.e. the number of hops per unit time of a particle), E_a is the activation barrier of the diffusion process and k_B is the Boltzmann constant. The inverse correlation time τ_c^{-1} is on the same order of magnitude as jump rate τ^{-1} and are used conjunctly.

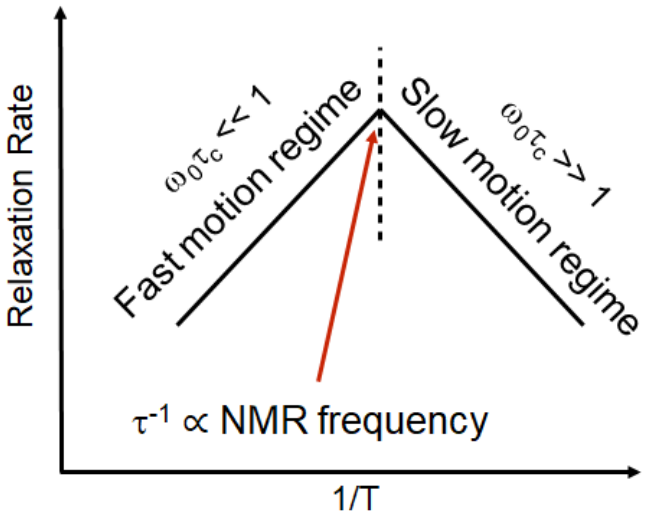

Figure 2.13. Schematic representation of the temperature dependence of NMR SLR rates.

The high temperature side of the volcano plot is the fast motion regime where $\omega_{0(1)}\tau_c << 1$. The relationship between the $T_{1(\rho)}^{-1}$ values on the high temperature flank measured at different frequencies give information on the dimensionality of the Li^+ diffusion process (summarised in Table 2.3), as the spins undergo several jumps before a single precession of the probe frequency.[28,44] The activation barrier is free from correlative effects and corresponds to full translational diffusion of the mobile ion, i.e.; Li^+ motion from one site to its neighbouring site.

One of the factors in the correlation function G(t) (Equation (2.19)) is described as a pair distribution function:

$$P(r_0, r, t) = (8\pi Dt)^{-n/2} \exp\left(-\frac{|r - r_0|^2}{8Dt}\right) \qquad (2.26)$$

where r_0 is the original position of the nuclei, r is the position of the nuclei after time t, D is the diffusion constant and n is the dimension of diffusion (n = 1 for 1D, 2 for 2D, and 3 for 3D).[44] Fourier transforming this, one can deduce that

at higher temperatures, $J(\omega) \propto 1/D$, which is the relationship of three-dimensional spin diffusion in liquids.[43,44] The value of the constant coefficient in the $J(\omega) \propto 1/D$ relationship for solids and liquids are analogous within error of calculation, and therefore this relationship is used for 3D spin diffusion in solids.

D can be derived from jump rate τ^{-1} using the Einstein-Smolchowski equation:

$$D = \frac{fa^2}{2n}\tau^{-1} \qquad (2.27)$$

where f is the correlation factor and a is the average hopping distance of the mobile ion (in cases for Li^+ ion conductors, Li^+). Since for a given solid the correlation factor, hopping distance and diffusion dimension is constant, one can then derive that $J(\omega) \propto \tau$.Therefore, one can deduce that the $T_{1(\rho)}^{-1}$ values for 3D Li^+ ion diffusion are independent of the probe frequency in the fast motion regime.

For 2D diffusion processes, one must consider the effect of ions diffusing in a plane rather than in all directions like 3D diffusion. Avogadro and Villa numerically determined the relationship between the spectral density and frequency as $J(\omega) \propto \ln \omega^{-1}$ and confirmed the relationship by probing HNO_3 diffusion between graphite sheets.[45] Sholl took this relationship and using Equation (2.26), derived the relationship $J(\omega) \propto 1/D \ln(-D/\omega)$. Using Equation (2.27), one can then derive $J(\omega) \propto \tau \ln(1/\omega\tau)$, i.e. $T_{1(\rho)}^{-1}$ values are shown proportional to $\tau \ln(1/\omega\tau)$. This is also known as Richards' semi empirical model, where Richards and Salamon identified this relationship using electron spin resonance.[46,47]

For systems with 1D diffusion processes, the correlation function G(t) and hence the spectral density J(ω) in the fast motion regime was experimentally determined to diverge towards $\omega^{-1/2}$.[48,49] Sholl took this relationship and using Equation (2.27) and can derive $J(\omega) \propto (\tau/\omega)^{1/2}$, and therefore see that $T_{1(\rho)}^{-1}$ values follow the square root of residual time in a single site over the probed frequency.

The low temperature side of this volcano plot, on the other hand, corresponds to the slow motion regime where spins do not fully jump between sites before a single precession of the probe frequency and is therefore not affected by the diffusion dimensionality. In this regime, $\omega_{0(1)}\tau_c >> 1$, which makes $1 + \omega_{0(1)}\tau_c = \omega_{0(1)}\tau_c$, therefore $J(\omega_{0(1)}) \propto 2\tau_c/\omega_{0(1)}^2\tau_c^2 \approx \omega_{0(1)}^{-2}\tau^{-1}$ and so one can derive that the $T_{1(\rho)}^{-1}$ values in this regime are frequency dependant. The activation energy E_a extracted in this regime is related to the energy required for local hop motion between local energy minima within the energy well including of the ion unsuccessful jumps between sites, rather than long range translational Li^+ ion diffusion.[50]

The BPP theory predicts that the volcano plot is symmetric and the quadratic frequency dependence of the spectral density function J(ω), and by extension $T_{1(\rho)}^{-1}$ values, is proportional to ω^{-2}. Many cases, however, are asymmetric and deviate from this model due to dimensionality of the diffusion and disorder in the studied system. The activation barrier for diffusion of Li^+ ions in solid conductors in the slow motion regime are affected by structural disorder in the material, Coulombic interactions and correlation effects of the mobile ions.[28,51] This asymmetry has a frequency dependence of $T_{1(\rho)}^{-1} \propto \omega^{-\beta}$ where β is the model parameter ranging between 1 and 2, which therefore

would give the low temperature limit relationship as $J(\omega) \propto \tau^{-1}\omega^{-\beta}$.

Table 2.3. High and Low Temperature Limits for 1D, 2D and 3D diffusion.[28]

	High Temperature Limits	Low Temperature Limits
1D	$(\tau/\omega)^{0.5}$	$\tau^{-1}\omega^{-\beta}$
2D	$\tau \ln(1/\omega\tau)$	$\tau^{-1}\omega^{-\beta}$
3D	τ	$\tau^{-1}\omega^{-\beta}$

2.3.5 Other Approaches in Literature

In this section, some complementary techniques used frequently in measuring Li^+ dynamics in literature, but not used this thesis due to circumstances detailed below, are explained for completeness.

2.3.5.1 **EXSY**

EXSY experiments, described earlier in this thesis, can also be used to measure Li^+ dynamics in Li^+ ion conductors.[25,26,30,52] In these cases, individual sites must be well resolved, hence ^6Li is preferred over ^7Li. The natural abundance of ^6Li is also low compared to ^7Li (Table 2.2), which gives good spacial separation of each ^6Li spin, and essentially neglects the possibility of spin diffusion. Therefore, any cross peaks that emerge come from chemical exchange of the nuclei.

The intensity of cross peaks relative to the mixing time τ_m are used widely to extract Li^+ exchange rates $\tau_{exchange}^{-1}$ between different sites using the following relationship:[30]

$$\frac{I_{cross}}{I_{main}} = \left[1 - \exp\left(-\frac{\tau_m}{\tau_{exchange}}\right)\right] \quad (2.28)$$

where I_{cross} and I_{main} are the intensities of the cross peak and main peak respectively, τ_m is the mixing time and $\tau_{exchange}$ is the exchange time. The exchange rate $\tau_{exchange}^{-1}$ is synonymous to the jump rate τ^{-1} as they both probe Li^+ mobility between sites.

In this thesis, all the peaks in the ^6Li NMR spectra are not well resolved. This does not enable accurate determination of extracting the intensity of cross peaks, hindering the determination of τ^{-1}. Therefore, in this thesis, EXSY is used primarily to identify correlation between peaks rather than to measure Li^+ dynamics.

2.3.5.2 **Pulse Field Gradient**

Pulse field gradient (PFG) NMR is used to yield macroscopic diffusion parameters of the probed nuclei.[1] Instead of extracting Li^+ jump rates τ^{-1}, the technique directly measures diffusion coefficients in the range of 10^{-14}~10^{-11} m^2 s^{-1}. The technique utilises the spin echo pulse sequence with two superimposing pulsed magnetic field gradient g during the evolution time τ_{evo} of pulse length δ, separated by interval time Δ (Figure 2.14). The initial gradient pulse cause the magnetisation of different sites to precess differently and dephases the signal. After the echo pulse at $\Delta/2$, a second gradient pulse is applied to refocus the magnetisation into an echo NMR spectrum. If the positions of the nuclei changes position during the time Δ, then the refocussing will be incomplete and the intensity of the echo will decrease. The diffusion coefficients can be calculated by using the Stejskal-Tanner equation:[53,54]

$$M_G(2\tau) = M_0(2\tau)\exp(-bD) \quad (2.29)$$

where

$$b = -\gamma^2 g^2 \delta^2 \left(\Delta - \frac{\delta}{3}\right) \quad (2.30)$$

where g, δ and Δ denote the strength, length and the interval time of the gradient field pulses, and D is the diffusion coefficient.

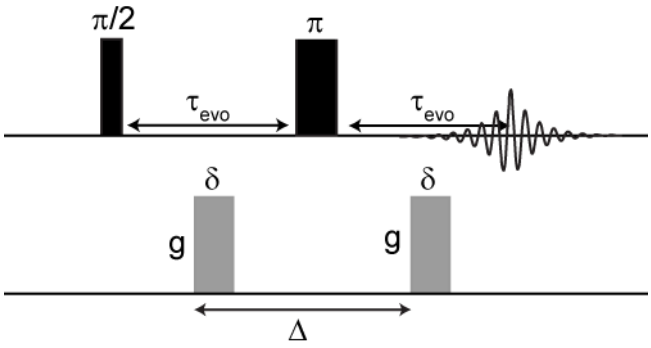

Figure 2.14. Schematic representation of a pulse field gradient NMR pulse sequence.

A gradient probe is required to perform PFG NMR, which are special probes optimised for strong gradient pulses. This equipment was not available at the University of Liverpool, and therefore PFG NMR is not used in this thesis.

2.3.6 Conversion into diffusion coefficient and conductivity

The extracted jump rates τ^{-1} can be converted into other units, for example, diffusion coefficients ($cm^2\ s^{-1}$) or conductivity ($S\ cm^{-1}$), to give further context to their values. Jump rates τ^{-1} are converted into diffusion coefficients with the Einstein-Smolchowski equation (Equation (2.27)). The diffusion coefficient is then converted into conductivity using the Nernst-Einstein equation:

$$D = \frac{k_B T}{N_{CC} q^2} H_R \sigma \qquad (2.31)$$

where N_{CC} is the number of charge carriers per unit cell volume, q is the ionic charge of the charge carrier, H_R is the Haven ratio and σ is the conductivity (S m^{-1}). The conductivity derived in this way using NMR derived jump rates τ^{-1} is often denoted as the NMR conductivity σ_{NMR}. H_R is the ratio between the tracer diffusion coefficient D_{tr}, which describes a single particle motion of the diffusing species, and the charge diffusion coefficient D_σ, derived from the measurements of ionic conductivity.

Combination and rearranging of equations (2.27) and (2.31) gives an overall equation of:

$$\sigma = \frac{f}{H_R} \frac{N_{CC} q^2 a^2}{2 n k_B T} \tau^{-1} \qquad (2.32)$$

The correlation factor f and the Haven ratio H_R are both related to correlative motion of the Li^+ ions into and out of vacant sites.[55,56] The correlation factor f = 1 for uncorrelated motion and tends towards 0 with the presence of correlative diffusion, dependant on the mechanism and its probability of occurrence. The Haven ratio H_R is the ratio between the tracer diffusion coefficient D_{tr} occurring from self diffusion of the charge carrier and the charge diffusion coefficient D_σ obtained from impedance spectroscopy.

In this thesis, we assume uncorrelated Li^+ion motion. In this case, $D_{tr} = D_s$ as there are no correlative effects to alter the values of each coefficient, and therefore $H_R = 1$. Finally, $f/H_R = 1$.

2.3.7 Temperature Calibration

All NMR methods used to measure Li^+ dynamics in this thesis require

experiments to be conducted at various temperatures. A thermocouple cannot be placed inside an NMR rotor to measure the temperature of the sample directly, so one must calibrate the NMR probe *ex situ* using known chemical thermometers. In this thesis, ^{207}Pb NMR of $Pb(NO_3)_2$ is used for both static and MAS conditions as the ^{207}Pb chemical shift of $Pb(NO_3)_2$ is very sensitive to temperature.[57,58] The temperature calibration is verified by following the ^{63}Cu shift of CuBr and CuI with temperature, and their respective γ-to-β phase transitions at 658 K and 642 K.[59,60]

2.4 References

1 M. E. Levitt, *Spin Dynamics: Basics of Nuclear Magnetic Resonance*, Wiley, 2nd edn., 2008.

2 J. Keeler, *Understanding NMR Spectroscopy*, Wiley-Blackwell, 2010.

3 D. D. Laws, H.-M. L. Bitter and A. Jerschow, *Angew. Chemie Int. Ed.*, 2002, **41**, 3096–3129.

4 P. P. Man, in *Encyclopedia of Analytical Chemistry*, John Wiley & Sons, Ltd, Chichester, UK, 2006, pp. 12224–12265.

5 G. Czjzek, J. Fink, F. Götz, H. Schmidt, J. M. D. Coey, J. P. Rebouillat and a. Liénard, *Phys. Rev. B*, 1981, **23**, 2513–2530.

6 J.-B. d'Espinose de Lacaillerie, C. Fretigny and D. Massiot, *J. Magn. Reson.*, 2008, **192**, 244–251.

7 F. Vasconcelos, S. Cristol, J.-F. Paul, L. Delevoye, F. Mauri, T. Charpentier and G. Le Caër, *J. Phys. Condens. Matter*, 2013, **25**, 255402.

8 P. J. Knijn, P. J. M. van Bentum, E. R. H. van Eck, C. Fang, D. L. A. G.

Grimminck, R. A. de Groot, R. W. A. Havenith, M. Marsman, W. L. Meerts, G. A. De Wijs and A. P. M. Kentgens, *Phys. Chem. Chem. Phys.*, 2010, **12**, 11517–11535.

9 D. L. A. G. Grimminck, Radboud University Nijmegen, 2013.

10 D. R. Neuville, L. Cormier and D. Massiot, , DOI:10.1016/j.gca.2004.05.048.

11 A. Medek, J. S. Harwood and L. Frydman, *J. Am. Chem. Soc.*, 1995, **117**, 12779–12787.

12 J.-P. Amoureux, C. Fernandez and S. Steuernagel, *J. Magn. Reson. Ser. A*, 1996, **123**, 116–118.

13 A. Goldbourt and P. K. Madhu, in *Annual Reports on NMR Spectroscopy*, 2004, vol. 54, pp. 81–153.

14 M. Smith, *Prog. Nucl. Magn. Reson. Spectrosc.*, 1999, **34**, 159–201.

15 D. Massiot, F. Fayon, M. Capron, I. King, S. Le Calvé, B. Alonso, J.-O. Durand, B. Bujoli, Z. Gan and G. Hoatson, *Magn. Reson. Chem.*, 2002, **40**, 70–76.

16 P. R. Bodart, *J. Magn. Reson.*, 1998, 133, 207–209.

17 Z. Gan, P. Gor'kov, T. A. Cross, A. Samoson and D. Massiot, *J. Am. Chem. Soc.*, 2002, **124**, 5634–5635.

18 A. Samoson, E. Lippmaa and A. Pines, *Mol. Phys.*, 1988, **65**, 1013–1018.

19 H. C. Gaede, in *Modern NMR Spectroscopy in Education*, eds. D. Rovnyak and R. Stockland, American Chemical Society, Washington, DC, 2007, vol. 969, pp. 176–189.

20 D. Iuga, C. Morais, Z. Gan, D. R. Neuville, L. Cormier and D. Massiot, *J. Am. Chem. Soc.*, 2005, **127**, 11540–11541.

21 D. Massiot, B. Touzo, D. Trumeau, J. P. Coutures, J. Virlet, P. Florian and P. J. Grandinetti, *Solid State Nucl. Magn. Reson.*, 1996, **6**, 73–83.

22 D. Massiot, F. Fayon, B. Alonso, J. Trebosc and J. P. Amoureux, *J. Magn. Reson.*, 2003, **164**, 160–164.

23 N. J. Stone, *At. Data Nucl. Data Tables*, 2005, **90**, 75–176.

24 K. J. D. MacKenzie and M. E. Smith, *Multinuclear Solid-State Nuclear Magnetic Resonance of Inorganic Materials*, Elsevier, Oxford, 2002.

25 Z. Xu and J. F. Stebbins, *Solid State Nucl. Magn. Reson.*, 1995, **5**, 103–112.

26 Z. Xu and J. F. Stebbins, *Science (80-.).*, 1995, **270**, 1332–1334.

27 M. Wilkening and P. Heitjans, *ChemPhysChem*, 2012, **13**, 53–65.

28 P. Heitjans, A. Schirmer and S. Indris, *NMR and β-NMR Studies of Diffusion in Interface-Dominated and Disordered Solids*, Springer-Verlag Berlin Heidelberg, The Netherlands, 2005.

29 O. Bohnke, J. Emery and J. L. Fourquet, *Solid State Ionics*, 2003, **158**, 119–132.

30 P. Bottke, D. Freude and M. Wilkening, *J. Phys. Chem. C*, 2013, **117**, 8114–8119.

31 A. Kuhn, P. Sreeraj, R. Pöttgen, H. D. Wiemhöfer, M. Wilkening and P. Heitjans, *J. Am. Chem. Soc.*, 2011, **133**, 11018–11021.

32 H. Buschmann, J. Dölle, S. Berendts, A. Kuhn, P. Bottke, M. Wilkening, P. Heitjans, A. Senyshyn, H. Ehrenberg, A. Lotnyk, V. Duppel, L. Kienle and J. Janek, *Phys. Chem. Chem. Phys.*, 2011, **13**, 19378.

33 K. Arbi, M. Hoelzel, A. Kuhn, F. García-Alvarado and J. Sanz, *Phys. Chem. Chem. Phys.*, 2014, **16**, 18397–18405.

34 A. Kuhn, V. Duppel and B. V. Lotsch, *Energy Environ. Sci.*, 2013, **6**, 3548.

35 V. Epp, Q. Ma, E.-M. Hammer, F. Tietz and M. Wilkening, *Phys. Chem. Chem. Phys.*, 2015, **17**, 32115–32121.

36 Y.-X. Xiang, G. Zheng, G. Zhong, D. Wang, R. Fu and Y. Yang, *Solid State Ionics*, 2018, **318**, 19–26.

37 N. Bloembergen, E. M. Purcell and R. V Pound, *Phys. Rev.*, 1948, **73**, 679–712.

38 H. Mehrer, *Diffusion in solids: fundamentals, methods, materials, diffusion-controlled processes*, Springer Berlin Heidelberg, Berlin, Heidelberg, 2007, vol. 155.

39 P. S. Hubbard, *J. Chem. Phys.*, 1970, **53**, 985–987.

40 A. B. Santibáñez-Mendieta, C. Didier, K. K. Inglis, A. J. Corkett, M. J. Pitcher, M. Zanella, J. F. Shin, L. M. Daniels, A. Rakhmatullin, M. Li, M. S. Dyer, J. B. Claridge, F. Blanc and M. J. Rosseinsky, *Chem. Mater.*, 2016, **28**, 7833–7851.

41 T. Pietrass, F. Taulelle, P. Lavela, J. Olivier-Fourcade, J.-C. Jumas and S. Steuernagel, *J. Phys. Chem. B*, 1997, **101**, 6715–6723.

42 T. C. Farrar and E. D. Becker, in *Pulse and Fourier Transform NMR*, eds. T. C. FARRAR and E. D. B. T.-P. and F. T. N. M. R. BECKER, Elsevier, San Diego, 1971, pp. 46–65.

43 A. Abragam, *The Principles of Nuclear Magnetism*, Oxford University Press, Oxford, 1961.

44 C. A. Sholl, *J. Phys. C Solid State Phys.*, 1981, **14**, 447–464.

45 A. Avogadro and M. Villa, *J. Chem. Phys.*, 2003, **66**, 2359–2367.

46 P. M. Richards and M. B. Salamon, *Phys. Rev. B*, 1974, **9**, 32–45.

47 P. M. Richards, in *Physics of Superionic Conductors*, ed. M. B. Salamon, Springer Berlin Heidelberg, Berlin, Heidelberg, 1979, pp. 141–174.

48 M. Nechtschein, F. Devreux, R. L. Greene, T. C. Clarke and G. B. Street, *Phys. Rev. Lett.*, 1980, **44**, 356–359.

49 J. P. Boucher, M. A. Bakheit, M. Nechtschein, M. Villa, G. Bonera and F. Borsa, *Phys. Rev. B*, 1976, **13**, 4098–4118.

50 R. Böhmer, K. R. Jeffrey and M. Vogel, *Prog. Nucl. Magn. Reson. Spectrosc.*, 2007, **50**, 87–174.

51 A. Kuhn, S. Narayanan, L. Spencer, G. Goward, V. Thangadurai and M. Wilkening, *Phys. Rev. B - Condens. Matter Mater. Phys.*, 2011, **83**, 1–11.

52 M. Wilkening, W. Küchler and P. Heitjans, *Phys. Rev. Lett.*, 2006, **97**, 065901.

53 E. O. Stejskal and J. E. Tanner, *J. Chem. Phys.*, 1965, **42**, 288–292.

54 J. E. Tanner, *J. Chem. Phys.*, 1970, **52**, 2523–2526.

55 K. Compaan and Y. Haven, *Trans. Faraday Soc.*, 1956, **52**, 786–801.

56 A. Marcolongo and N. Marzari, *Phys. Rev. Mater.*, 2017, **1**, 025402.

57 A. Bielecki and D. P. Burum, *J. Magn. Reson. Ser. A*, 1995, **116**, 215–220.

58 P. A. Beckmann and C. Dybowski, *J. Magn. Reson.*, 2000, **146**, 379–380.

59 K. D. Becker, *J. Chem. Phys.*, 1978, **68**, 3785–3793.

60 J. Wu, N. Kim and J. F. Stebbins, *Solid State Nucl. Magn. Reson.*, 2011, **40**, 45–50.

3. Review of Selected Li^+ Electrolytes

This chapter aims to give a basic literature review to the main families of solid state Li^+ electrolytes related to the materials studied in the consecutive chapters. The main structural differences in each family and their attractiveness for application in Li^+ ion batteries are highlighted in context with their respective solid state NMR studies. For further exhaustive reviews of each material's crystal chemistry and their performance by both NMR and other techniques, reviews by Stramare *et al*.,[1] Knauth,[2] Bachman *et al*.[3] and Xiang *et al*.[4] are noted.

3.1 Perovskites

A perovskite structure has a basic formula of ABX_3 where A and B are different sized cations and X is the anion. The B cation is octahedrally coordinated to six X anions. Each X anion bridges with another B cation, forming a 3D lattice of corner shared BX_6 octahedra. The A site cation resides in a 12-coordination hole made by the octahedral lattice. Perovskites have grown rapid interest in various materials communities, including the battery community, due to their flexible nature in replacing both A- and B-site cations, and their ability to not only dope into the cation sites but also the anion sites.[5] Additionally, the presence of anti-perovskites where the anion and cation sites are reversed, such as Li_3OCl,[6–8] further contribute to the general interest of this family of materials.

The best perovskite Li^+ ion conductor currently known is the $La_{2/3-x}Li_{3x}TiO_3$ (LLTO) family discovered by Inaguma *et al*.[9] and is composed of TiO_6 octahedra on the B-site and La^{3+} and Li^+ on the A-site, with alternating La^{3+}

rich and poor layers (Figure 3.1a). The bulk conductivity of LLTO (x = 0.11) is high with a value of 10^{-3} S cm^{-1} at room temperature and an activation barrier of 0.40 eV, showing great potential for use in a solid Li^+ ion battery. Many materials based on LLTO have been made, both by altering the Li^+ content and cations on both sites, with bulk conductivities and activation barriers of 10^{-3}–10^{-5} S cm^{-1} and 0.25–0.40 eV.[1]

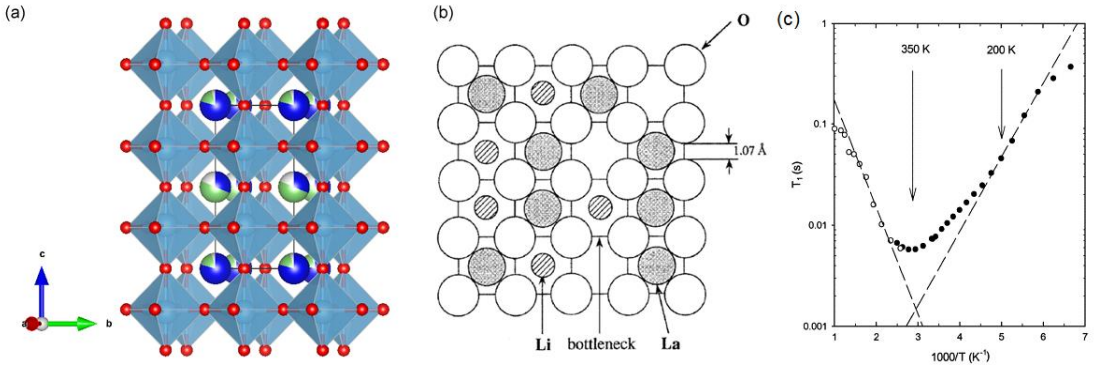

Figure 3.1. (a) Crystal structure of $La_{2/3-x}Li_{3x}TiO_3$ (x = 0.11) with corner sharing TiO_6 octahedra. Atom colours: La (blue), Li (green), Ti (cyan), O (red). Vacancies are shown in white. Structural model taken from Fourquet *et al*.[10] and is plotted in VESTA.[11] (b) Schematic representation of the bottleneck for Li^+ ion conduction. Reproduced with permission from *J. Electrochem. Soc.*, 1995, **142**, L8.[12] Copyright 1995, The Electrochemical Society. (c) Temperature dependence of spin-lattice relaxation time T_1 in $La_{2/3-x}Li_{3x}TiO_3$ (x = 0.11). Dashed lines represent the activation barrier on the low and high temperature flanks of 0.14 and 0.20 eV, respectively. Reprinted from *Solid State Ionics*, 2003, **158**, 119–132,[13] with permission from Elsevier.

Two main properties make LLTO a good Li^+ ion conductor. First, the A-site cations in LLTO have different charges and defects must therefore be introduced to balance the charge. In the case of LLTO, vacant A-sites are

formed. Secondly, due to the small ionic radii of Li^+ (0.59 Å),[14] it is displaced from the centre of the A-site and displays a fourfold coordination.[15] The ionic radii of Li^+ in this coordination sphere is significantly smaller than La^{3+} (1.36 Å),[14] allowing Li^+ to travel through the bottleneck between A-sites (~1.07 Å for an ideal perovskite cell, Figure 3.1b),[12] corresponding to Li^+ diffusion through the material.

Solid-state NMR has been used extensively to understand the Li^+ dynamics in LLTO. NMR relaxometry was used extensively on LLTO with varying Li^+ amounts to identify the best composition. The change in spin-lattice relaxation time T_1 with temperature showed the activation barrier for long range diffusion is 0.20 eV for x = 0.11 (room temperature to 1000 K, Figure 3.1c),[13] lower than the value of 0.26 eV for higher doped x = 0.167 material (350–500 K).[16] The small kink in the T_1 vs. 1000/T plot at 200 K (Figure 3.1c, right arrow) is ascribed to the change in Li^+ mobility from 2D, between the La^{3+} poor layers, to 3D as the bottleneck widen with lattice vibration, allowing Li^+ diffuses between La^{3+} rich and poor layers.[13,17,18]

3.2 NASICONs

Na Superionic Conductor (NASICON) is a crystallographic family discovered by Hagman and Kierkegaard based on the structure $AM_2(PO_4)_3$ (A = Na, M = Ti, Ge, Zr)[19] consisting of alternating corner sharing PO_4 and MO_6 units. The NASICON structure contains two partially occupied A sites – the 6-coordinated A_1 sites and 8-coordinated A_2 with preferential occupancy of the A_1 site.[20] At low temperature, only A_1–A_1 diffusion occurs. At higher temperatures, the framework expands and A_1–A_2 occurs, significantly

increasing conductivity (Figure 3.2b). However, Catti *et al*. denote that since the Li–O distance on the A_2 site are shorter than that of the A_1 site, which signifies higher bond strength. Additionally, the authors state that the role of A_2 in ionic diffusion is possibly minor as confirmed by bond valance calculations which showed significant underbonding of Li on the A_1 site in $LiZr_2(PO_4)_3$.[20] Therefore, although A cation diffusion in NASICONs is assumed to be three dimensional, one could deduce that it is not isotropic as A_1–A_1 and A_1–A_2 diffusion do not occur at the same rate.

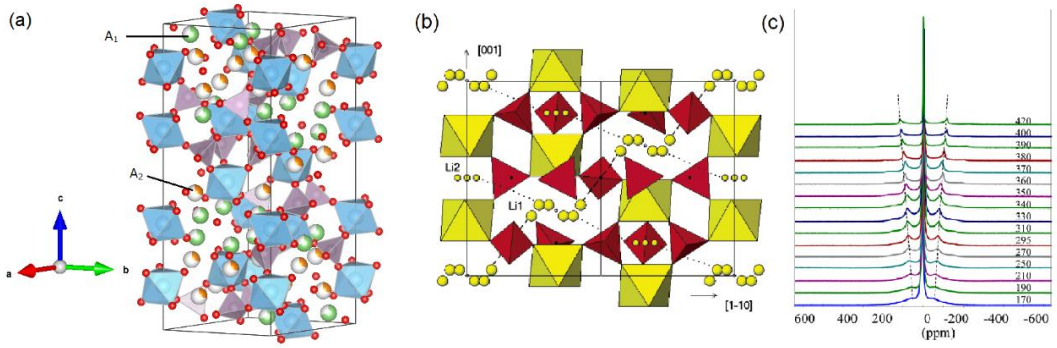

Figure 3.2. (a) Crystal structure of $Li_{1.2}Al_{0.2}Ti_{1.8}(PO_4)_3$. Atom colours: Li (green for A_1 site, orange for A_2 site), Al (grey), Ti (blue), O (red). Vacancies are shown in white. Structural model taken from Arbi *et al*.[31] and is plotted in VESTA.[11] (b) Li diffusion pathway (dotted lines) in $LiZr_2(PO_4)_3$. Yellow spheres are Li on their respective A sites A_1 and A_2; yellow and red polyhedra are ZrO_6 and PO_4, respectively. Adapted with permission from Catti *et al*.[20] Copyright 2003 American Chemical Society. (c) Temperature dependence of 7Li NMR spectra of $Li_{1.3}Al_{0.3}Ti_{1.7}(PO_4)_3$. Widening of the satellite transitions are observed with increasing temperature (in K). Adapted with permission from Emery *et al*.[34,35] Copyright 2003 American Chemical Society.

Li-analogues of these NASICONs have been synthesised by direct

exchange of Na^+ with Li^+ and have shown Li^+ ion conduction and generally showed very low conductivities (10^{-6}–10^{-10} S cm^{-1}), with activation barriers between 0.30–0.43 eV.[21] Out of the series studied, $LiTi_2(PO_4)_3$ (LTP) saw high conductivity of 5 x 10^{-3} S cm^{-1} at 300 ^oC.[22]

Multiple doping on LTP on the Ti site have been studied using M^{3+} (Al^{3+}, Cr^{3+}, Fe^{3+}, Ga^{3+}) and M^{5+} (Ta^{5+}, Nb^{5+}) cations in order to alter Li^+ content and improve room temperature conductivity.[22–26] Out of the combinations, the Al^{3+} doped $Li_{1+x}Al_xTi_{2-x}(PO_4)_3$ (LATP) series ($0 < x < 0.5$) was found to have the highest conductivity.[25,27] The phases with the highest bulk conductivity was found to be between x = 0.3 and 0.5 with values of 4~6 x 10^{-3} S cm^{-1} at room temperature, as the additional Li^+ sits on an additional site (labelled A_3) along the conduction pathway of the A_1, distorting Li^+ on the A_1 sites, and shortening the Li–Li distance.[26,28] For the x = 0.3 sample, activation barriers of 0.20 and 0.35 eV for temperatures above and below 473 K, respectively.[27]

Many compositions of NASICONs, especially the LATP family, have been studied using solid-state NMR spectroscopy. In LTP, París *et al*.[29] identified the preferential occupation of the 6-coordinated A_1 site by Li^+ by comparing the calculated and experimental dipole-dipole moments between Li and other spin – a this observation is in agreement with other NASICON phases determined using neutron diffraction.[20,30,31] Doping of LTP with Al^{3+} in the $0.0 \leq x \leq 1.0$ range studied by Chandran *et al*. [32] show an increase in lithium mobility up to x = 0.35 and 0.5, observed in both line-narrowing experiments and relaxometry experiments, with the lowest activation barrier and temperature of the maxima in the BPP curve observed for these two compositions (0.29 eV and 213 K for both), in agreement with observation in

impedance studies.[28] For x = 0.10, authors report two spin-lattice relaxation curves, and a broad BPP curve in x = 0.20, which is reported as two diffusion processes existing in LATP which are assigned to A_1 Li diffusing between interstitial sites, generated with an increase in Al^{3+} content, which are in agreement by the study by París *et al*.[29] and Epp *et al*.[33] However, the latter also shows that for LATP (x = 0.5) synthesised via sol-gel, as opposed to the conventional solid-state route, the activation barrier for the high temperature flank was lower (0.16 eV) and two diffusion processes are observed. Chandran *et al*. discusses this as different levels of defects or vacancies in the LATP system generated through the different synthesis methods.[32]

Further details in the LATP structure were studied by Emery *et al*.[34,35] The authors state that the addition of Al^{3+} distorts the PO_4 tetrahedra by altering the P–O bond lengths, and in turn the NASICON framework, widening the oxygen cage surrounding Li. As temperature is increased the distortion of the PO_4 tetrahedra and the framework increased. The authors found that the ^{7}Li satellite transitions widened, signifying an increase of the quadrupolar coupling constant C_Q when the opposite is expected caused by averaging of the quadrupolar interactions in ^{7}Li (Figure 3.2c). The authors state that this results from anisotropic motion of Li, which is in agreement with the observation made by Catti *et al*. in $LiZr_2(PO_4)_3$.[20]

3.3 Olivines

Olivine materials have a general formula of $ABXO_4$, and consists of edge sharing AO_6, corner sharing BO_6 and corner sharing XO_4 tetrahedra. Materials in this family, namely $LiFePO_4$ and $LiMnPO_4$, have been studied for use as

cathode materials in batteries due to their reversible Li^+ insertion and extraction due to their 1D Li^+ ion transport channels.[36,37]

For olivine type materials to be used as Li^+ ion conductors, the transition metal must be replaced to remove electronic conductivity. One such material is the olivine $LiMgPO_4$ (Figure 3.3a), which was found to have unfavourable Li^+ diffusion properties with high activation barriers (0.8 eV) and low conductivity values of 10^{-12} S cm^{-1} at room tempreature.[38,39] In attempts to improve Li^+ ion diffusivity and conductivity, Rosseinsky *et al*. studied the $Li_{1-x}Mg_{1-x}In_xPO_4$ series ($0 < x < 0.17$) to introduce Li^+ ion vacancies, where the conductivity increased with dopant level up to 10^{-9} S cm^{-1} at $x = 0.17$.[39]

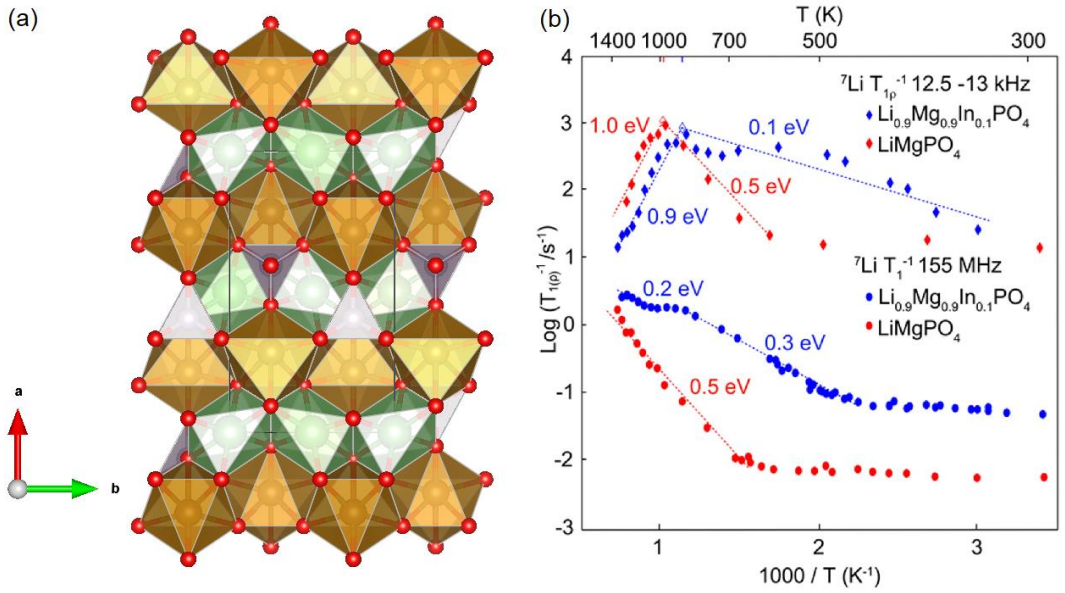

Figure 3.3. (a) Crystal structure of olivine $LiMgPO_4$. Atom colours: Li (green), Mg (brown), P (purple) and O (red). Structural model taken from Amador *et al*.[41] and is plotted in VESTA.[11] (b) Arrhenius plot of ^{7}Li spin-lattice relaxation rates (T_1^{-1} and $T_{1\rho}^{-1}$) of $LiMgPO_4$ and $LiMg_{0.9}In_{0.1}PO_4$. Reprinted with permission from Enciso-Maldonado *et al*.[39] Copyright 2015 American Chemical Society.

Static variable temperature ^{7}Li NMR was used to study $LiMgPO_4$ and $Li_{0.9}Mg_{0.9}In_{0.1}PO_4$ (Figure 3.3b).[39] The onset of Li^+ mobility in ^{7}Li NMR line width analysis in the In-doped olivine was found to occur at 470 K, a significantly lower temperature compared to the undoped material (750 K), highlighting much improved Li^+ mobility. ^{7}Li relaxometry also showed significant decrease in activation barrier on the low temperature flank responsible for uncorrelated local hopping of the mobile ion. Above the $T_{1\rho}^{-1}$ maximum, the activation barrier for long range diffusion is very similar for both doped and undoped material at ~0.9 and ~1.0 eV, respectively. The authors find that this value is close to the sum of the calculated trapping enthalpy of the dopant and hopping barrier. They conclude that the improved yet still low conductivity and Li^+ diffusion in $Li_{0.9}Mg_{0.9}In_{0.1}PO_4$, compared to other Li^+ ion conductor families, is caused by In^{3+} trapping the Li^+ ion channel, which is also observed in the olivine $LiFeO_4$.[40]

3.4 Garnets

These Li^+ ion conductors derive from the ideal garnet crystal structure with the general formula of $A_3B_2(XO_4)_3$, where A-sites, B sites and X-sites have 6-fold, 8-fold and 4-fold coordination, respectively. Li containing garnets $Li_5La_3M_2O_{12}$ (M = Nb, Ta)[42] and cubic $Li_7La_3Zr_2O_{12}$ (LLZO)[43] (Figure 3.4a) were initially studied as potential Li^+ ion conductors. Out of the compositions studied, cubic LLZO looked the most promising, owing to its low activation barrier to Li^+ ion diffusion (~0.34 eV) with a room temperature conductivity of ~5 x 10^{-4} S cm^{-1}, however it was found difficult to reproduce due to the presence of a tetragonally distorted modification of LLZO[44] which has a significantly lower

conductivity of 10^{-7} S cm^{-1} compared to the cubic phase. Doping LLZO with aluminium increases the room temperature stability of the cubic phase,[45–48] which lead to an increase in conductivity, matching the original LLZO values.[47]

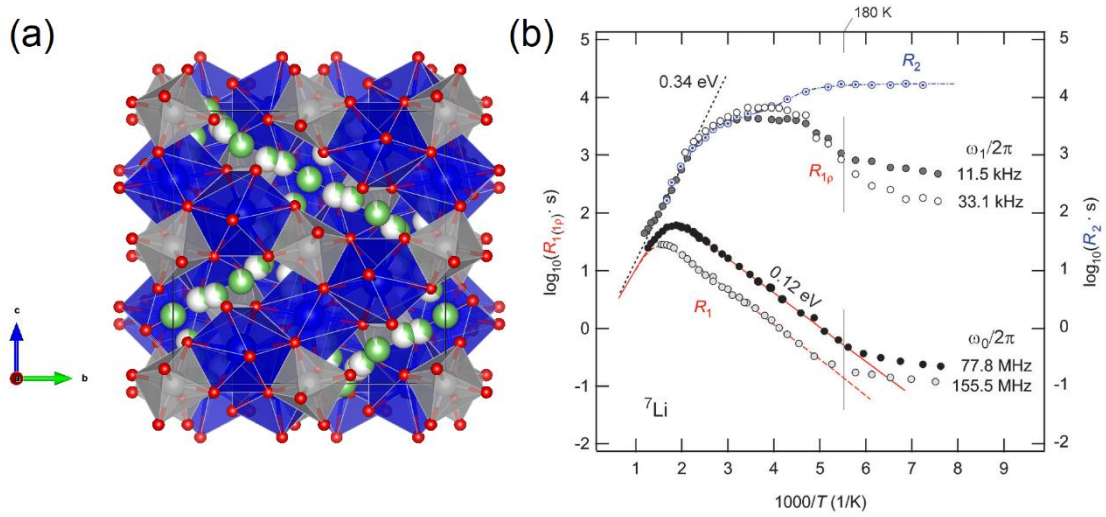

Figure 3.4. (a) Crystal structure of cubic $Li_7La_3Zr_2O_{12}$. Atom colours: Li (green), La (blue), Zr (grey), O (red). Vacancies are shown in white. Structural model taken from Awaka *et al*.[52] and is plotted in VESTA.[11] (b) Temperature dependence of spin-spin ($R_2 = T_2^{-1}$) and spin-lattice relaxation rates ($R_{1(\rho)} = T_{1(\rho)}^{-1}$) of cubic $Li_7La_3Zr_2O_{12}$. Reproduced from Buschman *et al.*[47] with permission from the PCCP Owner Societies.

Kuhn *et al*.[49] studied these phases by solid-state NMR and found low Li^+ diffusivity in tetragonal LLZO with an activation barrier of ~0.50 eV through the use of SLR techniques, similar to the value probed by impedance spectroscopy.[44] On the aluminium containing LLZO samples, the activation barrier to Li^+ diffusion was considerably lower (0.34 eV) and matched the value found in the original LLZO study (Figure 3.4b). Buschmann *et al*. found the ^{7}Li NMR line shape partially narrows with increasing temperature, signifying a two

component ^{7}Li line shape with different Li^{+} mobility, which has also been observed in $Li_5La_3Nb_2O_{12}$ by Koch and Vogel.[50]

The current best garnet Li^{+} ion conductor is the Ga-doped LLZO sample $La_3Zr_2Li_{6.55}Ga_{0.15}O_{12}$ synthesised by Kilner *et al*.[51] The authors used ^{71}Ga solid-state NMR to identify the Ga site, which was found to sit in an axial symmetric tetrahedral hole, expected in a cubic garnet. ^{7}Li and ^{1}H solid-state NMR was used to monitor the effect of moisture uptake. LiOH formation was observed and the increase in ^{7}Li T_1 was attributed to topotactic exchange of Li^{+} and H^{+} ions.

3.5 LISICONs

Lithium Super Ionic Conductors (LISICONs), although similar in its name, has a completely different structure to NASICONs. The first LISICON $Li_{14}Zn(GeO_4)_4$ was reported by Hong during the study of the $Li_{16-2x}M^{II}_x(M^{IV}O_4)_4$ compositions (M^{2+} = Mg^{2+}, Zn^{2+}; M^{4+} = Si^{4+}, Ge^{4+}) ($1 < x < 3$) and has a conductivity value of 0.13 S cm^{-1} at 300 ^{o}C.[53] The framework of LISICONs is the same as γ-Li_3PO_4 and consists of a hexagonal closed packed array of corner sharing $M^{2+}O_4$ and $M^{4+}O_4$ tetrahedra. One of the most common LISICON materials is the solid solution Li_4SiO_4–Li_3PO_4, where multiple orders of magnitude increase in conductivity is observed in both directions towards equal molar amount of each.[54–56]

Solid-state NMR has been used to study the $[1-z]Li_4SiO_4$–$[z]Li_3PO_4$ system (where z is the molar content of each material).[56] ^{6}Li MAS NMR of the $z = 0.25$ sample shows the presence of LiO_3, LiO_4, LiO_5 and LiO_6 environments, as seen in Li_4SiO_4.[57] The peaks coalesce into a single peak at $z = 0.5$, and at

z = 0.75 multiple resonances are observed. Variable temperature ^{7}Li relaxometry experiments show z = 0.25 of having the lowest activation barrier compared to the other compositions studied.

Small aluminium ($0.7Li_{4-3y}Al_ySiO_4$–$0.3Li_3PO_4$, y = 0.01, 0.05, 0.1) and boron doping (0.5~5 wt% Li_2CO_3/H_3BO_3 mixture in $0.4Li_4SiO_4$–$0.6Li_3PO_4$) of the Li_4SiO_4–Li_3PO_4 series have been found to increase conductivity.[58,59] The latter was studied by solid-state NMR to understand the role of boron by Wang *et al*.[60] ^{11}B NMR was used to identify that two boron environments present – at 20 ppm with second order quadrupolar broadening assigned as the BO_3 residing at the grain boundary, and a narrow peak at 2 ppm assigned to BO_4 within the bulk on the PO_4/SiO_4 site. The authors conclude that the BO_3 at the grain boundary acted as a sintering assistant, increasing the density of the pellets used for impedance measurements, which increased the ionic conductivity.

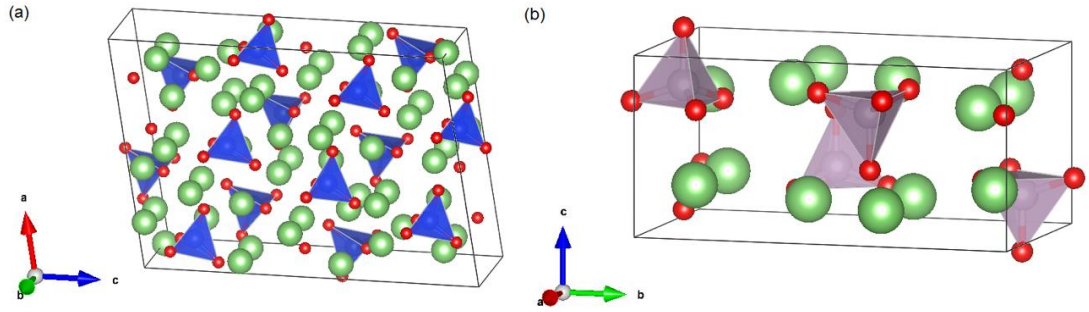

Figure 3.5. Crystal structures of (a) Li_4SiO_4 and (b) γ-Li_3PO_4. Atom colours: Li (green), Si (blue), P (purple), O (red). Structural models were taken from Tranqui *et al*.[61] and Wang *et al*.,[62] and is plotted in VESTA.[11]

3.6 Thio-LISICONs

Thio-LISICONs are a group based on the LISICON family, where O^{2-} is

replaced with S^{2-} to improve ionic conductivity due to its larger ionic radii and higher polarizability characteristics.[2,63–65] This anion replacement reduces the Li^+ interaction with the framework and increases the channel size, easing ion transport in the material.[65]

One of the best thio-LISICON reported is $Li_{10}GeP_2S_{12}$ (LGPS) by Kanno *et al*., which exhibits a very high conductivity of 1.2 x 10^{-2} S cm^{-1} at room temperature,[66] matching or possibly surpassing liquid-state electrolytes.[3] The structure consists of two isolated tetrahedra residing in two different crystallographic sites – one fully occupied with PS_4 and the other with a 1:1 ratio of PS_4 and GeS_4 (Figure 3.6a).[3,66] Further analogues of LGPS have been synthesised by replacing Ge with Si and Sn, which have shown similar conductivity values.[67,68]

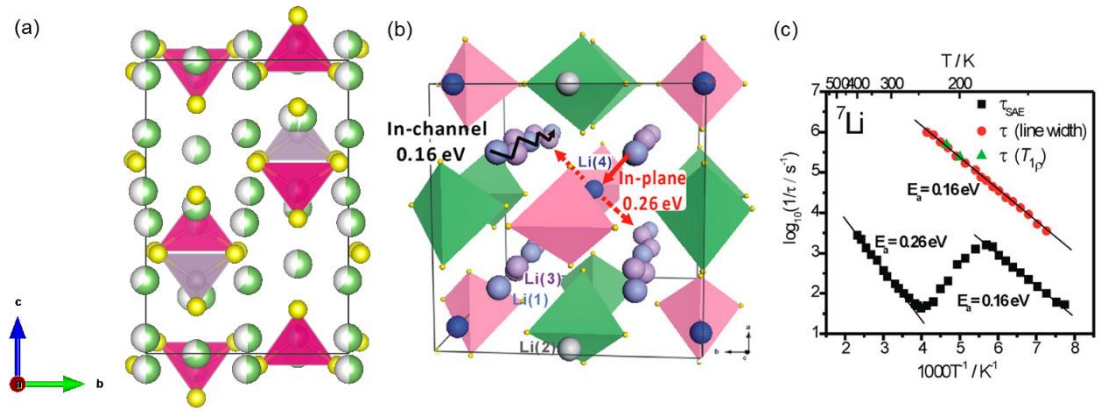

Figure 3.6. (a) Crystal structure of $Li_{10}GeP_2S_{12}$. Atom colours: Li (green), Ge (pink), P (purple), S (yellow). Pink tetrahedra denote the $(Ge/P)S_4$ tetrahedra site. Vacancies are shown in white. Structural model taken from Weber *et al*.[74] and is plotted in VESTA.[11] (b) Labelled structure of $Li_{10}GeP_2S_{12}$ with the Li^+ diffusion pathways labelled. (c) Li^+ jump rates τ^{-1} probed by ^{6}Li and ^{7}Li spin alignment echo, ^{7}Li spin-lock spin-lattice relaxation NMR and ^{7}Li line width analysis. (b) and (c) are reprinted with permission from Liang *et al*.[71] Copyright

2015 American Chemical Society.

The LGPS family has been studied thoroughly using solid-state NMR spectroscopy.[69–72] Kuhn *et al*. studied the Li^+ dynamics of multiple compositions of LGPS and its Si/Sn variants using NMR relaxometry and pulse-field gradient (PFG) NMR.[69,70] They report that $Li_{11}Si_2PS_{12}$ has the lowest activation barrier of the series studied (0.19(1) eV), followed by $Li_{10}GeP_2S_{12}$ (0.21(1) eV), then $Li_{10}SnP_2S_{12}$ (0.23(1) eV), which are in agreement with computational studies of these phases.[73] Liang *et al*. used ^6Li, ^7Li and ^{31}P NMR relaxometry and PFG NMR to study the Li^+ diffusive pathway in LGPS.[71] The authors identify an anisotropic 3D Li^+ diffusion network using multiple NMR techniques, consisting of a combination of an ultrafast 1D diffusion channel of 0.16 eV probed by ^7Li line width and $T_{1\rho}^{-1}$ relaxometry and an in-plane 2D pathway of 0.26 eV by PFG NMR (Figure 3.6b and c). The authors also suggest the activation barriers obtained by other NMR and non-NMR methods are an average of the 1D and 2D processes.

3.7 Argyrodites

Argyrodites are a family of Li^+ ion conductors with general formula of Li_6PS_5X (X = Cl, Br, I) based on the mineral on the argyrodite Ag_8GeS_6 and has high ionic conductivities ranging between 10^{-2}–10^{-3} S cm^{-1}.[75] The structure consists of layers of isolated PS_4 tetrahedra and X^-, with layer of isolated S^{2-} and Li^+ sites in between (Figure 3.7a).

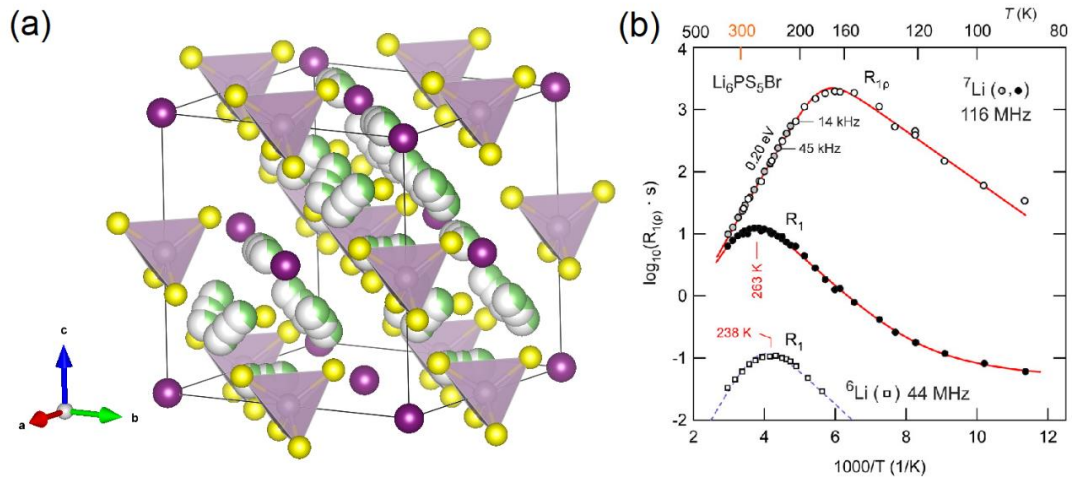

Figure 3.7. (a) Crystal structure of Li_6PS_5I. Atom colours: Li (green), P (purple), S (yellow), I (violet). Vacancies are shown in white. Structural model taken from Deoseroth *et al*.[75] and is plotted in VESTA.[11] (b) Arrhenius plot of ^6Li and ^7Li NMR relaxation rates T_1^{-1} and $T_{1\rho}^{-1}$ of Li_6PS_5Br. Reprinted with permission from Epp *et al*.[77] Copyright 2013 American Chemical Society.

Initial solid-state NMR studies were performed by Deiseroth *et al.*[75] ^{31}P MAS NMR of Li_6PS_5Cl, Li_6PS_5Br and Li_6PS_5I showed multiple phosphorus environments within the argyrodite. From the line shape of each composition, the authors concluded that Li_6PS_5Cl is fully disordered, Li_6PS_5I is fully ordered and Li_6PS_5Br has both ordered and disordered phases, complemented by NMR of the respective halides.

Variable temperature static ^7Li NMR were performed on these samples to study their Li^+ dynamics.[75–77] Deiseroth *et al*. identified the bromine sample as having the highest Li^+ mobility out of the halide compounds using ^7Li line width analysis,[75] which were complemented by impedance studies done by Rao and Adams.[78] ^7Li NMR relaxometry on Li_6PS_5Br showed a small activation barrier for 3D Li^+ long range diffusion of 0.20(2) eV and a $T_{1\rho}^{-1}$ and T_1^{-1}

maximum at 167 and 263 K, respectively (Figure 3.7b). The Li^+ jump rate derived here is converted into conductivity values by the Einstein-Smolchowski and Nernst-Einstein equations, and was found to be on the order of 10^{-2} S cm^{-1}, illustrating extremely fast Li^+ diffusion in Li_6PS_5Br.[77]

Deiseroth *et al*. also noted the sharp increase in ^7Li NMR line width at low temperatures for the iodide compound.[75] This was later identified as a solid-solid phase transition occurring at 177 ± 2 K through variable temperature ^{127}I NMR and dynamic scanning calorimetry studies on the iodide phase.[76]

3.8 Summary and Outlook

The reported conductivities of the representative Li^+ ion conductor for each family is summarised in Table 3.1. Overall, the sulfides have higher conductivity compared to oxide based conductors, as expected from their higher polarizability characteristics. $Li_{10}GeP_2S_{12}$ surpasses the target conductivity value of liquid electrolytes, however other factors must also be taken into consideration when designing Li^+ ion conductors for solid state batteries.

Table 3.1. Reported bulk conductivities and NMR activation barriers of Li^+ ion conductors for each electrolyte family at room temperature.

Crystal Structure	Composition	σ /S cm^{-1}	E_a (NMR) /eV	Ref.
Perovskite	$La_{0.51}Li_{0.34}TiO_{2.94}$	1 x 10^{-3}	0.20	9,13
NASICON	$Li_{1.4}Al_{0.4}Ti_{1.6}(PO_4)_3$	5.6 x 10^{-3}	0.29, 0.16†	28,32,33
Olivine	$Li_{0.9}Mg_{0.9}In_{0.1}PO_4$	1.5 x 10^{-9}	0.9	39
Garnet	"Al-doped" $Li_7La_3Zr_2O_{12}$	4 x 10^{-4}	0.34	47
LISICON	$Li_{3.5}Si_{0.5}P_{0.5}O_4$	1.3 x 10^{-7} *	0.23	56
Thio-LISICON	$Li_{10}GeP_2S_{12}$	1.2 x 10^{-2}	0.21	66,69
Argyrodite	Li_6PS_5Br	6.8 x 10^{-3}	0.20	78
Liquid Electrolyte	1M $LiPF_6$ (50:50 EC/PC)	1 x 10^{-2}		79

* Value extrapolated from higher temperatures to low temperatures, reported by Bachman *et al*.[3]

† Values from x = 0.5.

The ideal anode material in batteries is Li metal, and therefore the conductors must be stable against it. Sulfide based conductors, including $Li_{10}GeP_2S_{12}$, are not always stable against Li metal and decomposes into an interphase containing Li_2S, Li_3P, Li-Ge alloy.[80] They are also moisture sensitive and produce H_2S, so must be handled in inert atmosphere,[81] which could potentially limit their application. Oxide based conductors are generally more stable,[43,82] however their low room temperature conductivity disadvantages them for use in solid lithium ion batteries.

Another factor that must be taken into consideration is the presence of transition metals in fast Li ion conductors. LLTO and NASICONs show high conductivity values, however both contain Ti^{4+}. During cycling, Ti^{4+} may reduce to Ti^{3+}, introducing electronic conductivity which would short circuit the battery and render the battery unusable. The change in oxidation state may also alter the crystal structure of the electrolyte, and at best, only reduce the capacity. Therefore, stable fast Li ion conductors ideally should have no transition metals, for both safety and structural integrity.

Solid state NMR studies of the conductors discussed show that for the activation barriers for the best Li^+ ion conductors are low at around 0.2 eV. As NMR activation barriers measure the pure Li site-to-site diffusion energy, this suggests that the solid state Li^+ ion conductors have good lithium diffusion properties, but other factors may hinder the overall conductivity of these materials when measured at a longer range with methods such as impedance spectroscopy. These factors include defect formation, Coulomb effects of other cations, blocking of the Li^+ channels and reactions at electrolyte-electrode interfaces.

Whilst the field matures with electrolytes having conductivity values approaching those found in liquid electrolytes, further studies must be performed to achieve the desired Li^+ ion conductor, especially in the Li metal-electrolyte interface without sacrificing performance. One such approach to this is to synthesise new materials with previously undiscovered crystal structures. Newly synthesised materials based on the perovskite structure, NASICON structure and thio-LISICONs have been studied and will be discussed in the subsequent chapters.

3.9 References

1 S. Stramare, V. Thangadurai and W. Weppner, *Chem. Mater.*, 2003, **15**, 3974–3990.

2 P. Knauth, *Solid State Ionics*, 2009, **180**, 911–916.

3 J. C. Bachman, S. Muy, A. Grimaud, H.-H. Chang, N. Pour, S. F. Lux, O. Paschos, F. Maglia, S. Lupart, P. Lamp, L. Giordano and Y. Shao-Horn, *Chem. Rev.*, 2016, **116**, 140–162.

4 Y.-X. Xiang, G. Zheng, G. Zhong, D. Wang, R. Fu and Y. Yang, *Solid State Ionics*, 2018, **318**, 19–26.

5 Z. Zhang, Y. Zhu, Y. Zhong, W. Zhou and Z. Shao, *Adv. Energy Mater.*, 2017, **7**, 1700242.

6 X. Lü, G. Wu, J. W. Howard, A. Chen, Y. Zhao, L. L. Daemen and Q. Jia, *Chem. Commun.*, 2014, **50**, 11520–11522.

7 M. Wu, B. Xu, X. Lei, K. Huang and C. Ouyang, *J. Mater. Chem. A*, 2018, **6**, 1150–1160.

8 J. A. Dawson, T. S. Attari, H. Chen, S. P. Emge, K. E. Johnston and M. S. Islam, *Energy Environ. Sci.*, 2018, **11**, 2993–3002.

9 Y. Inaguma, C. Liquan, M. Itoh, T. Nakamura, T. Uchida, H. Ikuta and M. Wakihara, *Solid State Commun.*, 1993, **86**, 689–693.

10 J. L. Fourquet, H. Duroy and M. P. Crosnier-Lopez, *J. Solid State Chem.*, 1996, **127**, 283–294.

11 K. Momma and F. Izumi, *J. Appl. Crystallogr.*, 2011, **44**, 1272–1276.

12 Y. Inaguma, J. Yu, Y. Shan, M. Itoh and T. Nakamuraa, *J. Electrochem. Soc.*, 1995, **142**, L8.

13 O. Bohnke, J. Emery and J. L. Fourquet, *Solid State Ionics*, 2003, **158**,

119–132.

14 R. D. Shannon, *Acta Crystallogr. Sect. A*, 1976, **A32**, 751–767.

15 A. Rivera and J. Sanz, *Phys. Rev. B*, 2004, **70**, 94301.

16 W. Bucheli, K. Arbi, J. Sanz, D. Nuzhnyy, S. Kamba, A. Várez and R. Jimenez, *Phys. Chem. Chem. Phys.*, 2014, **16**, 15346–15354.

17 J. Emery, O. Bohnké, J. L. Fourquet, J. Y. Buzaré, P. Florian and D. Massiot, *J. Phys. Condens. Matter*, 2002, **14**, 523–539.

18 O. Bohnke, *Solid State Ionics*, 2008, **179**, 9–15.

19 L. O. Hagman and P. Kierkegaard, *Acta Chem. Scand.*, 1968, **22**, 1822–1832.

20 M. Catti, A. Comotti and S. Di Blas, *Chem. Mater.*, 2003, **15**, 1628–1632.

21 H. Aono, E. Sugimoto, Y. Sadaoka, N. Imanaka and G. Adachi, *J. Electrochem. Soc.*, 1993, **140**, 1827–1833.

22 M. Subramanian, R. Subramanian and A. Clearfield, *Solid State Ionics*, 1986, **18**–**19**, 562–569.

23 H. Yamamoto, M. Tabuchi, T. Takeuchi and O. Nakamura, *J. Power Sources*, 1997, **68**, 397–401.

24 V. Thangadurai, A. K. Shukla and J. Gopalakrishnan, *J. Mater. Chem.*, 1999, **9**, 739–741.

25 K. Arbi, M. G. Lazarraga, D. Ben Hassen Chehimi, M. Ayadi-Trabelsi, J. M. Rojo and J. Sanz, *Chem. Mater.*, 2004, **16**, 255–262.

26 K. Arbi, J. M. Rojo and J. Sanz, *J. Eur. Ceram. Soc.*, 2007, **27**, 4215–4218.

27 H. Aono, E. Sugimoto, Y. Sadaoka, N. Imanaka and G.-Y. Adachi, *J. Electrochem. Soc.*, 1990, **137**, 1023–1027.

28 D. Rettenwander, A. Welzl, S. Pristat, F. Tietz, S. Taibl, G. J. Redhammer and J. Fleig, *J. Mater. Chem. A*, 2016, **4**, 1506–1513.

29 M. A. París, A. Martínez-Juárez, J. M. Rojo and J. Sanz, *J. Phys. Condens. Matter*, 1996, **8**, 5355–5366.

30 D. T. Qui, S. Hamdoune, J. L. Soubeyroux and E. Prince, *J. Solid State Chem.*, 1988, **72**, 309–315.

31 K. Arbi, M. Hoelzel, A. Kuhn, F. García-Alvarado and J. Sanz, *Phys. Chem. Chem. Phys.*, 2014, **16**, 18397–18405.

32 C. Vinod Chandran, S. Pristat, E. Witt, F. Tietz and P. Heitjans, *J. Phys. Chem. C*, 2016, **120**, 8436–8442.

33 V. Epp, Q. Ma, E.-M. Hammer, F. Tietz and M. Wilkening, *Phys. Chem. Chem. Phys.*, 2015, **17**, 32115–32121.

34 J. Emery, T. Šalkus, A. Abramova, M. Barré and A. F. Orliukas, *J. Phys. Chem. C*, 2016, **120**, 26173–26186.

35 J. Emery, T. Šalkus and M. Barré, *J. Phys. Chem. C*, 2016, **120**, 26235–26243.

36 A. K. Padhi, K. S. Nanjundaswamy and J. B. Goodenough, *J. Electrochem. Soc.*, 1997, **144**, 1188–1194.

37 K. Zaghib, A. Guerfi, P. Hovington, A. Vijh, M. Trudeau, A. Mauger, J. B. Goodenough and C. M. Julien, *J. Power Sources*, 2013, **232**, 357–369.

38 R. Jalem, T. Aoyama, M. Nakayama and M. Nogami, *Chem. Mater.*, 2012, **24**, 1357–1364.

39 L. Enciso-Maldonado, M. S. Dyer, M. D. Jones, M. Li, J. L. Payne, M. J. Pitcher, M. K. Omir, J. B. Claridge, F. Blanc and M. J. Rosseinsky, *Chem. Mater.*, 2015, **27**, 2074–2091.

40 A. Goñi, T. J. Bonagamba, M. A. Silva, H. Panepucci, T. Rojo and G. E. Barberis, *J. Appl. Phys.*, 1998, **84**, 416–421.

41 O. García-Moreno, M. Alvarez-Vega, J. García-Jaca, J. M. Gallardo-Amores, M. L. Sanjuán and U. Amador, *Chem. Mater.*, 2001, **13**, 1570–1576.

42 V. Thangadurai, H. Kaack and W. J. F. Weppner, *J. Am. Ceram. Soc.*, 2003, **86**, 437–440.

43 R. Murugan, V. Thangadurai and W. Weppner, *Angew. Chemie Int. Ed.*, 2007, **46**, 7778–7781.

44 J. Awaka, N. Kijima, H. Hayakawa and J. Akimoto, *J. Solid State Chem.*, 2009, **182**, 2046–2052.

45 C. A. Geiger, E. Alekseev, B. Lazic, M. Fisch, T. Armbruster, R. Langner, M. Fechtelkord, N. Kim, T. Pettke and W. Weppner, *Inorg. Chem.*, 2011, **50**, 1089–1097.

46 A. Düvel, A. Kuhn, L. Robben, M. Wilkening and P. Heitjans, *J. Phys. Chem. C*, 2012, **116**, 15192–15202.

47 H. Buschmann, J. Dölle, S. Berendts, A. Kuhn, P. Bottke, M. Wilkening, P. Heitjans, A. Senyshyn, H. Ehrenberg, A. Lotnyk, V. Duppel, L. Kienle and J. Janek, *Phys. Chem. Chem. Phys.*, 2011, **13**, 19378.

48 J.-M. Lee, T. Kim, S.-W. Baek, Y. Aihara, Y. Park, Y.-I. Kim and S.-G. Doo, *Solid State Ionics*, 2014, **258**, 13–17.

49 A. Kuhn, S. Narayanan, L. Spencer, G. Goward, V. Thangadurai and M. Wilkening, *Phys. Rev. B - Condens. Matter Mater. Phys.*, 2011, **83**, 1–11.

50 B. Koch and M. Vogel, *Solid State Nucl. Magn. Reson.*, 2008, **34**, 37–

43.

51 C. Bernuy-Lopez, W. Manalastas, J. M. Lopez Del Amo, A. Aguadero, F. Aguesse and J. A. Kilner, *Chem. Mater.*, 2014, **26**, 3610–3617.

52 J. Awaka, A. Takashima, K. Kataoka, N. Kijima, Y. Idemoto and J. Akimoto, *Chem. Lett.*, 2011, **40**, 60–62.

53 H. Y.-P. Hong, *Mater. Res. Bull.*, 1978, **13**, 117–124.

54 Y.-W. Hu, I. D. Raistrick and R. A. Huggins, *J. Electrochem. Soc. Solid-State Sci. Technol.*, 1977, **124**, 1240–1242.

55 R. D. Shannon, B. E. Taylor, A. D. English and T. Berzins, *Electrachimica Acta*, 1977, **22**, 783–796.

56 Y. Deng, C. Eames, J.-N. Chotard, F. Lalère, V. Seznec, S. Emge, O. Pecher, C. P. Grey, C. Masquelier and M. S. Islam, *J. Am. Chem. Soc.*, 2015, **137**, 9136–9145.

57 Z. Xu and J. F. Stebbins, *Solid State Nucl. Magn. Reson.*, 1995, **5**, 103–112.

58 J. Choi and J. Lee, *Solid State Ionics*, 2016, **289**, 173–179.

59 L. Zhang, L. Cheng, J. Cabana, G. Chen, M. M. Doeff and T. J. Richardson, *Solid State Ionics*, 2013, **231**, 109–115.

60 D. Wang, G. Zhong, Y. Li, Z. Gong, M. J. McDonald, J.-X. Mi, R. Fu, Z. Shi and Y. Yang, *Solid State Ionics*, 2015, **283**, 109–114.

61 D. Tranqui, R. D. Shannon, H. Y. Chen, S. Iijima and W. H. Baur, *Acta Crystallogr. Sect. B Struct. Crystallogr. Cryst. Chem.*, 1979, **35**, 2479–2487.

62 B. Wang, B. C. Chakoumakos, B. C. Sales, B. S. Kwak and J. B. Bates, *J. Solid State Chem.*, 1995, **115**, 313–323.

63 R. Kanno, T. Hata, Y. Kawamoto and M. Irie, *Solid State Ionics*, 2000, **130**, 97–104.

64 R. Kanno and M. Murayama, *J. Electrochem. Soc.*, 2001, **148**, A742–A746.

65 R. Chen, W. Qu, X. Guo, L. Li and F. Wu, *Mater. Horiz*, 2016, **3**, 487–516.

66 N. Kamaya, K. Homma, Y. Yamakawa, M. Hirayama, R. Kanno, M. Yonemura, T. Kamiyama, Y. Kato, S. Hama, K. Kawamoto and A. Mitsui, *Nat. Mater.*, 2011, **10**, 682–686.

67 P. Bron, S. Johansson, K. Zick, J. S. A. Der Günne, S. Dehnen and B. Roling, *J. Am. Chem. Soc.*, 2013, **135**, 15694–15697.

68 J. M. Whiteley, J. H. Woo, E. Hu, K.-W. Nam and S.-H. Lee, *J. Electrochem. Soc.*, 2014, **161**, A1812–A1817.

69 A. Kuhn, V. Duppel and B. V. Lotsch, *Energy Environ. Sci.*, 2013, **6**, 3548.

70 A. Kuhn, O. Gerbig, C. Zhu, F. Falkenberg, J. Maier and B. V. Lotsch, *Phys. Chem. Chem. Phys.*, 2014, **16**, 14669–14674.

71 X. Liang, L. Wang, Y. Jiang, J. Wang, H. Luo, C. Liu and J. Feng, *Chem. Mater.*, 2015, **27**, 5503–5510.

72 M. C. Paulus, M. F. Graf, P. P. R. M. L. Harks, A. Paulus, P. P. M. Schleker, P. H. L. Notten, R.-A. Eichel and J. Granwehr, *J. Magn. Reson.*, 2018, **294**, 133–142.

73 S. P. Ong, Y. Mo, W. D. Richards, L. Miara, H. S. Lee and G. Ceder, *Energy Environ. Sci.*, 2013, **6**, 148–156.

74 D. A. Weber, A. Senyshyn, K. S. Weldert, S. Wenzel, W. Zhang, R. Kaiser, S. Berendts, J. Janek and W. G. Zeier, *Chem. Mater.*, 2016, **28**,

5905–5915.

75 H.-J. Deiseroth, S.-T. Kong, H. Eckert, J. Vannahme, C. Reiner, T. Zaiß and M. Schlosser, *Angew. Chemie Int. Ed.*, 2008, **47**, 755–758.

76 O. Pecher, S.-T. Kong, T. Goebel, V. Nickel, K. Weichert, C. Reiner, H.-J. Deiseroth, J. Maier, F. Haarmann and D. Zahn, *Chem. - A Eur. J.*, 2010, **16**, 8347–8354.

77 V. Epp, Ö. Gün, H.-J. Deiseroth and M. Wilkening, *J. Phys. Chem. Lett.*, 2013, **4**, 2118–2123.

78 R. P. Rao and S. Adams, *Phys. Status Solidi Appl. Mater. Sci.*, 2011, **208**, 1804–1807.

79 P. . Stallworth, J. . Fontanella, M. . Wintersgill, C. D. Scheidler, J. J. Immel, S. . Greenbaum and A. . Gozdz, *J. Power Sources*, 1999, **81**–**82**, 739–747.

80 S. Wenzel, S. Randau, T. Leichtweiß, D. A. Weber, J. Sann, W. G. Zeier and J. Janek, *Chem. Mater.*, 2016, **28**, 2400–2407.

81 H. Muramatsu, A. Hayashi, T. Ohtomo, S. Hama and M. Tatsumisago, *Solid State Ionics*, 2011, **182**, 116–119.

82 J. Wolfenstine, J. L. Allen, J. Read and J. Sakamoto, *J. Mater. Sci.*, 2013, **48**, 5846–5851.

4. Perovskite with Li on both A- and B-sites – $La_3Li_3W_2O_{12}$

The first new material of interest which is reported in this thesis is the double perovskite $La_3Li_3W_2O_{12}$. The work was published in Chemistry of Materials in 2016.[1] and this chapter discusses the NMR contribution to this collaborative work.

A double perovskite is a perovskite that consists of two different cations on the B-site, forming an array of BO_6 and $B'O_6$ octahedron with bridging oxygen in either a rock-salt, layered or columnar order (Figure 4.1).[2] These double perovskites are used widely in a variety of fields including ferromagnets and superconductors. Li containing double perovskites have also been studied where Li is found on the B-site in materials such as $SrLi_{0.4}W_{0.6}O_3$[3] and the La_2LiMO_6 (*M* = V, Nb, Ta, Mo, Re, Ru, Os, Ir and Sb) series,[4–6] as well as perovskites with combinations of Li, Nb and W on the B-site.[7,8] These B-site Li double perovskites are not considered as Li^+ ion conductors due to the lack of obvious Li^+ diffusion pathways between two LiO_6 octahedra, however the distance between adjacent A-site and B-site in an undistorted rock-salt ordered double perovskite is shorter than the distance between neighbouring A-sites. Therefore, a perovskite where Li exists on both A-site and B-site may allow Li^+ diffusion between A-site and B-site, rather than A-site only, This would increase the number of Li^+ transport pathways, which could lead to a possible increase in Li^+ conductivity to match or even surpass that of liquid Li^+ electrolytes.

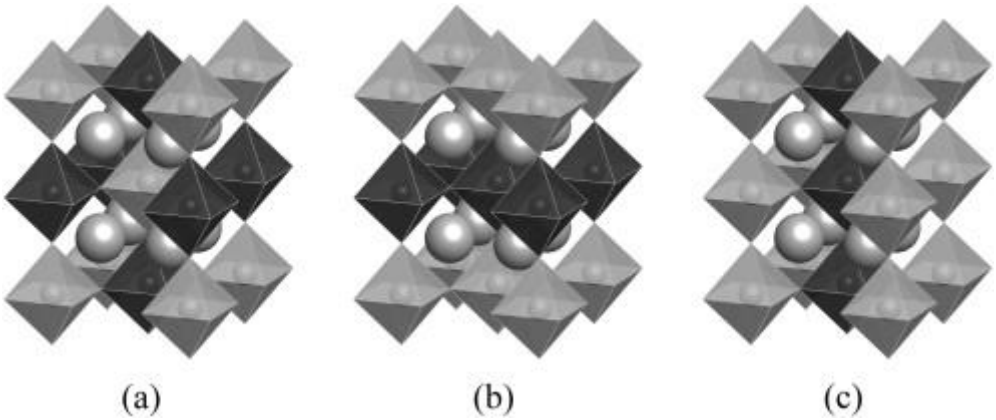

Figure 4.1. Three different types of $BO_6/B'O_6$ octahedra ordering in double perovskites: (a) rock-salt, (b) layered, (c) columnar ordering. Reprinted from *Prog. Solid State Chem.*, 2015, **43**, 1–36, [2] with permission from Elsevier.

$La_3Li_3W_2O_{12}$ is the first reported perovskite with Li present on both the A-site and B-site of the crystal structure. A combination of powder X-ray and neutron diffraction showed the resulting crystal structure of $La_3Li_3W_2O_{12}$ characteristic of cryolite-type double perovskites, which consists of alternating BO_6 octahedra of the different cations with tilted distortion due to the size differences of the LiO_6 and WO_6 octahedral volumes of 12.9 $Å^3$ vs. 9.3 $Å^3$, respectively. However, as the scattering factor on Li is very low, the exact position of A-site Li could not be determined.

DFT calculations of the crystal structure were performed on the experimentally refined structure of $La_3Li_3W_2O_{12}$. The A-site Li was found displaced away from the centre of the A-site, forming a distorted tetrahedron with 4 O atoms (Figure 4.2a, b). Local A-site ordering were investigated and the lower energy structures showed preference to local ordering of Li. This resulted in A-site Li atoms in neighbouring sites on both horizontal and vertical axes and also the presence of fully La occupied A-site layers which may prohibit long range Li diffusion. The three lowest energy DFT configurations

labelled **C1**, **C2**, and **C3** (Figure 4.2c-e) were used to calculate ^{6}Li and ^{17}O NMR parameters using the GIPAW method to aid solid-state NMR investigation.[1]

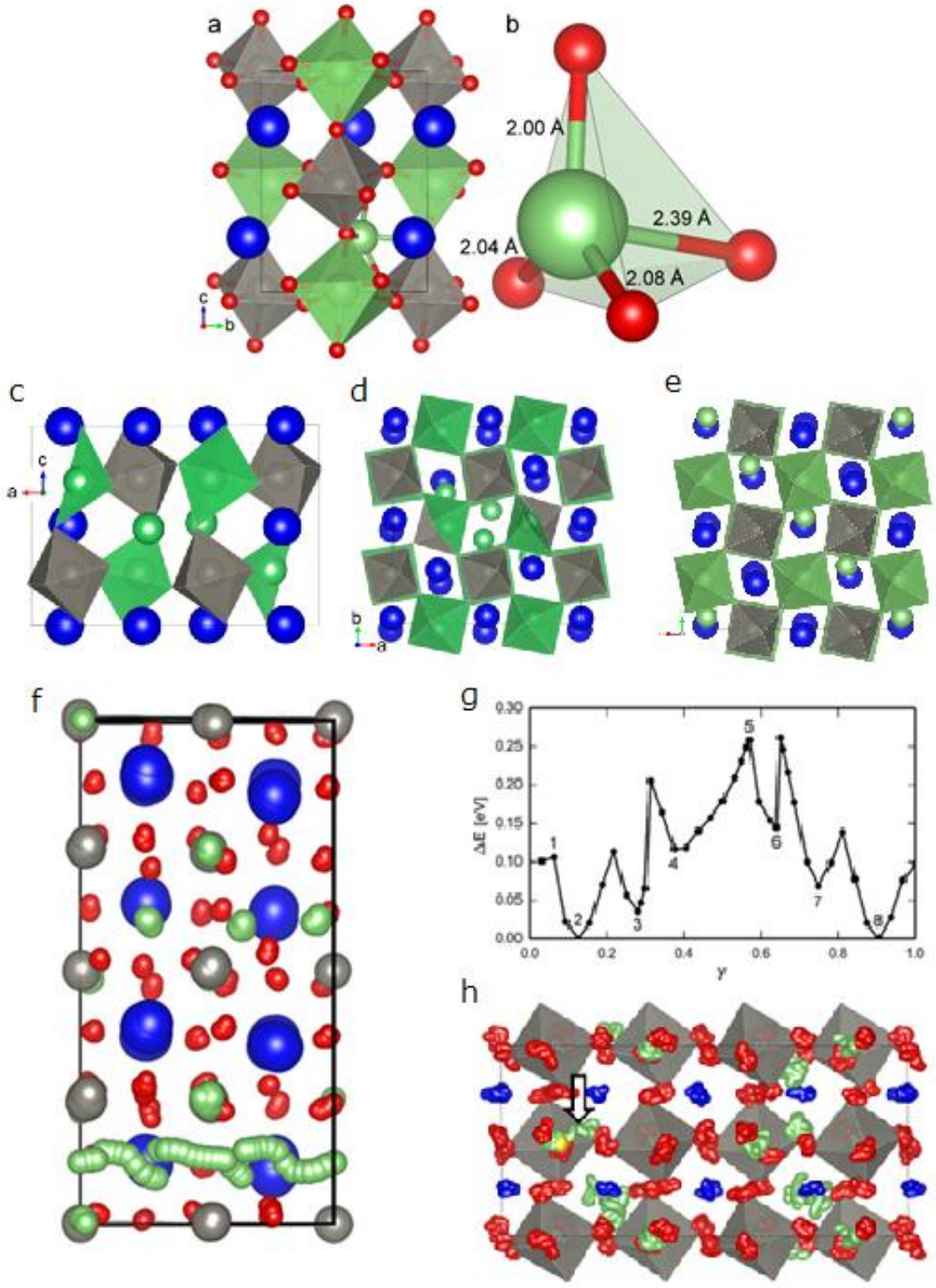

Figure 4.2. (a) Crystal structure of $La_3Li_3W_2O_{12}$ from DFT calculations. (b) The

coordination spheres of A-site Li, highlighting the short Li-O distances of the 4-coordinated A-site Li. (c-e) Lowest DFT configurations of $La_3Li_3W_2O_{12}$ **C1**, **C2** and **C3**, respectively. (f) Atomic positions from each constrained DFT relaxations as A-site Li is moved to the neighbouring A-site, showing the path of Li throughout the diffusive process. (g) The relative energies of each DFT relaxed structure against Li position on the y axis. Numbers denote the $La_3Li_3W_2O_{12}$ structure at those positions, presented in the published paper. (h) AIMD of $La_3Li_3W_2O_{12}$, highlighting the migration of B-site Li to A-site (arrow). Atom colours: La (blue), Li (green), W (grey), O (red). Pie charts denote occupancies of the site. Yellow sphere in (e) denotes the starting position of Li before the AIMD run.

Computational approaches were also used to investigate the Li^+ dynamics of the material. The A-site to A-site Li^+ energy barrier was investigated by performing DFT relaxations along the y axis through the supercell (Figure 4.2f, g). The resulting energy landscape showed Li^+ diffusion between A-sites consists of multiple minima and energy barriers, with the difference between the lowest energy minima and highest point as ~0.25 eV. *Ab initio* molecular dynamics (AIMD) also identified B-site Li migration to an A-site, in addition to A-site to A-site diffusion (Figure 4.2h). The A-site Li is also observed to be highly mobile within its site.

In this chapter, solid state NMR investigation of the new double perovskite $La_3Li_3W_2O_{12}$ is discussed. Structural information is extracted using a combination of ^6Li and ^{17}O MAS NMR, along with some spatial information using ^7Li–^{17}O Heteronuclear Multiple Quantum Correlation (HMQC) NMR.

Comparisons are made with the experimentally determined crystal structure and calculated ^{6}Li and ^{17}O NMR values. Li^{+} dynamics are investigated using variable temperature ^{6}Li exchange spectroscopy (EXSY) MAS NMR and ^{6,7}Li static NMR, and are compared to both AC impedance spectroscopy and *ab* initio molecular dynamics calculations, performed by Dr. J. Felix Shin and Dr. Matthew S. Dyer, respectively.

4.1 Experimental

These $La_3Li_3W_2O_{12}$ samples were studied using solid-state NMR and are labelled as follows:

- $La_3Li_3W_2O_{12}$, synthesised with stoichiometric amounts of La_2O_3, Li_2CO_3 and WO_3 at natural abundance (synthesised by Dr. Christophe Didier and Dr. Michael J. Pitcher).
- $La_3{}^{6}Li_3W_2O_{12}$, synthesised with isotopically ^{6}Li enriched Li_2CO_3 (99.9 % Li, Sigma-Aldrich).
- $La_3Li_3W_2{}^{17}O_{12}$, prepared by gas-solid exchange of $La_3Li_3W_2O_{12}$ with 60% ^{17}O enriched O_2 gas (see below)

Further synthesis details are described in the corresponding publication.[1]

4.1.1 NMR Details

^{6}Li Magic Angle Spinning (MAS) solid-state NMR experiments were carried out on a 9.4 T Bruker Avance III HD spectrometer equipped with a Bruker 4 mm HXY MAS probe (in double resonance mode) tuned to X = ^{6}Li at a Larmor frequency $\nu_0(^{6}Li)$ = 58.88 MHz and on a 20 T Bruker Avance II spectrometer with a Bruker 4 mm HX MAS probe tuned to ^{6}Li at $\nu_0(^{6}Li)$ = 125.11

MHz. ^{6}Li spectra were obtained with a $\pi/2$ pulse length of 3 μs at a radio-frequency (rf) amplitude of $\nu_1(^{6}\text{Li})$ = 83 kHz at a MAS rate of 10 kHz. Additional ^{6}Li MAS NMR spectra were recorded on the same 9.4 T NMR spectrometer with a Bruker 1.3 mm HXY MAS probe at with a $\pi/2$ pulse length of 3 μs at a rf amplitude of $\nu_1(^{6}\text{Li})$ = 83 kHz at a MAS rate of 60 kHz.

^{17}O rotor synchronised Hahn echo and two dimensional (2D) z-filtered Multiple-Quantum MAS (MQMAS)[9–11] experiments were carried out on a 9.4 T Bruker Avance III HD spectrometer with a Bruker 4 mm HXY MAS probe (in double resonance mode) tuned to ^{17}O at $\nu_0(^{17}\text{O})$ = 54.2 MHz and at a MAS rate of 13 kHz, and on a 20 T Bruker Avance II spectrometer with a Bruker 3.2 mm HXY MAS probe (in double resonance mode) tuned to ^{17}O at $\nu_0(^{17}\text{O})$ = 115.3 MHz and at a MAS rate of 20 kHz. ^{17}O spectra were obtained with $\pi/2$ pulse lengths of 1 and 1.2 μs at a rf amplitude of $\nu_1(^{17}\text{O})$ = 83 kHz and 70 kHz at 20 and 9.4 T, respectively. Excitation and reconversion pulses in the 2D ^{17}O 3QMAS NMR experiments were performed at rf amplitude of $\nu_1(^{17}\text{O}) \approx 83$ kHz while the soft $\pi/2$ was obtained at 13 kHz.

^{7}Li observed ^{7}Li–^{17}O dipolar-based heteronuclear multiple quantum correlation (HMQC) experiments (see Chapter 2) were performed on a 20 T Bruker Avance II spectrometer with a Bruker 4 mm HXY MAS probe with the ^{7}Li/^{6}Li configuration under MAS frequency of ν_r = 13 kHz. X channel was tuned to $\nu_0(^{7}\text{Li})$ = 330.4 MHz and Y channel tuned to $\nu_0(^{17}\text{O})$ = 115.2 MHz. Selective pulses of rf field amplitude $\nu_1(^{7}\text{Li})$ = 5 kHz and $\nu_1(^{17}\text{O})$ = 4 kHz were used with 20 μs increments in the F_1 dimension.

Variable temperature ^{6}Li and ^{7}Li solid-state NMR experiments were

obtained at 9.4 T and with $\nu_0(^6Li)$ = 58.88 MHz and $\nu_0(^7Li)$ = 155.51 MHz, respectively. ^6Li exchange spectroscopy (EXSY) experiments (see Chapter 2) were performed with mixing times τ_m up to 1 s with a Bruker 4 mm HXY MAS probe at a MAS rate of 10 kHz at room temperature and 423 K and a 1.3 mm HXY MAS probe at a MAS rate of 60 kHz. Below 650 K, static experiments were conducted on a 9.4 T Bruker Avance III HD spectrometer with a Bruker 4 mm HX high temperature MAS probe (between 294 K and 650 K) and with a Bruker 4 mm HXY MAS probe (in double resonance mode) below 294 K using standard 4 mm ZrO_2 rotors and caps. Above 650 K, static experiments were carried out on a 9.4 T Bruker Avance spectrometer using a single channel high temperature static NMR probe with a homemade CO_2 laser (λ = 10.6 μm, 250 W) heating system developed in Orléans (CNRS – CEMHTI, France).[12,13] The sample was placed in a BN crucible and inserted into the rf coil of the high temperature NMR probe. The sample is heated up by two lasers, passing axially through the NMR probe, with the sample temperature controlled by the laser power output. A flow of N_2 is used to cool the rf coil and a flow of Ar gas to prevent oxidation of the BN crucible at high temperature. ^6Li spectra were obtained with a $\pi/2$ pulse of 3 μs at an rf amplitude of $\nu_1(^6Li)$ = 83 kHz below 650 K and with a $\pi/2$ pulse of 52.5 μs at an rf amplitude of $\nu_1(^6Li)$ = 4.7 kHz above 650 K. ^7Li spectra were obtained with a $\pi/2$ pulse of 2 μs at an rf amplitude of $\nu_1(^7Li)$ = 62.5 kHz below 650 K and with a $\pi/2$ pulse of 8 μs at an rf amplitude of $\nu_1(^7Li)$ = 15 kHz above 650 K. Spin-lattice relaxation times in the laboratory frame (T_1) were obtained using a saturation recovery pulse sequence and the data were fitted to a stretched exponential of the form $1-\exp[-(\tau/T_1)^\alpha]$, where τ are variable delays and α is the stretch exponential

coefficient (between 0.85 and 1). ^{7}Li spin-lattice relaxation times in the rotating frame ($T_{1\rho}$) were obtained with a spin-lock pulse sequence at frequencies of $\nu_1(^{7}Li)$ = 8 and 14 kHz. $T_{1\rho}$ data were fitted to a stretch exponential of the form $\exp[-(\tau/T_{1\rho})^{\alpha}]$. Temperature calibrations of the MAS probes (below 650 K) were performed with the ^{207}Pb chemical shift thermometer of $Pb(NO_3)_2$,[14,15] and by following the ^{63}Cu resonances of Cu^{I}I and Cu^{I}Br across the γ-to-β phase transition at 642 K and 658 K, respectively.[16,17] Temperature calibration of the laser heated NMR probe was carried out by direct measurements of the melting points of reference samples.[12,13] All temperatures reported are actual sample temperatures and have an estimated accuracy of ± 5 K (below 294 K), ± 10 K (between 294 K and 420 K, ± 20 K (between 420 K and 600 K) and ± 30 K (above 600 K on the static laser probe).

Spectra were referenced to 10 M LiCl in D_2O (for ^{6,7}Li shifts) and H_2O (for ^{17}O shifts) at 0 ppm.

4.1.2 ^{17}O enrichment of $La_3Li_3W_2O_{12}$

^{17}O enriched $La_3Li_3W_2O_{12}$ was prepared by a gas-solid exchange reaction with ^{17}O O_2 gas (60 % ^{17}O, Sigma-Aldrich). The sample was placed inside an evacuated quartz tube, and ~3 mL of ^{17}O enriched gas was then inserted. The tube containing $La_3Li_3W_2O_{12}$ and ^{17}O enriched O_2 gas was heated at 600 ^{o}C for 12 hours with heating and cooling rates of 5 ^{o}C/min.

4.1.3 Temperature Stability Testing

Temperature stability testing of $La_3Li_3W_2O_{12}$ on boron nitride under N_2 atmosphere was performed to replicate conditions measured at CEMHTI-

CNRS. $La_3Li_3W_2O_{12}$ powders were studied on a Panalytical X'Pert Pro diffractometer using monochromated Co $K_{\alpha 1}$ radiation (λ = 1.7890 Å) after heating and cooling the powders on a BN pellet. The BN pellet was made by pressing ~0.4 g of BN powder under ~1.5 tons of pressure. ~15 mg of $La_3Li_3W_2O_{12}$ was carefully placed on top of the BN pellet and this was placed on an Al_2O_3 crucible lid and inserted into the centre of the tube furnace. N_2 atmosphere was obtained with a flow of 10 mL/min for 1 hour. The sample was held at the target temperature for 1 hour with heating and cooling rates of 5 °C/min and 10 °C/min, respectively.

4.2 Results

4.2.1 Structural Investigation

4.2.1.1 Identification of two Li sites with ^{6}Li MAS NMR Spectroscopy

The room temperature ^{6}Li MAS NMR spectrum of $La_3Li_3W_2O_{12}$ and $La_3{}^6Li_3W_2O_{12}$ recorded at 9.4 and 20 T at varying MAS rates is presented in Figure 4.3 where two Li environments are clearly observed, and are fitted with two resonances at 0 and –0.4 ppm. Based on the existing relationship between Li–O coordination and shift ($\delta(^6Li) = -0.608 \times CN + 2.91$[18–20]), the latter resonance is assigned to LiO_6 while the former corresponds to a lower coordinate Li environment. Based on the proposed crystal structure of $La_3Li_3W_2O_{12}$, the two resonances at 0 and –0.4 ppm are assigned as the A-site Li and B-site Li respectively. The integral ratios of the peaks are found to be 1:2, consistent with the A:B site Li ratio proposed in the DFT structural model, confirming the presence of two distinctly different Li sites which were

not experimentally detected in X-ray and room temperature neutron diffraction.[1]

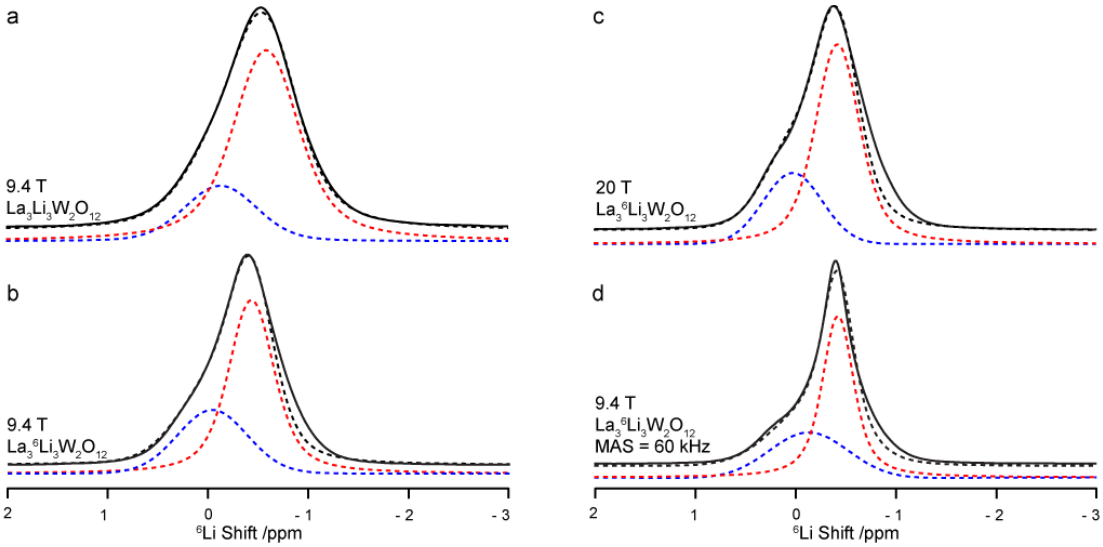

Figure 4.3. ^{6}Li Magic Angle Spinning (MAS) NMR spectra of (a) $La_3Li_3W_2O_{12}$ and (b-d) $La_3{}^{6}Li_3W_2O_{12}$ obtained at magnetic field strengths of 9.4 and 20 T. Black dashes lines represent line shape simulation using two different ^{6}Li resonances at 0 ppm (blue dashed line) and –0.4 ppm (red dashed line) corresponding to A-site (LiO_4 or LiO_5) and B-site (LiO_6) local environments, respectively. All spectra were obtained at a MAS rate of ν_r = 10 kHz unless noted.

Computationally-assisted spectral assignment using the DFT–GIPAW method is a common approach when studying new materials with solid state NMR.[21,22] This approach has successfully derived local structures on a variety of materials with various nuclei,[23–28] including ^{6}Li and ^{17}O.

The three most stable configurations of $La_3Li_3W_2O_{12}$ **C1**, **C2** and **C3**[1] (Figure 4.2c-e) were used to predict the ^{6}Li NMR parameters using the GIPAW approach. The ^{6}Li isotropic shielding values σ_{iso} were converted using the

formula $\delta_{iso} = 86.89 - 0.96\sigma_{iso}$, obtained by linear fitting of calculated σ_{iso} values and the experimental isotropic shifts δ_{iso} of Li_2O, LiOH and Li_2CO_3 with an RMS error of 0.24, which is smaller than the change in Li shift in relation to Li-O coordination number,[18–20] highlighting high accuracy. Li^+ ions at the A-sites in these optimised structures have calculated isotropic chemical shielding values, σ_{iso}, of 91.0 ± 0.1 ppm (and calculated isotropic chemical shifts δ_{iso} = –0.6 ± 0.1 ppm) and those at the B-sites of 91.5 ± 0.1 ppm (and δ_{iso} = –1.0 ± 0.2 ppm, Figure 4.4). Although the exact shift is not equal to experimental NMR shifts, this is often observed in literature[23–28] and reported as error when calculating reference data. Therefore the difference between the shifts are important, which are consistent between calculated and experimental values (0.0 and –0.4 ppm).

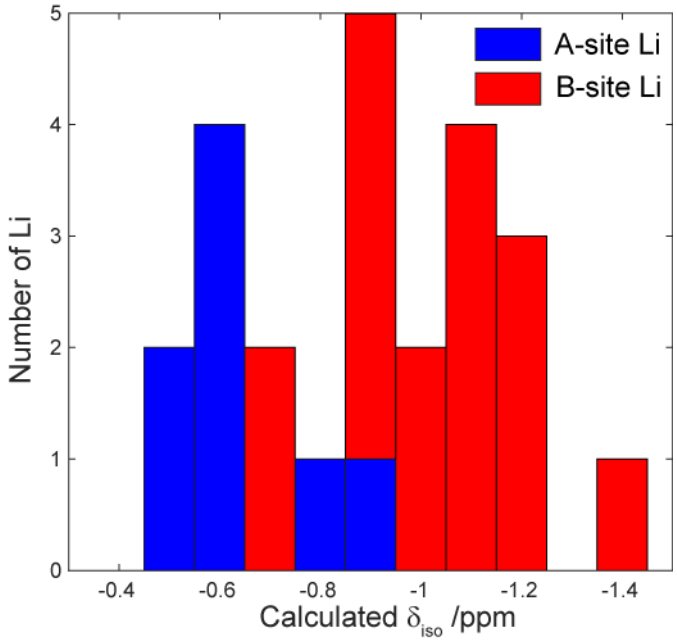

Figure 4.4. Calculated isotropic chemical shifts, δ_{iso}, for Li^+ ions in structures **C1**, **C2** and **C3** (Figure 4.2c-e).

4.2.1.2 ^{17}O NMR Spectroscopy

The ^{17}O Hahn echo spectra obtained for $La_3Li_3W_2{}^{17}O_{12}$ at 9.4 and 20 T show a pattern consisting of multiple overlapping peaks spanning 300 to 500 ppm (Figure 4.5a). Both spectra have similar line widths and no further line narrowing is seen at high field, as expected for ionic solids.[30] No further spectral resolution is obtained in the 2D 3QMAS NMR spectrum obtained at 9.4 T (Figure 4.5b) which shows signal along the isotropic diagonal and is indicative of a large distribution of chemical shifts, associated with structural disorder seen in the crystal structure (Figure 4.2a).

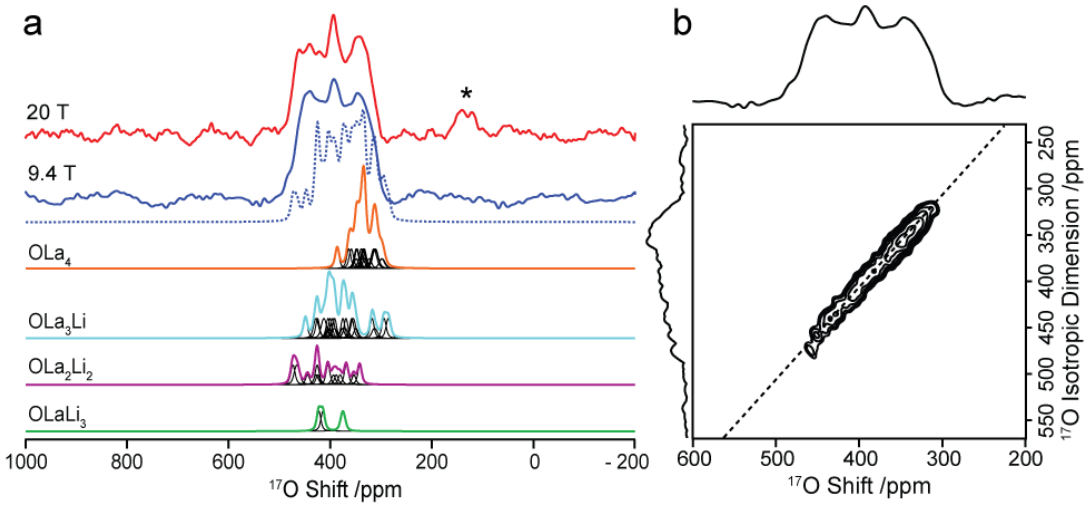

Figure 4.5. (a) ^{17}O Hahn echo NMR spectra of $La_3Li_3W_2{}^{17}O_{12}$ recorded at 9.4 T under MAS at 13 kHz (blue) and at 20 T under MAS at 20 kHz (red). The blue dotted line is the sum of the simulated spectra of the calculated GIPAW[21,22] ^{17}O shifts for the 96 oxygen atoms of $La_3Li_3W_2O_{12}$ within the three lowest energy structures **C1**, **C2** and **C3** ($OLaLi_3$, OLa_2Li_2, OLa_3Li and OLa_4 oxygen environments are given in green, purple, cyan and orange, respectively) simulated at 9.4 T. Black lines denote the simulated peaks of each individual atom. The calculated ^{17}O shifts appear to be weakly correlated

with the number of La^{3+} ions around a single O^{2-} ion (Figure 4.6). Asterisks (*) denote spinning sidebands. (b) ^{17}O 2D z-filtered 3QMAS spectrum of $La_3Li_3W_2{}^{17}O_{12}$ recorded at 9.4 T and under MAS at 13 kHz. The diagonal dotted line represents the isotropic correlation line. Left: isotropic projection of the 2D 3QMAS data. Top: ^{17}O Hahn echo NMR spectra of $La_3Li_3W_2{}^{17}O_{12}$.

The NMR parameters of the O atoms in the lowest energy DFT structures lowest **C1**, **C2** and **C3** (Figure 4.2c-e) were calculated using the GIPAW approach.[21,22] GIPAW calculations were used to determine the expected experimental shifts arising from the various local oxygen environments OLi_3La, OLa_2Li_2, OLa_3Li and OLa_4 in $La_3Li_3W_2O_{12}$. ^{17}O shifts δ were calculated using equations (2.17) and (2.18), where $\delta_{iso,q}$ is < 11.6 ppm and < 2.6 ppm at 9.4 and 20 T, respectively, small values as expected for ionic solids.[30]

Calculated ^{17}O shifts δ are distributed over the 300 – 480 ppm range (Figure 4.5a) and agree well with the experiment shifts observed in $La_3Li_3W_2{}^{17}O_{12}$. There is a weak correlation between the predicted shifts and the different number of A-site Li^+ ions coordinated to a single O^{2-} ion, the higher shift obtained corresponding to the larger number of coordinated Li^+ ions (Figure 4.6). This trend is expected due to the smaller chemical shieldings (and hence larger shifts) created around oxygens by the smaller four-coordinated Li^+ than La^{3+} (ionic radii of 0.76 and 1.03 Å, respectively).[31]

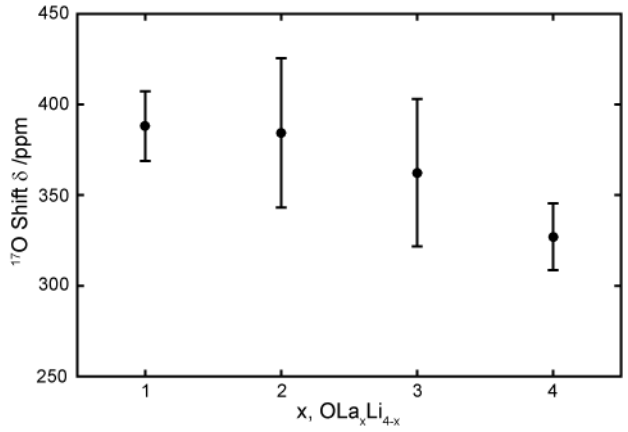

Figure 4.6. Average ^{17}O shift δ obtained from GIPAW[21,22] calculations of structures **C1**, **C2** and **C3** against number of La^{3+} ions *x* surrounding a single O^{2-} anion.[1] Error bars represent the standard deviation of the range of shifts.

4.2.1.3 ^{7}Li–^{17}O Correlation NMR

To further investigate the local environment surrounding Li, ^{7}Li–^{17}O dipolar-based HMQC experiments were conducted at 20 T (Figure 4.7). A clear correlation between B-site ^{7}Li and ^{17}O is observed, signifying close proximity of the two nuclei, as expected for a LiO_6 octahedra. For A-site Li, correlation is observed with downfield ^{17}O shifts with lower intensity cross peaks, as expected for a Li site with a lower coordination number. Two explanations can be made in relation to the low intensity of this peak: 1. the A-site Li is mobile at room temperature (see later sections), which would average out the heteronuclear dipole-dipole interaction between the two nuclei; 2. as the oxygen enrichment level is unknown and is possibly low, which would lower the number of ^{7}Li–^{17}O interactions, reducing the intensity of the cross peaks. If the enrichment level is high, one can assume that the peak intensity increase.

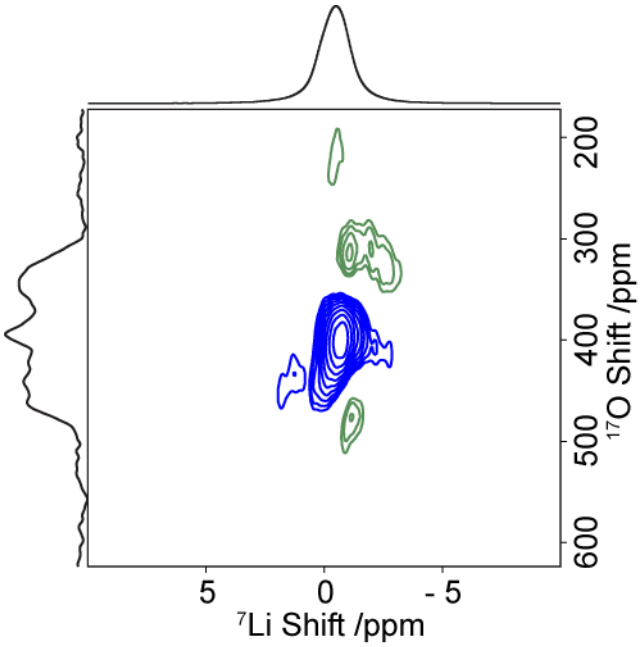

Figure 4.7. ^{7}Li–^{17}O HMQC NMR spectra of $La_3Li_3W_2{}^{17}O_{12}$ recorded at 20 T at a MAS frequency of 13 kHz. Blue and green contours denote positive and negative contours, respectively. Top: ^{7}Li MAS NMR spectra of $La_3Li_3W_2{}^{17}O_{12}$ at MAS of 13 kHz. Left: ^{17}O Hahn echo NMR spectra of $La_3Li_3W_2{}^{17}O_{12}$ at MAS of 20 kHz.

4.2.2 Variable Temperature NMR

4.2.2.1 Temperature Stability of $La_3Li_3W_2O_{12}$

Prior to investigating the Li^+ dynamics of $La_3Li_3W_2O_{12}$, temperature stability test of the sample was performed on a BN pellet under high temperature in N_2 atmosphere. Extra reflections were observed only when $La_3Li_3W_2O_{12}$ was heated above 1000 K, denoting decomposition of the material at these conditions, giving the upper limit of high temperature experiments. These extra reflections were assigned by peak matching using the appropriate atoms present during experiment in X'Pert HighScore Plus and are assigned to $LaWO_{0.6}N_{2.4}$, $La_4B_2WO_{12}$, Li_4WO_5, $La_{0.14}WO_3$. The broad

background was assigned to the BN from the pellet.

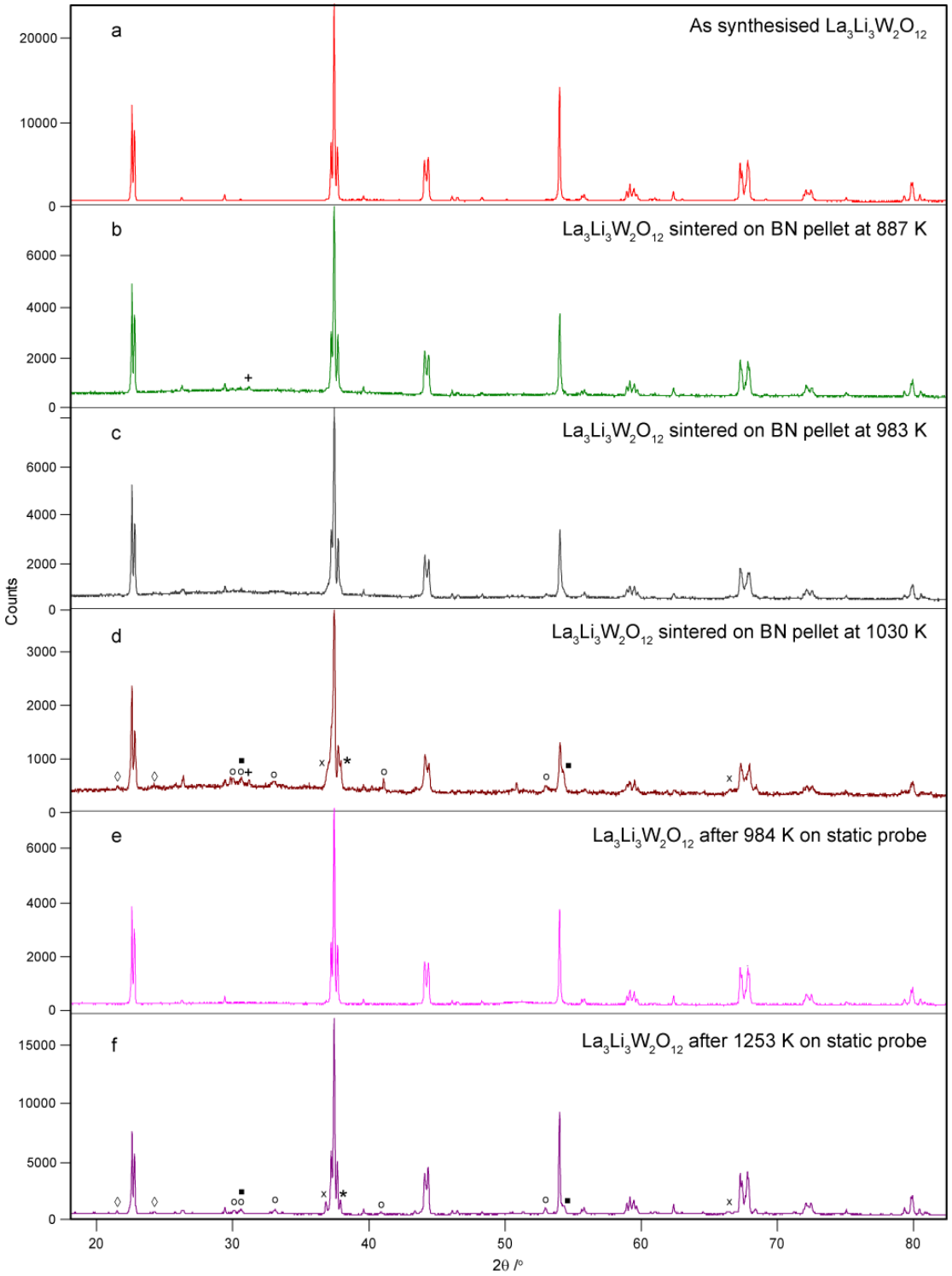

Figure 4.8. Temperature stability test of $La_3Li_3W_2O_{12}$ under reducing atmosphere and in contact with BN. PXRD patterns of (a) as synthesised $La_3Li_3W_2O_{12}$, (b–d) after sintering on a BN pellet under 10 mL/min N_2 flow, and after high temperature NMR with the static laser heated probe up to (e) 984 K

and (f) 1253 K (under reduced N_2/Ar atmosphere). Impurity phases are denoted as $LaWO_{0.6}N_{2.4}$ (×), $La_4B_2WO_{12}$ (o), Li_4WO_5 (◊), $La_{0.14}WO_3$ (▪), BN (+). Unidentified phases are marked with asterisks (*).

4.2.2.2 ^{6}Li Exchange Spectroscopy

AIMD measurements identified migration of B-site Li migrated to the A-site, signifying an extra Li^+ diffusion pathway (Figure 4.2h).[1] Exchange spectroscopy (EXSY) NMR has been used to study Li^+ mobility between two different Li^+ sites[19,32–34] (see Chapter 2 for theory) and was therefore selected to experimentally determine migration between A-site Li and B-site Li.

^{6}Li EXSY NMR on $La_3{}^6Li_3W_2O_{12}$ obtained at 9.4 T at varying conditions are shown in Figure 4.9a-c. NMR spectra are extracted from the peak representative of A-site Li (0 ppm, dotted line) as the broad B-site Li peak overlaps with the A-site spectra (Figure 4.3), complicating the extraction of cross peaks. At room temperature at MAS of 10 kHz (Figure 4.9d), an increase in intensity at -0.5 ppm is observed with increase in mixing time. This resonance is assigned to B-site Li and highlights spatial interaction with A-site Li. EXSY at higher temperature (Figure 4.9e) gives higher resolution, and we also see an increase in the peak representative of B-site Li with mixing time, consistent with room temperature data. Similar observations are made with EXSY measured at higher MAS (Figure 4.9f). The distance between the nearest A-site Li and B-site Li is 3.4 Å, resulting in a very small ^{6}Li–^{6}Li dipole-dipole constant of 66 Hz which is averaged out by MAS, and therefore suggests that the cross peak presence is not a result of spin diffusion, but rather site migration of A-site Li and B-site Li, showing that migration between

sites is also a probable path. The rate and activation barrier of Li site exchange may be determined with further experiments by conducting experiments with a longer mixing times (Equation 2.28).

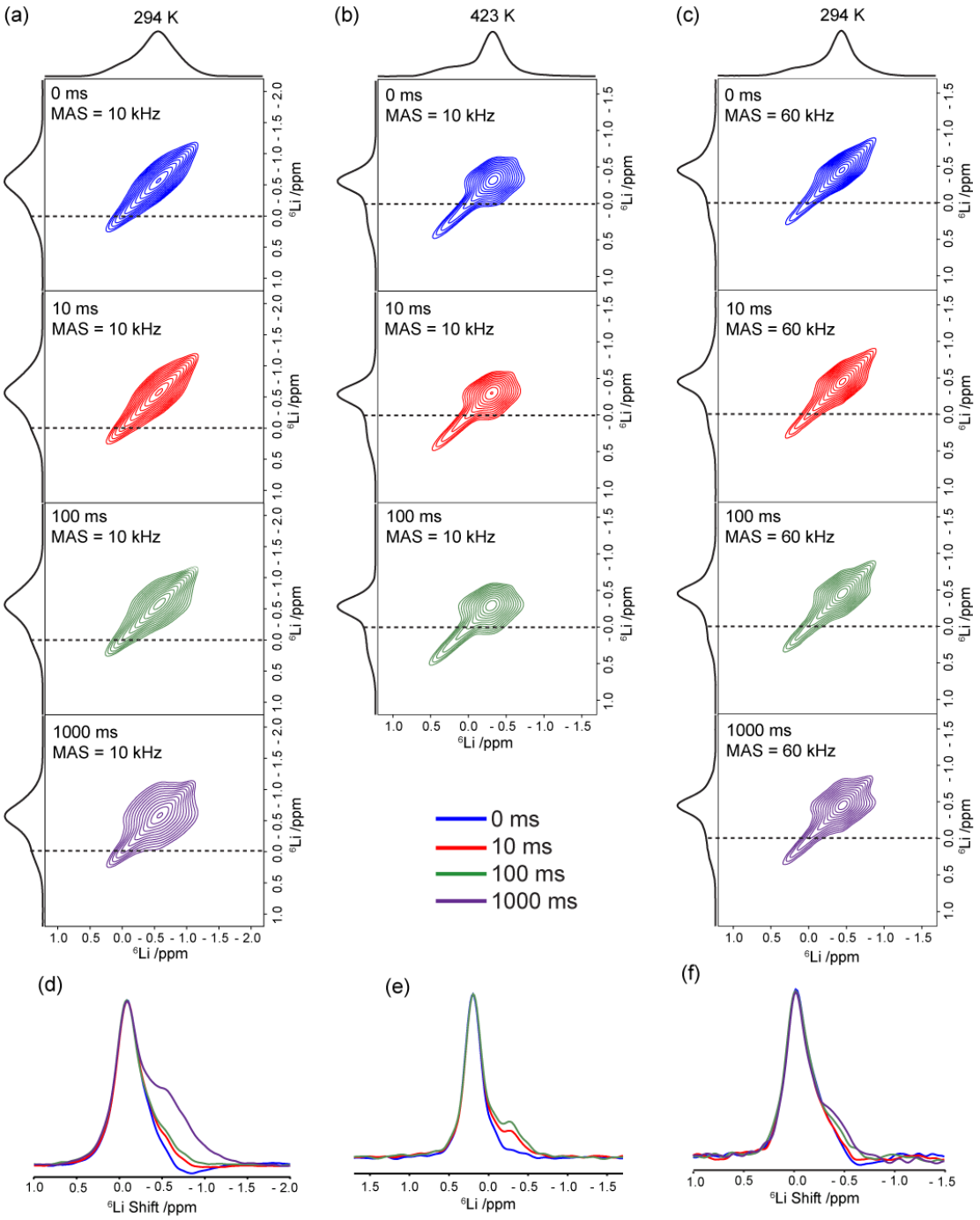

Figure 4.9. ^{6}Li EXSY NMR on $La_3{}^{6}Li_3W_2O_{12}$ obtained at 9.4 T at (a) MAS = 10 kHz at room temperature, (b) MAS = 10 kHz at 423 K and (c) MAS = 60 kHz at room temperature. Top and left: ^{6}Li MAS NMR spectra at the respective

conditions. (d, e, f) Extracted horizontal slice along the A-site Li on the F_1 axis at different mixing times for the 2D ESXY data reported in (a), (b) and (c), respectively. The spectra are normalised to the largest peak.

4.2.2.3 **Li^+ ion mobility: ^7Li line shape analysis**

Information on the Li^+ ion dynamics was initially obtained from motional narrowing of the static ^6Li and ^7Li NMR spectra as a function of temperature. The variable temperature ^7Li NMR spectra of $La_3Li_3W_2O_{12}$ and ^6Li NMR spectra of fully ^6Li enriched $La_3Li_3W_2O_{12}$ ($La_3{}^6Li_3W_2O_{12}$) obtained at 9.4 T are shown in Figure 4.10. Below room temperature, the ^7Li static NMR spectra show the anticipated line shape expected for a spin 3/2 nucleus with a dipolar broadened central line (full width at half maximum of ~4 kHz) at around 0 ppm corresponding to the 1/2 ↔ −1/2 central transition, and a very broad resonance spanning ~300 ppm (~50 kHz) corresponding to the 3/2 ↔ 1/2 and −1/2 ↔ −3/2 satellite transitions. The broadening of the central transition is due to the strong ^7Li–^7Li homonuclear dipolar interaction and is averaged out as the temperature is increased due to greater Li^+ ion mobility (Figure 4.10c), yielding motional narrowing of NMR line widths. Similarly, the ^6Li static NMR lines of $La_3{}^6Li_3W_2O_{12}$ are slightly broadened (~1.4 kHz) below room temperature and narrow with increasing temperature to ~0.7 kHz at ~600 K and ~0.5 kHz above ~900 K. The onset of motional narrowing occurs at similar temperatures of ~300 K for both ^6Li and ^7Li, which is expected as the the Larmor frequencies of the isotopes are on the same order of magnitude. At the inflexion point of the temperature dependent line narrowing experiment, the Li^+ jump rates τ^{-1} are estimated from the NMR linewidth in the low temperature rigid-lattice

regime $\Delta\omega_{\text{rigid lattice}}$, and yield values of ~9 × 10^3 s^{-1} and ~3 × 10^4 s^{-1} at 400 K and 420 K from ^{6}Li and ^{7}Li data, respectively.

In the fast motional regime above 420 K, the static ^{7}Li NMR spectra show motionally narrowed NMR lines and the typical broad powder pattern line shape characteristics of a spin 3/2 nucleus with the clear discontinuities associated with the satellite transitions. At 720 K, these singularities are observed at ~ −100 and 100 ppm (Figure 4.10a) from which a quadrupolar coupling constant C_Q of 30 kHz can be estimated. As the temperature is increased to 984 K, the broad static pattern gradually narrows through a continuous averaging of the electric quadrupolar interactions down to ~16 kHz by Li^+ ion motion. It is potentially expected that at higher temperature the satellite transitions would completely narrow and vanish due to increasing Li^+ ion mobility. However, this regime is not obtained here due to the decomposition of $La_3Li_3W_2O_{12}$, or its reaction with the BN crucible, above 1000 K under the reducing N_2/Ar atmosphere of the high temperature laser heated NMR probe used (Figure 4.8). Another possible explanation could be deduced from the crystal structure $La_3Li_3W_2O_{12}$. The A-sites are fully occupied by La and Li with no obvious vacancies (Figure 4.2a). DFT calculations suggests Li moves between neighbouring A-sites also occupied by Li,[1] which would give anisotropic Li diffusion in this sample. This would not allow full averaging out of the satellite transitions, even at high temperatures.

The average C_Q values calculated by DFT–GIPAW calculations are found to be 161(23) and 117(52) kHz for the A and B-sites Li, respectively, significantly larger than the values observed at high temperature experimentally. The simulation for the spectrum measured at 166 K where no

Li is mobile, estimated the C_Q to a value of ~45 kHz, significantly lower than the calculated values. The difference is possibly caused by the mobility of A-site Li within the A-site seen in molecular dynamics calculations in $La_3Li_3W_2O_{12}$, reducing the size of the local electric field gradient around Li^+ ions.

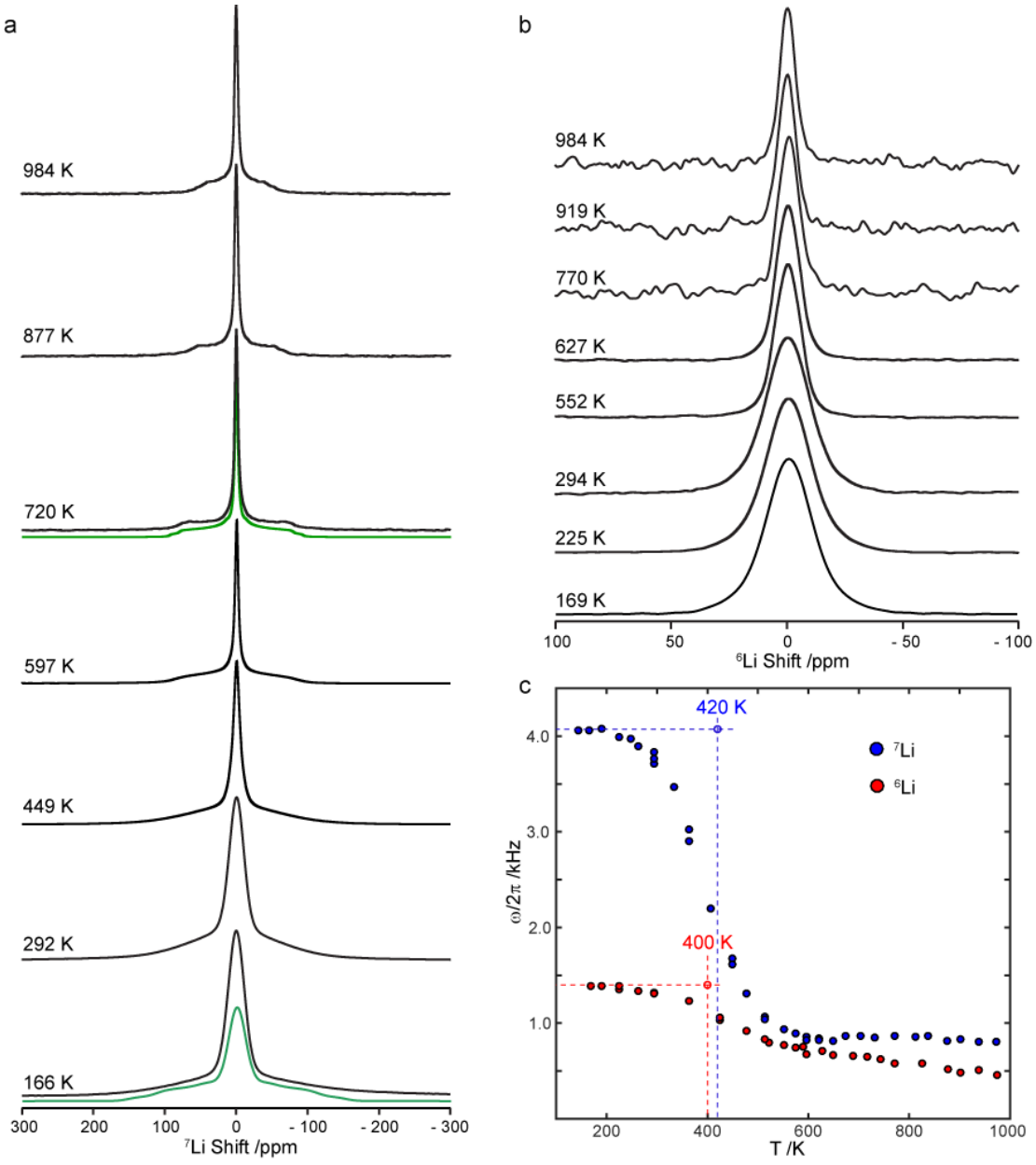

Figure 4.10. The Li^+ dynamics obtained from NMR motional narrowing. (a) ^7Li static NMR spectra of $La_3Li_3W_2O_{12}$ and (b) ^6Li static NMR spectra of $La_3{}^6Li_3W_2O_{12}$ as a function of temperature. The green spectra in (a) correspond to line shape simulations. (c) Temperature dependence of the ^6Li

(red) and ^{7}Li (blue) NMR line widths of $La_3Li_3W_2O_{12}$. The vertical and horizontal dashed lines give the temperatures corresponding to the inflexion point of the ^{6,7}Li line narrowing experiments and the rigid-lattice linewidth $\Delta\omega_{\text{rigid lattice}}$ used to determine the Li jump rates τ^{-1} ($\tau^{-1} \approx \Delta\omega_{\text{rigid lattice}}$), respectively, and are guides to the eyes.

4.2.2.4 **Li$^+$ ion mobility: ^{6,7}Li spin lattice relaxation rates**

Figure 4.11 shows the temperature dependence of the ^{6}Li and ^{7}Li spin-lattice relaxation rates in the laboratory and rotating frames, T_1^{-1} and $T_{1\rho}^{-1}$, providing Li$^+$ ion dynamics with frequencies on the order of the Larmor (ν_0 = 59 and 156 MHz for ^{6}Li and ^{7}Li) and spin-lock frequencies (ν_1 = 8 and 14 kHz), respectively, and resulting from fluctuations of the local magnetic dipolar or electrical quadrupolar interactions induced by Li$^+$ ion motion.

The dominant relaxation mechanism can be determined by calculating the ratio of T_1 values between ^{7}Li and ^{6}Li (see Chapter 2). In the case of $La_3Li_3W_2O_{12}$, the ratio $T_1(^7\text{Li})/T_1(^6\text{Li})$ is approximately 0.7 at room temperature, signifying that dipolar interaction is the dominant relaxation mechanism which allows one to determine Li$^+$ mobility using the Bloembergen-Purcell-Pound (BPP) theory of relaxation.[45]

At temperature below 250 K, the T_1^{-1} and $T_{1\rho}^{-1}$ values are relatively constant, showing little Li$^+$ ion motion. As the temperature is increased to 260 K, the T_1^{-1} and $T_{1\rho}^{-1}$ rates measured for both ^{6}Li and ^{7}Li become longer and are indicative of a slow motional regime (where $2\pi\nu_0\tau_c$ and $2\pi\nu_1\tau_c >> 1$ with τ_c the correlation time of the motion). Here, both T_1^{-1} and $T_{1\rho}^{-1}$ rates do not characterise Li$^+$ ion translational diffusion[36] but probe local processes such as

hopping between local energy minima that contribute to unsuccessful jumps between cages. Activation energies E_a on the order of 0.09–0.19(2) eV are extracted and are similar to those seen in this regime in other Li^+ ion conducting oxides such as $La_{2/3-x}Li_{3x}TiO_3$ ($0.08 < x < 0.167$)[37–39] and cubic $Li_7La_3Zr_2O_{12}$.[40]

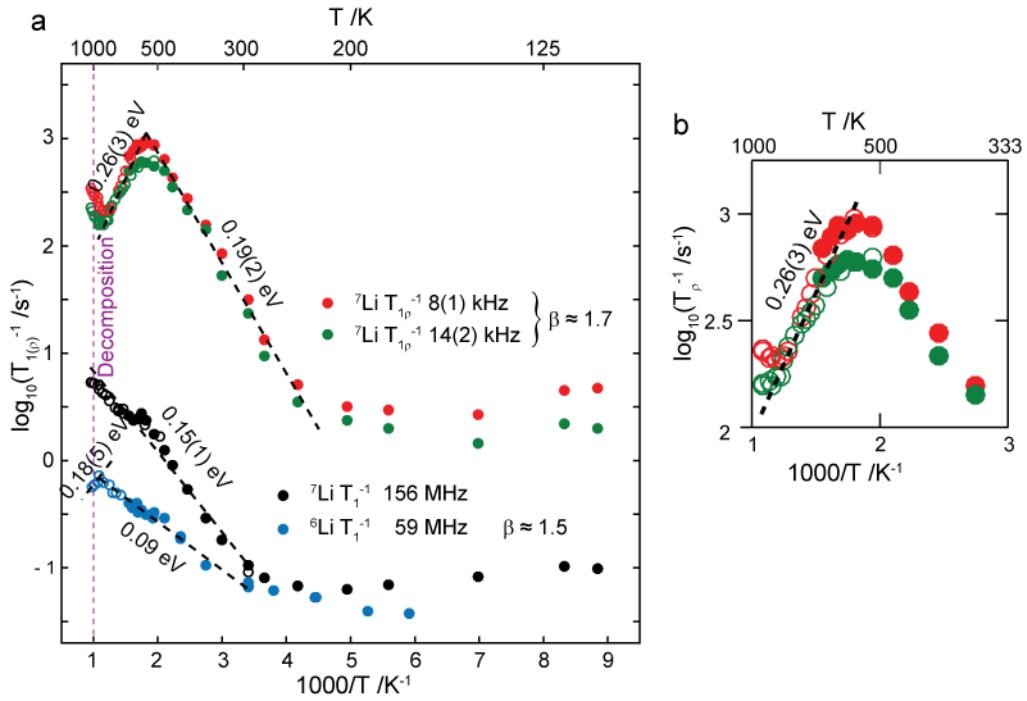

Figure 4.11. The Li^+ ion dynamics obtained from NMR relaxometry. (a) Arrhenius plot of the spin-lattice relaxation rates T_1^{-1} obtained at $\nu_0(^6Li)$ = 59 MHz (blue) on $La_3{}^6Li_3W_2O_{12}$ and $\nu_0(^7Li)$ = 156 MHz (black), and the spin-lattice relaxation rates in the rotating frame $T_{1\rho}^{-1}$ obtained at $\nu_1(^7Li)$ = 8 kHz (red) and 14 kHz (green) on $La_3Li_3W_2O_{12}$. Filled and empty black circles refer to data obtained with the MAS probes and the laser heated static probe, respectively. The slight anomaly seen at ~600 K for ^7Li T_1^{-1} data perhaps results from the change in NMR probe used to perform the experiment. Dashed lines represent the range where the activation energies E_a and the deviation from BPP theory defined by β (see text) are determined. (b) Zoomed in view around the $T_{1\rho}^{-1}$

maxima and the fast motion regime to highlight frequency independence of $T_{1\rho}^{-1}$ values.

As the temperature is increased further, $T_{1\rho}^{-1}$ maxima are observed at around 550 K and the Li^+ ion jump rates τ^{-1} are on the order of the spin-lock frequency ν_1 ($2\pi\nu_1\tau \approx 0.5$)[41] yielding values of 1 x 10^5 and 1.8 x 10^5 s^{-1} at 552 and 574 K. At temperatures above these maxima, the T_1^{-1} and $T_{1\rho}^{-1}$ rates decrease (*i.e.,* the material enters the fast motional regime, $2\pi\nu_0\tau_c$ and $2\pi\nu_1\tau_c$ << 1) and the jump rates τ^{-1} relate to Li^+ translational diffusion.[42,43] An activation energy of 0.26 ± 0.10 eV is determined from the ^7Li $T_{1\rho}^{-1}$ relaxation rates in this regime. The frequency dependence of T_1^{-1} and $T_{1\rho}^{-1}$ rates in the fast motional regime ($2\pi\nu_0\tau$ and $2\pi\nu_1\tau$ << 1) is well-known to relate to the dimensionality of the diffusion processes.[42,44] Figure 4.11 shows that the ^7Li $T_{1\rho}^{-1}$ rates obtained over the 600 – 800 K temperature range and probed at two different spin lock frequencies (ν_1 = 8 kHz and 14 kHz) are independent of frequency, characteristic of 3D diffusion of Li^+ ions in $La_3Li_3W_2O_{12}$ (see Chapter 2).

The asymmetric behaviour of the temperature dependence of the $T_{1\rho}^{-1}$ rates on either side of the maxima has been well documented in the literature for fast ion conductors and disordered materials, and arises from a combination of structural disorder and Coulomb interactions of mobile ions.[19,42] This yields a deviation from the BPP theory of relaxation[45] (which predicts symmetric peaks and a quadratic frequency dependence of the relaxation rates $T_{1\rho}^{-1} \propto \nu^{-2}$) giving in the slow motional regime ($2\pi\nu_1\tau$ >> 1) a frequency

dependence of the form $T_{1\rho}^{-1} \propto \nu^{-\beta}$, where the model parameter β ranges between 1 and 2. Our data in the two low temperature flanks of the $T_{1\rho}^{-1}$ rates are indeed frequency-dependent and fit to an exponent β = 1.7 for ^{7}Li $T_{1\rho}^{-1}$ (using the equation $E_{a,low} = (\beta-1)E_{a,high}$[42] where $E_{a,low}$ = 0.19 eV and $E_{a,high}$ = 0.26 eV are the activation energies on the low and high temperature flanks, respectively). The higher activation energy observed at high temperature accounts for cooperative effects such as long range Coulombic interactions between charge carriers or structural disorder that produce multiple or correlated hops over longer distances than probed in the lower temperature regime, and corresponds to translational diffusion of Li^{+} ions.[41]

The jump rates τ^{-1} extracted from the NMR relaxometry data (that is the two maxima of the ^{7}Li $T_{1\rho}^{-1}$ data, Figure 4.11) and the line narrowing experiments (Figure 4.10c) are plotted against reciprocal temperature (Figure 4.12). The fit to the data using an Arrhenius equation of the form $\tau^{-1} = \tau_0^{-1} \exp(E_a/RT)$ is reasonably good and yields an activation energy E_a of 0.29 ± 0.17 eV and a prefactor (attempt frequency) τ_0^{-1} of ~6×10^7 s^{-1}. The activation energy determined here is identical to the value seen in the high temperature flank of the ^{7}Li spin-lattice relaxation rate plot (Figure 4.11) within experimental error, which suggests that we probe the same diffusive process in both line narrowing and relaxometry experiments.

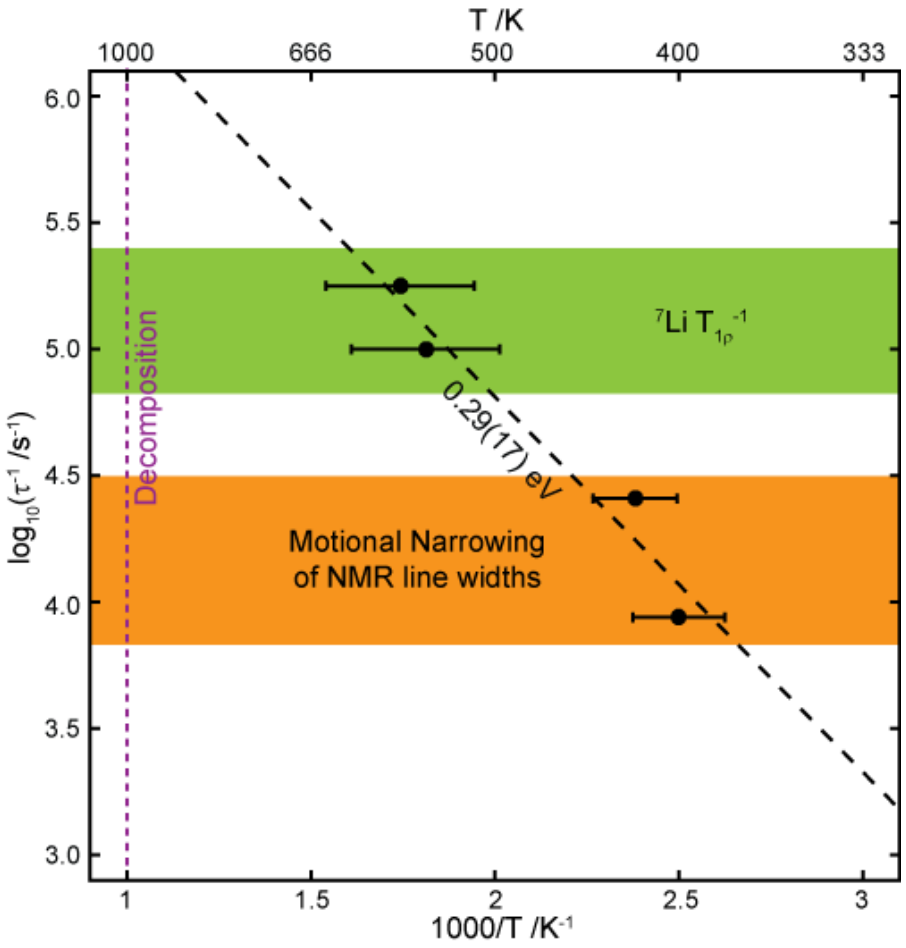

Figure 4.12. Arrhenius plot of Li jump rates τ^{-1} extracted from motional narrowing of NMR line width (Figure 4.10) and the NMR relaxometry data. Horizontal error bars represent the estimated errors of temperature gradient and peak position of $T_{1\rho}^{-1}$ maximum. Vertical error bars are within the size of the symbols. Note that at around 800 K, $T_{1\rho}^{-1}$ minima are seen and may correspond to a different Li^+ dynamics mechanism, which is not quantitatively accessible due to sample decomposition at the higher temperatures where data would be needed to fully probe these processes (see Figure 4.8).

NMR conductivity σ_{NMR} can be calculated from this NMR-derived Li^+ ion jump rate τ^{-1} (Figure 4.12) by combining the Nernst-Einstein and the Einstein-

Smoluchowski equations (Equation 2.32). The ratio of the correlation factor and Haven ratio f/H_R is set to 1 for uncorrelated motion, N_{CC} is the number of charge carriers (assumed as 1 A-site Li) per unit cell volume (245 $Å^3$), q is the ionic charge of Li^+, a is the average jump distance (taken as 4 ± 0.2 Å for A-site Li–Li distance) and n is the dimension of diffusion; and yields values in the range of 5.8 x 10^{-5} – 2.2 x 10^{-4} S/cm between 400 and 574 K (Figure 4.13).

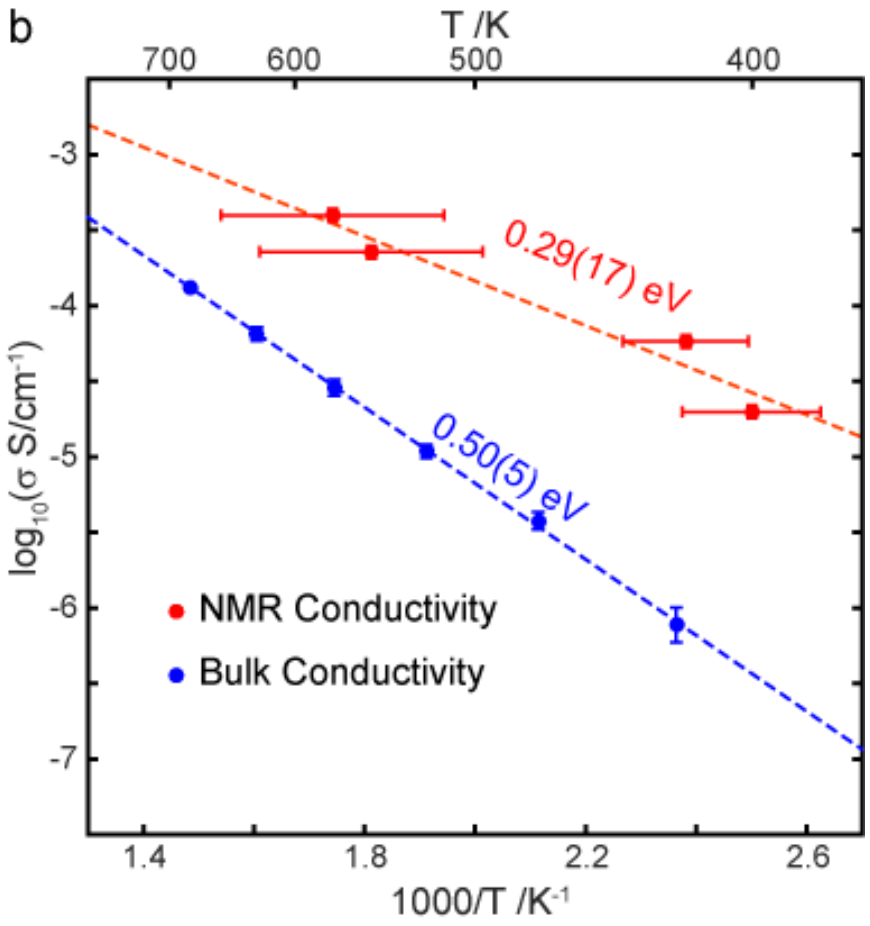

Figure 4.13. Bulk conductivities σ of $La_3Li_3W_2O_{12}$ *vs.* temperature obtained from the AC impedance data, and extracted from the NMR Li^+ jump rates τ^{-1} obtained from ^7Li relaxation rates $T_{1\rho}^{-1}$ and motional narrowing using the Nernst-Einstein-Smoluchowski equations. The horizontal error bar on the NMR conductivity is an estimation of the temperature gradient on NMR probe and the peak position for $T_{1\rho}^{-1}$ maximum.

4.3 Discussion

The activation energy extracted from the high temperature flank of the $T_{1\rho}^{-1}$ relaxation data (0.26 ± 0.10 eV) and from the jump rates obtained the ^{6,7}Li line narrowing experiments and the $T_{1\rho}^{-1}$ maxima (0.29 ± 0.17 eV) are identical within experimental error, and reflect the barrier to the same 3D translational diffusion process. These values are similar to the maximum energy barrier calculated for the A-site to neighbouring A-site pathway (Figure 4.2g) and suggest that we probe this diffusive process. The activation energy obtained on the high temperature flank (0.26 eV) of the $T_{1\rho}^{-1}$ data is similar to those of $La_{2/3-x}Li_{3x}TiO_3$ (0.20 eV for x = 0.11,[37] 0.26 eV for x = 0.08,[38] and 0.26 eV for x = 0.167)[39] and doped $Li_7La_3Zr_2O_{12}$ (0.34 eV)[40] which suggests that barrier to A-site to A-site Li^+ ion diffusion in $La_3Li_3W_2O_{12}$ probed by NMR is comparable to the best oxide Li^+ ion conductors reported, despite the considerable structural and Li^+ diffusive pathway differences from the perovskite $La_{2/3-x}Li_{3x}TiO_3$ family.[37,46,47] In this phase, the relaxometry plot for Li^+ ions in $La_{2/3-x}Li_{3x}TiO_3$ (x = 0.11) shows two motional regimes – at low temperatures (T < 200 K) a 2D diffusion process is observed, where only the bottlenecks between A-sites on the same La^{3+} poor layers are large enough to accommodate Li^+ ion transport in the material, and a 3D diffusion process above 200 K, where thermal agitation opens up the bottleneck between La^{3+} rich and La^{3+} poor layers allowing Li^+ to hop between the two layers.[37,46,47]

The prefactor τ_0^{-1} of ~6×10^7 s^{-1} obtained in the Arrhenius fit is lower than seen in $La_{2/3-x}Li_{3x}TiO_3$ (x = 0.08, $\tau_0^{-1} = 4.6 \times 10^{11}$ s^{-1}),[38] and some other fast Li conductors[48,49,50] but comparable to $Li_2Ti_3O_7$ reported by Huberman and Boyce

(τ_0^{-1} = ~4 x 10^7 s^{-1}),[51] though on a more recent study on $Li_2Ti_3O_7$ by Volgmann *et al.*,[34] a prefactor τ_0^{-1} of ~6 × 10^{13} s^{-1} was observed. Attempt frequencies in Li^+ ion conductors are usually found to be lower than those for crystal lattices (~10^{13} s^{-1}), and are often attributed to the large distribution of the charge carrier sites through disorder, resulting in a shallow potential wells with low activation barriers, resulting in a decrease in attempt frequency.[53] In the case of $La_3Li_3W_2O_{12}$, the phenomenon where the attempt frequency is low by multiple orders of magnitudes when compared to other Li^+ ion conductors could be explained with the aid of the computational approach. DFT calculations identified three possible Li positions in the A-site with very small activation barriers of 0.08 eV between each site.[1] *Ab initio* molecular dynamics calculations at 298 K also show that A-site Li accesses a large region of space within the site. The combination of potential wells with low energy barriers and the large number of possible positions available for A-site Li to migrate would significantly decrease the attempt frequency.

The activation energy for Li^+ site-to-site motion obtained from NMR conductivity (0.29 ± 0.17 eV) is smaller than the value determined through impedance measurements (0.50 ± 0.05 eV), such a difference is not uncommon in the literature of fast ion conductors,[28,48,54–56] including $La_{2/3-x}Li_{3x}TiO_3$,[38,57] and has been discussed extensively before.[58] The activation energy obtained from the ^{6,7}Li NMR dataset can be assigned to migration between A-sites, while that obtained from conductivity is often larger as it may contain additional contributions such as defect formation, and defect association that are involved in longer-range transport of Li between multiple cages. Defect creation energies are in the range 0.4–0.6 eV in $La_3Li_3W_2O_{12}$

from the small supercell calculations presented in the Appendix. The NMR conductivity is higher than the bulk impedance conductivity (by up to two orders of magnitude at low temperature (Figure 4.13). This discrepancy is observed in other systems,[28,32,38,50,58] as unsuccessful Li^+ ion jumps (that is a moving ion returning to its original site rather than hopping further to the next site) contribute to the motional narrowing of the NMR spectra and the relaxation rates without producing longer range Li^+ ion transport probed by impedance spectroscopy.[58,59] For example, NMR conductivity is an order of magnitude higher than values obtained in impedance spectroscopy for $La_{2/3-x}Li_{3x}TiO_3$ (x = 0.08) [38] and Li_2ZrO_3.[32]

4.4 Conclusions and Future Prospects

The identification of two distinct Li sites on the A-site and B-site in $La_3Li_3W_2O_{12}$ gives it a unique crystal structure and Li^+ dynamics compared to other perovskite Li^+ ion conductors (Chapter 3). ^{6}Li MAS NMR identified the two distinct Li sites with ratios in agreement with both diffraction and computational results. ^{7}Li-^{17}O HMQC experiments showed the close proximity of downfield ^{17}O resonances and A-site ^{7}Li, complemented by computational calculations of NMR parameters. The A-site to B-site Li migration observed by *ab initio* molecular dynamics was seen by EXSY NMR on $La_3{}^6Li_3W_2O_{12}$ with cross peaks present between the two sites. The possibility of spin diffusion was removed under the experimental conditions and highlighted the exchange of Li^+ between the two sites – this indicates that $La_3Li_3W_2O_{12}$ is the first perovskite material where Li migrates between the two different crystallographic sites. The experimentally identified the barrier of A-site to A-

site Li^+ diffusion by $^{6,7}Li$ NMR relaxometry (0.29 ± 0.17 eV) is comparable to those seen in the best Li conducting oxides also studied of 0.2~0.3 eV, highlighting its potential as a possible candidate for use as a Li ion conductor.

The large discrepancy in activation barriers between NMR and impedance spectroscopy is attributed to the requirement of defect formation and low percolation of the Li^+ ion within the lattice through the lack of an obvious Li^+ diffusion pathway. In attempts to increase the conductivity of $La_3Li_3W_2O_{12}$, approaches such as introducing vacancies could be taken, though one should also carefully consider decreasing the amount of higher charged cations, resulting in increased Li ordering and give a clearer long range Li diffusion pathway, both which in turn would increase overall conductivity. Another possible approach would be to increase the rate of A-site to B-site Li migration, in which case interactions such as repulsion between Li^+ and the framework O^{2-} ions must be considered. Controlling the appropriate defect chemistry for either or both approaches would allow for emergence of materials with multiple Li^+ diffusion pathways and would bring about new methods and possibilities when designing new Li^+ ion conductors.

4.5 References

1 A. B. Santibáñez-Mendieta, C. Didier, K. K. Inglis, A. J. Corkett, M. J. Pitcher, M. Zanella, J. F. Shin, L. M. Daniels, A. Rakhmatullin, M. Li, M. S. Dyer, J. B. Claridge, F. Blanc and M. J. Rosseinsky, *Chem. Mater.*, 2016, **28**, 7833–7851.

2 S. Vasala and M. Karppinen, *Prog. Solid State Chem.*, 2015, **43**, 1–36.

3 Y. Hikichi and S. Suzuki, *J. Am. Ceram. Soc.*, 1987, **70**, C-99-C–100.

4 G. Demazeau, E. Oh-Kim, J. Choy and P. Hagenmuller, *Mater. Res. Bull.*, 1987, **22**, 735–740.

5 K. Hayashi, H. Noguchi and M. Ishii, *Mater. Res. Bull.*, 1986, **21**, 401–406.

6 M. L. López, M. L. Veiga, J. Rodríguez-Carvajal, F. Fernández, A. Jerez and C. Pico, *Mater. Res. Bull.*, 1992, **27**, 647–654.

7 H. Wu and P. K. Davies, *J. Solid State Chem.*, 2004, **177**, 3469–3478.

8 H. Wu and P. K. Davies, *J. Solid State Chem.*, 2004, **177**, 4305–4315.

9 L. Frydman and J. S. Harwood, *J. Am. Chem. Soc.*, 1995, **117**, 5367–5368.

10 A. Medek, J. S. Harwood and L. Frydman, *J. Am. Chem. Soc.*, 1995, **117**, 12779–12787.

11 J.-P. Amoureux, C. Fernandez and S. Steuernagel, *J. Magn. Reson. Ser. A*, 1996, **123**, 116–118.

12 V. Lacassagne, C. Bessada, P. Florian, S. Bouvet, B. Ollivier, J.-P. Coutures and D. Massiot, *J. Phys. Chem. B*, 2002, **106**, 1862–1868.

13 V. Lacassagne, C. Bessada, B. Ollivier, D. Massiot, P. Florian and J.-P. Coutures, *Comptes Rendus l'Académie des Sci. - Ser. IIB*, 1997, **325**, 91–98.

14 A. Bielecki and D. P. Burum, *J. Magn. Reson. Ser. A*, 1995, **116**, 215–220.

15 P. A. Beckmann and C. Dybowski, *J. Magn. Reson.*, 2000, **146**, 379–380.

16 K. D. Becker, *J. Chem. Phys.*, 1978, **68**, 3785–3793.

17 J. Wu, N. Kim and J. F. Stebbins, *Solid State Nucl. Magn. Reson.*, 2011,

40, 45–50.

18 K. J. D. MacKenzie and M. E. Smith, *Multinuclear Solid-State Nuclear Magnetic Resonance of Inorganic Materials*, Elsevier, Oxford, 2002.

19 Z. Xu and J. F. Stebbins, *Science (80-.).*, 1995, **270**, 1332–1334.

20 Z. Xu and J. F. Stebbins, *Solid State Nucl. Magn. Reson.*, 1995, **5**, 103–112.

21 C. J. Pickard and F. Mauri, *Phys. Rev. B*, 2001, **63**, 245101.

22 J. R. Yates, C. J. Pickard and F. Mauri, *Phys. Rev. B*, 2007, **76**, 024401.

23 D. S. Middlemiss, F. Blanc, C. J. Pickard and C. P. Grey, *J. Magn. Reson.*, 2010, **204**, 1–10.

24 F. Blanc, D. S. Middlemiss, Z. Gan and C. P. Grey, *J. Am. Chem. Soc.*, 2011, **133**, 17662–17672.

25 D. Laurencin and M. E. Smith, *Prog. Nucl. Magn. Reson. Spectrosc.*, 2013, **68**, 1–40.

26 R. Dervişoğlu, D. S. Middlemiss, F. Blanc, Y.-L. Lee, D. Morgan and C. P. Grey, *Chem. Mater.*, 2015, **27**, 3861–3873.

27 M. Choi, K. Matsunaga, F. Oba and I. Tanaka, *J. Phys. Chem. C*, 2009, **113**, 3869–3873.

28 L. Enciso-Maldonado, M. S. Dyer, M. D. Jones, M. Li, J. L. Payne, M. J. Pitcher, M. K. Omir, J. B. Claridge, F. Blanc and M. J. Rosseinsky, *Chem. Mater.*, 2015, **27**, 2074–2091.

29 C. Bonhomme, C. Gervais, F. Babonneau, C. Coelho, F. Pourpoint, T. Azaïs, S. E. Ashbrook, J. M. Griffin, J. R. Yates, F. Mauri and C. J. Pickard, *Chem. Rev.*, 2012, **112**, 5733–5779.

30 M. Smith, *Prog. Nucl. Magn. Reson. Spectrosc.*, 1999, **34**, 159–201.

31 R. D. Shannon, *Acta Crystallogr. Sect. A*, 1976, **A32**, 751–767.

32 P. Bottke, D. Freude and M. Wilkening, *J. Phys. Chem. C*, 2013, **117**, 8114–8119.

33 C. Vinod Chandran, S. Pristat, E. Witt, F. Tietz and P. Heitjans, *J. Phys. Chem. C*, 2016, **120**, 8436–8442.

34 K. Volgmann, V. Werth, S. Nakhal, M. Lerch, T. Bredow and P. Heitjans, *Zeitschrift fur Phys. Chemie*, 2017, **231**, 1243–1262.

35 T. Pietrass, F. Taulelle, P. Lavela, J. Olivier-Fourcade, J.-C. Jumas and S. Steuernagel, *J. Phys. Chem. B*, 1997, **101**, 6715–6723.

36 R. Böhmer, K. R. Jeffrey and M. Vogel, *Prog. Nucl. Magn. Reson. Spectrosc.*, 2007, **50**, 87–174.

37 O. Bohnke, J. Emery and J. L. Fourquet, *Solid State Ionics*, 2003, **158**, 119–132.

38 J. Emery, J. . Buzare, O. Bohnke and J. . Fourquet, *Solid State Ionics*, 1997, **99**, 41–51.

39 W. Bucheli, K. Arbi, J. Sanz, D. Nuzhnyy, S. Kamba, A. Várez and R. Jimenez, *Phys. Chem. Chem. Phys.*, 2014, **16**, 15346–15354.

40 H. Buschmann, J. Dölle, S. Berendts, A. Kuhn, P. Bottke, M. Wilkening, P. Heitjans, A. Senyshyn, H. Ehrenberg, A. Lotnyk, V. Duppel, L. Kienle and J. Janek, *Phys. Chem. Chem. Phys.*, 2011, **13**, 19378.

41 A. Abragam, *The Principles of Nuclear Magnetism*, Oxford University Press, Oxford, 1961.

42 P. Heitjans, A. Schirmer and S. Indris, *NMR and β-NMR Studies of Diffusion in Interface-Dominated and Disordered Solids*, Springer-Verlag Berlin Heidelberg, The Netherlands, 2005.

43 M. Wilkening and P. Heitjans, *ChemPhysChem*, 2012, **13**, 53–65.

44 A. Kuhn, P. Sreeraj, R. Pöttgen, H. D. Wiemhöfer, M. Wilkening and P. Heitjans, *J. Am. Chem. Soc.*, 2011, **133**, 11018–11021.

45 N. Bloembergen, E. M. Purcell and R. V Pound, *Phys. Rev.*, 1948, **73**, 679–712.

46 J. Emery, O. Bohnké, J. L. Fourquet, J. Y. Buzaré, P. Florian and D. Massiot, *J. Phys. Condens. Matter*, 2002, **14**, 523–539.

47 O. Bohnke, *Solid State Ionics*, 2008, **179**, 9–15.

48 A. Kuhn, V. Duppel and B. V. Lotsch, *Energy Environ. Sci.*, 2013, **6**, 3548.

49 V. Epp, Ö. Gün, H.-J. Deiseroth and M. Wilkening, *J. Phys. Chem. Lett.*, 2013, **4**, 2118–2123.

50 V. Epp, Q. Ma, E.-M. Hammer, F. Tietz and M. Wilkening, *Phys. Chem. Chem. Phys.*, 2015, **17**, 32115–32121.

51 B. A. Huberman and J. B. Boyce, *Solid State Commun.*, 1978, **25**, 843–846.

52 J. A. Huwaldt, Plot Digitizer, https://sourceforge.net/projects/plotdigitizer/.

53 S. Geller, *Solid Electrolytes*, Springer, Berlin, 1977.

54 L. Latie, G. Villeneuve, D. Conte and G. Le Flem, *J. Solid State Chem.*, 1984, **51**, 293–299.

55 Y. Deng, C. Eames, J.-N. Chotard, F. Lalère, V. Seznec, S. Emge, O. Pecher, C. P. Grey, C. Masquelier and M. S. Islam, *J. Am. Chem. Soc.*, 2015, **137**, 9136–9145.

56 K. Arbi, M. G. Lazarraga, D. Ben Hassen Chehimi, M. Ayadi-Trabelsi, J. M. Rojo and J. Sanz, *Chem. Mater.*, 2004, **16**, 255–262.

57 C. León, M. Lucia, J. Santamaria and M. París, *Phys. Rev. B*, 1996, **54**, 184–189.

58 N. Kim, C. H. Hsieh, H. Huang, F. B. Prinz and J. F. Stebbins, *Solid State Ionics*, 2007, **178**, 1499–1506.

59 L. Holmes, L. Peng, I. Heinmaa, L. A. O'Dell, M. E. Smith, R.-N. Vannier and C. P. Grey, *Chem. Mater.*, 2008, **20**, 3638–3648.

5. New NASICON materials

5.1 Introduction

The best Li^+ ion conductor with the NASICON framework is the Al-doped $LiTi_2(PO_4)_3$ series, as detailed in the Chapter 3, and consists of high ionic conductivity of 4~6 x 10^{-3} S cm^{-1} at 300 °C with low activation barriers of ~0.3 eV.[1,2] Despite these attractive characteristics, these materials have difficulty finding application as a battery electrolyte, as the Ti^{4+} reduces to Ti^{3+} when in contact with lithium and introduces electronic conductivity to the material, short-circuiting the battery.[3,4] Thangadurai *et al*. reported the $LiM^{V}M^{III}(PO_4)_3$ series (M^{V}=Nb, Ta; M^{III}=Al, Cr, Fe), which consists of the same NASICON crystal structure without the Ti^{4+} disadvantages.[5] Out of the series, the NASICON $LiTaAl(PO_4)_3$ was reported with the best conductivity at 1.0 x 10^{-2} S cm^{-1} at 350 ^{o}C, comparable to the conductivity of the $LiTi_2(PO_4)_3$ of 6.3 x 10^{-3} S cm^{-1} at the same temperature. This non-Ti containing NASICON material was then chosen to study and improve ionic conductivity on.

One approach to increase Li^+ conductivity formation of Li^+ vacancies or interstitial sites are required.[6,7] To form Li^+ interstitials, we aim to dope Ca^{2+} on the Ta^{5+}/Al^{3+} octahedral site in $LiTaAl(PO_4)_3$, charge compensated by increased Li^+ content which form the targeted interstitials. This may lead to higher conductivity with more Li^+ diffusion pathways or lower conductivity due to percolation limitations of the Li^+ ions.

Two new materials with the compositions $Li_{0.925}Ta_{1.062}Al_{0.938}P_{3.16}O_{12+x}$ and $Li_{0.734}Ta_{1.187}Ca_{0.108}Al_{0.705}P_3O_{12}$ were synthesised by Dr. Chris Collins and Dr. Leopoldo Enciso-Maldonado, respectively. Both compositions were

indexed to the NASICON crystal structure, with the Ca-doped composition having a larger unit cell, which suggests successful Ca doping into the NASICON framework. Both samples also contained $AlPO_4$ impurities (cristobalite and tridymite type for the parent sample, cristobalite type for the Ca-doped sample), though their relative amounts were not stated.[8] Conductivities of both compositions were measured by AC impedance spectroscopy using Ag paste electrodes and $Li_{0.925}Ta_{1.062}Al_{0.938}P_{3.16}O_{12+x}$ was found to have a conductivity of 1.3 x 10^{-7} S cm^{-1} at 30 ^oC, with an activation barrier of 0.47(1) eV, on the same order of magnitude to $LiTaAl(PO_4)_3$ and $Li_{1.2}Ta_{0.9}Al_{1.1}(PO_4)_3$ at the same temperature (6.5 x 10^{-7} S cm^{-1}, 0.47–0.51 eV). On the other hand, the Ca-doped material show a significant drop in conductivity at 1.5 x 10^{-13} S cm^{-1} at 25 ^oC with a high activation barrier of 0.8 eV. It is suggested that this is caused either by the lower Li content in the NASICON, or possibly Ca being present on the A_1 or A_2 site, blocking the Li^+ diffusion pathway. Further details on synthesis conditions, and analysis of powder X-ray diffraction and AC impedance spectroscopy are available in Dr. Leopoldo Enciso-Maldonado's thesis.[8]

This chapter here presents the solid state NMR investigation of the structure and Li^+ dynamics of the two NASICON materials– $Li_{0.925}Ta_{1.062}Al_{0.938}P_{3.16}O_{12+x}$ and $Li_{0.734}Ta_{1.187}Ca_{0.108}Al_{0.705}P_3O_{12}$. Structural information is studied through the use of solid-state ^6Li, ^{27}Al and ^{31}P nuclear magnetic resonance (NMR) spectroscopy experiments. Insights into the Li^+ ion dynamics are obtained using variable temperature solid-state ^7Li NMR spectroscopy.

5.2 Experimental

^{6}Li, ^{27}Al and ^{31}P magic angle spinning (MAS) solid-state NMR experiments were carried out on a 9.4 T Bruker Avance III HD spectrometer equipped with a Bruker 4 mm HXY MAS probe in double resonance mode. ^{6}Li and ^{31}P MAS NMR spectra were obtained with a $\pi/2$ pulse length of 3 μs at a radio frequency (rf) amplitude of $\nu_1(^{6}\text{Li})$ = 83 kHz and a MAS rate of ν_r = 10 kHz. ^{27}Al 10^{o} flip angle NMR spectra were obtained at $\pi/18$ pulse lengths of 0.11 μs at a rf amplitude of $\nu_1(^{27}\text{Al})$ = 83 kHz and a MAS rate of ν_r = 12.5 kHz. ^{27}Al two-dimensional (2D) z-filtered multiple-quantum MAS (MQMAS)[9–11] experiments were also obtained. Excitation and reconversion pulses of rf amplitude $\nu_1(^{27}\text{Al})$ = 100 kHz and a selective $\pi/2$ pulse of $\nu_1(^{27}\text{Al})$ ≈ 1.5 kHz were used. Additional ^{27}Al NMR spectra were obtained on a 16.4 T Bruker Avance III on a 2.5 mm HX MAS probe at a MAS rate of 33 kHz and 20 T Bruker Avance III HD spectrometer on the 3.2 mm HXY MAS probe at a MAS rate of 22 kHz, with a $\pi/18$ pulse of pulse length 0.11 μs at a rf amplitude of $\nu_1(^{27}\text{Al})$ = 83 kHz. The ^{27}Al EXSY experiment was performed using the $\pi/6–t_1–-\pi/6–\tau_{mix}–\pi/6–$acq pulse sequence, with a soft $\pi/6$ pulse of pulse length 10 μs at a rf amplitude of $\nu_1(^{27}\text{Al})$ ≈ 2.5 kHz where t_1 is the increment time in the F1 direction and τ_{mix} is the mixing time. The large peak at ~-17.5 ppm and the overall fit of the ^{27}Al NMR spectra for $Li_{0.925}Ta_{1.062}Al_{0.938}P_{3.16}O_{12+x}$ was performed using the Gaussian isotropic model[12–14] (derived from the Czjzek distribution[15]) in dmfit.[16] All other simulations and fittings were performed using the SOLA package in Bruker TopSpin 3.2.

^{7}Li variable temperature solid-state NMR experiments were all obtained

under static conditions. Spectra below 650 K were recorded on a 9.4 T Bruker Avance III HD spectrometer with a Bruker 4 mm HX high temperature MAS probe (294 K–623 K) and a Bruker 4 mm HXY MAS probe in double resonance mode (< 294 K) using standard 4 mm ZrO_2 rotors and caps. Experiments above 650 K were carried out on a 9.4 T Bruker Avance spectrometer using a single channel high temperature static NMR probe with a homemade CO_2 laser (λ = 10.6 μm, 250 W) heating system developed in Orléans (CEMHTI−CNRS, France).[17,18] The BN crucible containing the sample is heated by two lasers passing axially through the NMR probe with the sample temperature controlled by the laser power output. A flow of N_2 gas is used to cool the rf coil of the NMR probe and a flow of Ar gas to prevent oxidation of the BN crucible at high temperature. ^{7}Li spectra were obtained with a $\pi/2$ pulse length of 1.5 μs at rf amplitude of $\nu_1(^7\text{Li})$ = 83 kHz below 650 K and with a 11.5 μs at rf amplitude of $\nu_1(^7\text{Li})$ = 11 kHz above 650 K. ^{7}Li spin-lattice relaxation times (T_1) were obtained using a saturation recovery pulse sequence and the data were fitted to a stretch exponential of the form $1 - \exp[-(\tau/T_1)^{\alpha}]$ where τ are variable delays and α is the stretch exponential coefficient (0.5–0.9). ^{7}Li spin-lattice relaxation times in the rotating frame ($T_{1\rho}$) were obtained with a spin-lock pulse sequence at frequencies of $\nu_1(^7\text{Li})$ = 5, 8 and 20 kHz on the MAS probe and $\nu_1(^7\text{Li})$ = 5 and 8 kHz on the static probe due to instrument limitations. $T_{1\rho}$ data were fitted to a stretch exponential of the form $\exp[-(\tau/T_{1\rho})^{\alpha}]$. Temperature calibrations of the MAS probes (< 650 K) were performed with the ^{207}Pb chemical shift thermometer of $Pb(NO_3)_2$,[19,20] and by following the ^{63}Cu resonances of $Cu^{I}I$ and $Cu^{I}Br$ across the γ-to-β phase transition at 642 K and 658 K, respectively.[21,22] Temperature calibration of the laser heated NMR

probe was carried out by the direct measurements of the melting points of reference samples.[17,18] All temperatures reported are actual sample temperatures and have an estimated accuracy of ± 5 K (< 294 K), ± 10 K (294–420 K), ± 20 K (420–650 K) and ± 30 K (> 650 K on the static laser probe).

Spectra were referenced to 10 M LiCl in D_2O (for $^{6,7}Li$), 0.1 $Al(NO_3)_3$ in H_2O (for ^{27}Al) and 85 % H_3PO_4 (for ^{31}P) at 0 ppm.

5.3 Results and Discussion

5.3.1 NMR: Structure

5.3.1.1 ^{27}Al

^{27}Al (I = 5/2) NMR provides sensitive analysis of multiple Al-containing phases and their Al coordination and have been used in studying structure and disorder in NASICON materials.[23–26] The ^{27}Al MAS NMR spectra and 3QMAS NMR spectra of $Li_{0.925}Ta_{1.062}Al_{0.938}P_{3.16}O_{12+x}$ obtained at 9.4 T are shown in Figure 5.1. Signals at ~40 ppm and ~–20 ppm are assigned to tetrahedrally and octahedrally coordinated Al sites, respectively.

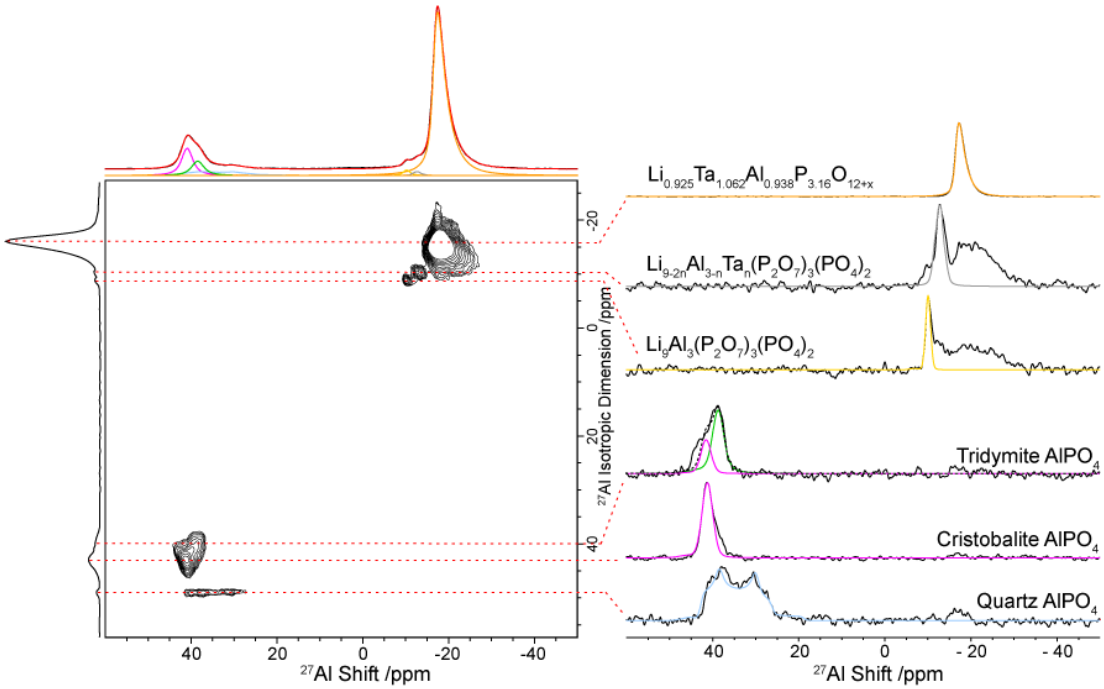

Figure 5.1. ^{27}Al 10° flip angle one pulse (top) and two-dimensional z-filtered MQMAS spectra of $Li_{0.925}Ta_{1.062}Al_{0.938}P_{3.16}O_{12+x}$ obtained at 9.4 T at a MAS rate of 12.5 kHz. The contour maximum of the octahedral Al in the NASICON has been cut to highlight the smaller resonances. Coloured solid lines represent the simulations of peaks using NMR parameters extracted from the slices and the sum of the simulated peaks. Pink: Cristobalite $AlPO_4$, Green: Tridymite $AlPO_4$, Light Blue: Quartz $AlPO_4$, Yellow: $Li_9Al_3(P_2O_7)_3(PO_4)_2$, Grey: $Li_{9-2n}Al_{3-n}Ta_n(P_2O_7)_3(PO_4)_2$, Orange: octahedral Al in NASICON, Red: Sum of all simulated peaks. The fit for the octahedral Al in the NASICON phase was performed using the Czjzek function in dmfit using the CzSimple model (see Chapter 2).

The octahedral Al region shows one large peak at ~–17.5 ppm and two smaller peaks slightly downfield at ~–10 ppm, which are partially resolved. The 3QMAS spectra resolves three distinct Al environments here. The large peak with an isotropic chemical shift $\delta_{iso,cs}$ of –16.7(1) ppm is observed to have a

large quadrupolar tail, which is associated to the distribution of quadrupolar interaction.[27] This is attributed to the octahedral Al environment within the NASICON, and could be influenced by the distortion of Al–O–P bonds, related to the distortion of the $[PO_4]^{3-}$ tetrahedra due to the higher charged Ta^{5+} [28] and the resulting anisotropic strain observed in the PXRD analysis.[8] The peak is fitted to a Czjzek function in dmfit using the CzSimple model (see Chapter 2 for details on this model),[16] and provides the average distribution of the EFG tensor as $\overline{C_Q}$[29,30] of 1.7(1) MHz (see Table 5.1 for parameters). The small peak at $\delta_{iso,cs}$ = –9.4(1) ppm is assigned to the phase $Li_9Al_3(P_2O_7)_3(PO_4)_2$, which although was not observed in the PXRD pattern of this sample,[8] perhaps due to its low content of ~2.6 wt% (calculated from NMR mol%), was observed by both PXRD and NMR in the NASICONs $Li_{1+x}Al_xGe_{2-x}(PO_4)_3$ ($x \geq 0.6$) prepared using similar starting materials.[26] The AlO_6 octahedra in this material is linked to six different PO_4 groups of 2 types, deshielding Al more compared to AlO_6 in the NASICON framework which are linked to 4 PO_4 groups.[31] The peak at $\delta_{iso,cs}$ = –11.3(2) ppm has similar NMR parameters as the peak at –9.4 ppm, and therefore one could assume they share a similar crystal structure with possibly similar composition to the $Li_9Al_3(P_2O_7)_3(PO_4)_2$, perhaps $Li_{9-2n}Al_{3-n}Ta_n(P_2O_7)_3(PO_4)_2$, where the change in Li^+ number decreases the deshielding of AlO_6 octahedra in the structure and shifts the resonance upfield. These two impurities ($Li_9Al_3(P_2O_7)_3(PO_4)_2$ and $Li_{9-2n}Al_{3-n}Ta_n(P_2O_7)_3(PO_4)_2$) are not observed in PXRD, perhaps due to their small amounts (Table 5.2), which puts them below the detection limit.

Table 5.1. Experimental NMR parameters of $Li_{0.925}Ta_{1.062}Al_{0.938}P_{3.16}O_{12+x}$ and $Li_{0.734}Ta_{1.187}Ca_{0.108}Al_{0.705}P_3O_{12}$ from ^{27}Al 3QMAS NMR and δ positions at infinite magnetic field B_0 derived from the changes in peak maxima δ_{max} against magnetic fields. The octahedral Al in the $Li_{0.925}Ta_{1.062}Al_{0.938}P_{3.16}O_{12+x}$ was fitted to the Czjzek function in the dmfit program using the CzSimple model.[32] $Li_{0.734}Ta_{1.187}Ca_{0.108}Al_{0.705}P_3O_{12}$ was not measured at high fields.

Composition	$\delta_{iso,cs}$ /ppm (MQMAS)	$\lvert C_Q \rvert$ /MHz	η_Q	$\delta_{iso,cs}$ /ppm (Extrapol-ation of δ_{max})	Assignment
$Li_{0.925}Ta_{1.062}Al_{0.938}P_{3.16}O_{12+x}$	42.2(1)	1.3(1)	0.8(1)	41.8(5.4)	Cristobalite $AlPO_4$
	44.6(3)	4.3(1)	0.30(5)	–	Quartz $AlPO_4$
	39.6(1)	1.3(1)	0.9(1)	40.2(13.0)	Tridymite $AlPO_4$
	-9.4(1)	1.1(1)	0.6(1)	-9.3(3.5)	$Li_9Al_3(P_2O_7)_3(PO_4)_2$
	-11.3(2)	1.6(1)	0.6(1)	-11.5(4.2)	$Li_{9-2n}Al_{3-n}Ta_n(P_2O_7)_3(PO_4)_2$
	-16.7(1)	1.7(1)[a]	–	-16.7(3.1)	Octahedral Al in main phase
$Li_{0.734}Ta_{1.187}Ca_{0.108}Al_{0.705}P_3O_{12}$	42.2(3)	1.3(1)	0.8(1)		Cristobalite $AlPO_4$
	39.6(3)	0.8(2)	0.9(1)		Tridymite $AlPO_4$
	-17.2(1)	1.3(1)	0.7(1)		Octahedral Al in main phase
	-19.7(2)	1.1(1)	0.8(1)		Octahedral Al in main phase

[a] The average quadrupolar coupling constant $\overline{C_Q}$ is determined here.

Table 5.2. Summary of phases present in $Li_{0.925}Ta_{1.062}Al_{0.938}P_{3.16}O_{12+x}$ and $Li_{0.734}Ta_{1.187}Ca_{0.108}Al_{0.705}P_3O_{12}$ and their relative mol and wt % derived from ^{27}Al and ^{31}P NMR.

Composition	Phase	27Al mol%	27Al wt%	31P mol%	31P wt%
$Li_{0.925}Ta_{1.062}Al_{0.938}P_{3.16}O_{12+x}$[a]	Cristobalite $AlPO_4$	10.6%	3.0%	5.7%	1.5%
	Quartz $AlPO_4$	5.8%	1.6%	4.1%	1.1%
	Tridymite $AlPO_4$	6.1%	1.7%	5.5%	1.5%
	$Li_9Al_3(P_2O_7)_3(PO_4)_2$	1.3%	2.6%	0.6%	1.2%
	$Li_{9-2n}Al_{3-n}Ta_n(P_2O_7)_3(PO_4)_2$[b]	0.9%	1.8%	0.8%	1.5%
	$Li_4P_2O_7$	–	–	3.3%	1.5%
	NASICON	75.3%	89.3%	79.9%	91.6%
$Li_{0.734}Ta_{1.187}Ca_{0.108}Al_{0.705}P_3O_{12}$	Cristobalite $AlPO_4$	10.5%	2.8%	2.3%	0.6
	Tridymite $AlPO_4$	6.2%	1.6%	3.6	0.9
	NASICON	83.2%	95.5%	94.1%	98.6%

[a] x calculated as 0. [b] n calculated as 0.1

In the tetrahedral Al region at ~40 ppm, three distinct NMR signals with very different line shapes are observed in the 3QMAS NMR spectra. The peaks in this region have been a point of discussion in literature in many NASICON based materials, such as the resonances being assigned to the AlO_4^- unit in the main phase with partial substitution of the P species.[23,24,26,33,34] ^{27}Al–^{31}P correlation experiments including $^{27}Al\{^{31}P\}$ REDOR on the NASICON $Li_{1+x}Al_xGe_{2-x}(PO_4)_3$ phases show that this is not the case.[26,33] With this in mind, ^{27}Al exchange spectroscopy NMR on $Li_{0.925}Ta_{1.062}Al_{0.938}P_{3.16}O_{12+x}$ was done to investigate if we observe any interaction between the two regions (Figure 5.2). The mixing time τ_{mix} of 40 ms was chosen as the spin-lattice relaxation time T_1

of the octahedral region was estimated ~150 ms. No cross peaks were observed, suggesting the two regions are not in close proximity i.e. not within the NASICON framework. The NMR parameters of these peaks at ~40 ppm correspond to the three polymorphs of $AlPO_4$ reported values in literature,[35] and are assigned to cristobalite, quartz and tridymite $AlPO_4$ phases with $\delta_{iso,cs}$ of 44.2(1), 44.6(3) and 39.6(1) ppm, respectively.

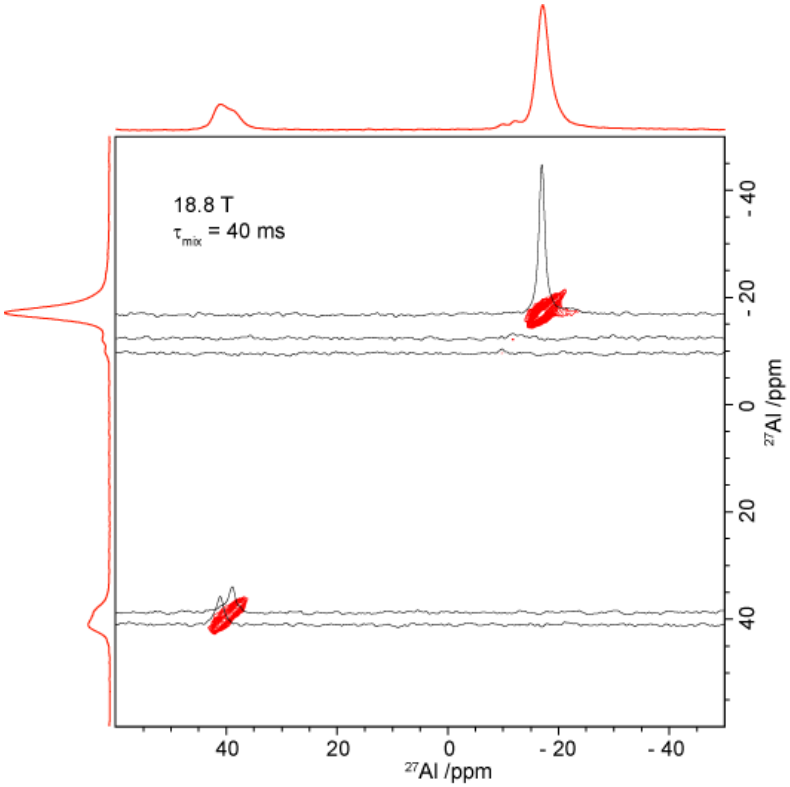

Figure 5.2. ^{27}Al exchange spectroscopy NMR spectra of $Li_{0.925}Ta_{1.062}Al_{0.938}P_{3.16}O_{12+x}$ obtained at 18.8 T at a MAS rate of 33 kHz with a mixing time τ_{mix} of 40 ms. Black lines within the 2D contour plot represents the extracted horizontal slices at the respective shifts. No cross peaks are observed, suggesting that the shifts are not in close proximity.

The ^{27}Al MAS NMR spectra of $Li_{0.925}Ta_{1.062}Al_{0.938}P_{3.16}O_{12+x}$ measured at different magnetic fields are shown in Figure 5.3a. The large broad peak

assigned to octahedral Al in the main phase narrows with magnetic field strength (from 12.5 to 33 kHz from 9.4 to 20 T) as expected if the second order quadrupolar broadening coupling is the dominant NMR interaction.[27] The isotropic shift $\delta_{iso,CS}$ can also be estimated by plotting the centre of gravity against B_0^{-2} (see Chapter 2, equation 2.13),[27,36,37] as the intercept where $B_0^{-2} = 0$ simulates carrying out NMR experiments at high (infinite) magnetic fields where all quadrupolar interactions are suppressed. The centre of gravity of the ^{27}Al peaks for all peaks excluding the quartz $AlPO_4$ are within 0.5 ppm of the peak maxima δ_{max} with low C_Q in the 3QMAS spectra at 9.4 T due to small 2nd order quadrupolar broadening (Figure 5.1, right) and is therefore used to plot against B_0^{-2} (Figure 5.3b).[27] For the peaks in the octahedral Al region, $\delta_{iso,CS}$ was determined as ~–16.7(3.1), ~–11.5(4.2) and ~–9.3(3.5) ppm for the $Li_{0.925}Ta_{1.062}Al_{0.938}P_{3.16}O_{12+x}$ NASICON phase, $Li_9Al_3(P_2O_7)_3(PO_4)_2$ and $Li_{9-2n}Al_{3-n}Ta_n(P_2O_7)_3(PO_4)_2$, respectively, complementing the 3QMAS NMR data in Table 5.1. Peaks for cristobalite $AlPO_4$ and tridymite $AlPO_4$ were also plotted and gave $\delta_{iso,CS}$ as ~41.8(5.4) and ~40.2(13.0) ppm, respectively.

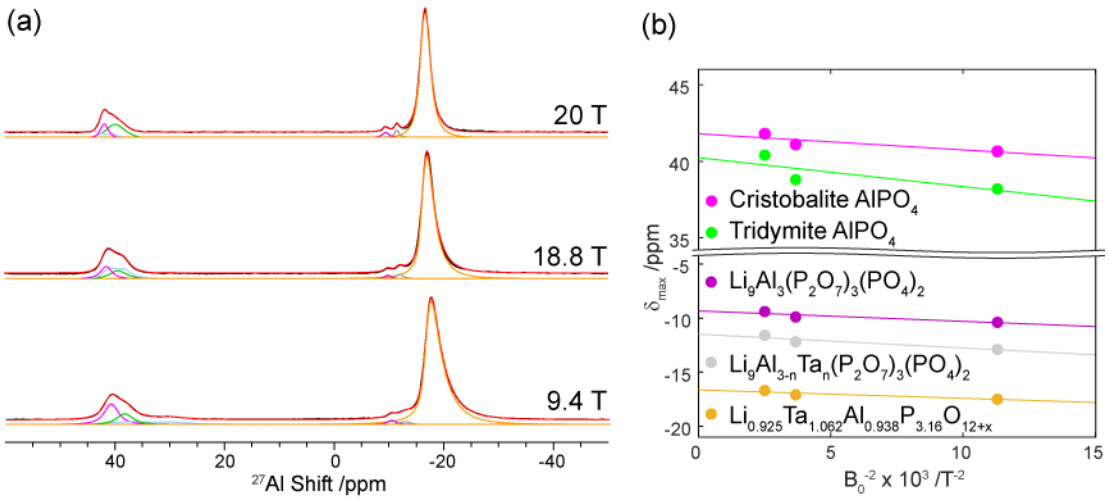

Figure 5.3. (a) ^{27}Al 10° flip angle MAS NMR spectra of $Li_{0.925}Ta_{1.062}Al_{0.938}P_{3.16}O_{12+x}$ at different magnetic fields. MAS rates are 12.5 kHz, 33 kHz and 22 kHz for at 9.4 T, 18.8 T and 20 T, respectively. (b) Plot of peak maximum positions δ_{max} against B_0^{-2}. Quartz $AlPO_4$ is not shown here as its high C_Q, shifting the centre of gravity from its peak maximum δ_{max}.

The ^{27}Al MAS NMR and 3QMAS NMR spectra for the second phase of interest $Li_{0.734}Ta_{1.187}Ca_{0.108}Al_{0.705}P_3O_{12}$, is shown in Figure 5.4. Similarly to $Li_{0.925}Ta_{1.062}Al_{0.938}P_{3.16}O_{12+x}$, tetrahedral and octahedral Al sites are observed. In the octahedral Al region, two resonances are observed at $\delta_{iso,cs}$ of –17.2(1) and –19.7(2) ppm (Table 5.1). The two peaks have similar quadrupolar parameters (C_Q of 1.3(1) and 1.1(1) MHz, respectively), and are therefore assigned to the Al environments within the NASICON phase, with the further upfield peak may be environments in close proximity to Ca^{2+} environments due to less shielding from the lower charged cation. In the tetrahedral region, the two peaks with $\delta_{iso,cs}$ of 44.2(3) and 39.6(3) ppm are assigned to the cristobalite $AlPO_4$ phase, observed by PXRD, and the tridymite $AlPO_4$, which are not observed by PXRD.[8]

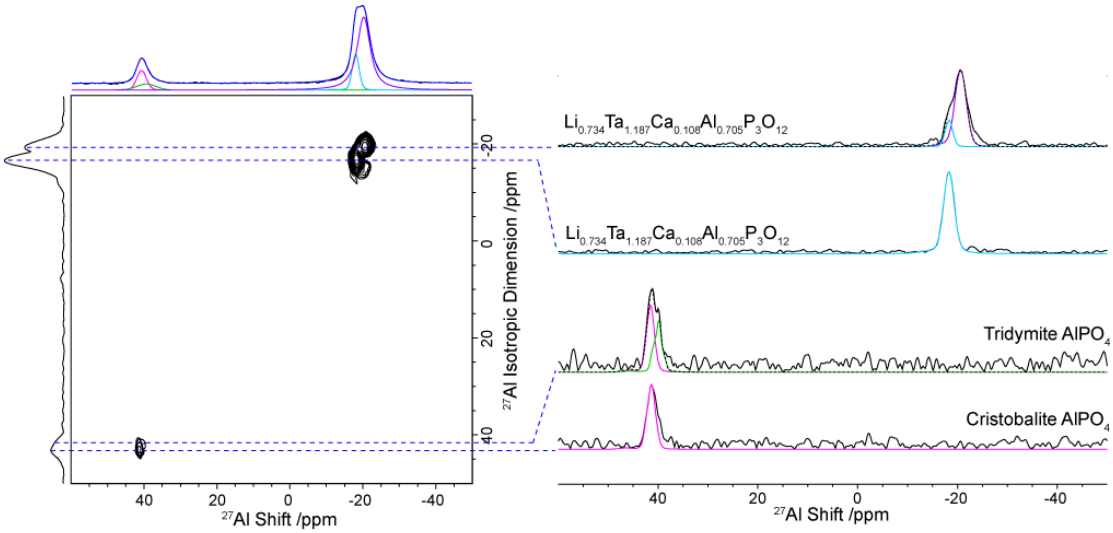

Figure 5.4. ^{27}Al 10º flip angle one pulse (top) and two-dimensional z-filtered MQMAS spectra of $Li_{0.734}Ta_{1.187}Ca_{0.108}Al_{0.705}P_3O_{12}$ obtained at 9.4 T at a MAS rate of 12.5 kHz. Coloured solid lines represent the simulations of peaks using NMR parameters extracted from the slices and the sum of the simulated peaks. Pink: Cristobalite $AlPO_4$, Green: Tridymite $AlPO_4$, Cyan/Purple: octahedral Al in NASICON, Blue: Sum of all simulated peaks.

5.3.1.2 ^{31}P

^{31}P (I = 1/2) MAS NMR is obtained to further understand information on the phases identified in $Li_{0.925}Ta_{1.062}Al_{0.938}P_{3.16}O_{12+x}$ (Figure 5.5a). The large broad peak consisting of multiple overlapping environments spanning from –20 ppm to –30 ppm is assigned to the PO_4 environments observed in the NASICON structure, an agreement with previous studies when investigating materials of similar crystal structures.[26,34,38,39] $AlPO_4$ phases seen by ^{27}Al NMR spectroscopy are also detected and are fitted accordingly.[35] This region is fit to peaks that appear in range with the impurities observed in ^{27}Al NMR spectroscopy, including resonances from each polymorph of $AlPO_4$ impurities

(pink for cristobalite $AlPO_4$, green for tridymite $AlPO_4$ and light blue for quartz $AlPO_4$) obtained from literature.[35] Five orange peaks are selected to represent the $P(OAl)_{4-x}(OTa)_x$ ($0 < x < 4$) environments (i.e. the $[PO_4]^{3-}$ group bridging to Ta^{5+} or Al^{3+}) within the NASICON structure. The peaks are assumed to be shifting left with higher Ta^{5+} content due to the larger deshielding of P caused by the higher charge Ta^{5+} cation compared to the smaller Al^{3+}. Exact assignments may be possible using ^{27}Al–^{31}P double resonance experiments such as REDOR and REAPDOR as reported in $Li_{1+x}Al_xGe_{2-x}(PO_4)_3$,[26,33] however the large overlap of the resonances could hinder that approach, possibly necessitating other techniques such as DFT calculations.

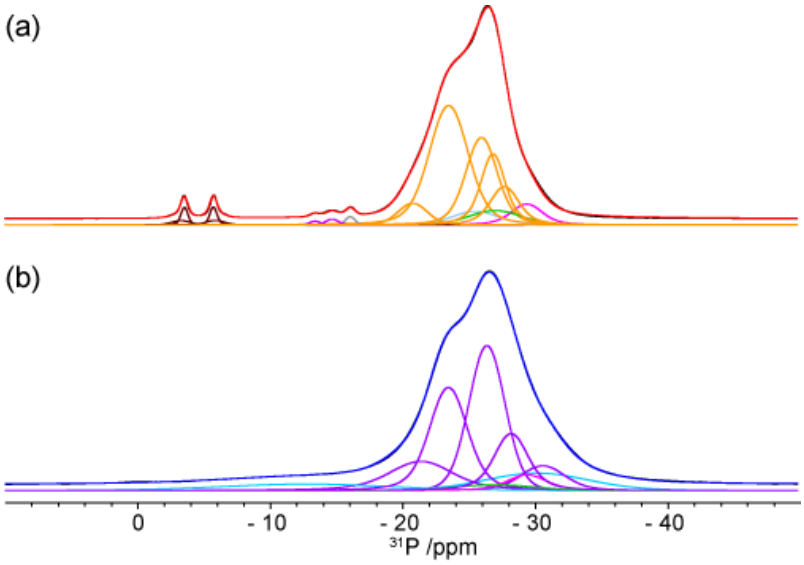

Figure 5.5. ^{31}P MAS NMR spectra of (a) $Li_{0.925}Ta_{1.062}Al_{0.938}P_{3.16}O_{12+x}$ and (b) $Li_{0.734}Ta_{1.187}Ca_{0.108}Al_{0.705}P_3O_{12}$ obtained at 9.4 T at a MAS rate of 10 kHz. The red and blue solid lines represent the sum of those simulated peaks. Orange/Purple: PO_4^- in NASICON phase, Cyan: PO_4^- group in NASICON neighbouring Ca^{2+}, Pink: cristobalite $AlPO_4$, Green: Tridymite $AlPO_4$, Light Blue: Quartz $AlPO_4$, Magenta: $Li_9Al_3(P_2O_7)_3(PO_4)_2$, Grey: $Li_9Al_{3-n}Ta_n(P_2O_7)_3(PO_4)_2$, Brown: $Li_4P_2O_7$.

The two sharp and broad peaks at ~–5 ppm are assigned as $Li_4P_2O_7$,[26] which is also observed in the PXRD pattern and most likely arising from both crystalline and amorphous $Li_4P_2O_7$ being present in $Li_{0.925}Ta_{1.062}Al_{0.938}P_{3.16}O_{12+x}$. These peaks arise from the two P environments in $Li_4P_2O_7$ with slightly different shielding, caused by the slight difference in P–O bond lengths in the P_2O_7 group.[40] Small slightly broader peaks are observed at –13.5, –14.8, –16.2 ppm. The peaks at –13.5 and –14.8 ppm are assigned to the PO_4 and P_2O_7 groups in $Li_9Al_3(P_2O_7)_3(PO_4)_2$ respectively.[26] The PO_4:P_2O_7 ratio in $Li_9Al_3(P_2O_7)_3(PO_4)_2$ is expected to be 1:3, however we observe a ratio of 1:2.0(3). This discrepancy is possibly caused by the extra resonance observed at –16.2 ppm, which could be assigned to the P_2O_7 group in $Li_{9-2n}Al_{3-n}Ta_n(P_2O_7)_3(PO_4)_2$, and the PO_4 peak overlapping with the PO_4 peak in $Li_9Al_3(P_2O_7)_3(PO_4)_2$.

The ^{31}P MAS NMR spectrum for $Li_{0.734}Ta_{1.187}Ca_{0.108}Al_{0.705}P_3O_{12}$ is shown in Figure 5.5b. A broad resonance consisting of at least 5 overlapping peaks are observed between –20 and –35 ppm and are assigned to the PO_4 environments in the NASICON phase, which represent the $P(OAl)_{4-x}(OTa)_x$ environments with increase in x from low to high shift ($0 < x < 4$), similarly to $Li_{0.925}Ta_{1.062}Al_{0.938}P_{3.16}O_{12+x}$. The shifts are generally at lower shift compared to those observed in $Li_{0.925}Ta_{1.062}Al_{0.938}P_{3.16}O_{12+x}$, (i.e. more shielded), which may be related to Ca^{2+} doping, reducing the deshielding effect in the NASICON framework. The broad shifts at ~–11 ppm and ~–30 ppm (cyan) can be assigned either as a PO_4 group directly neighbouring Ca^{2+} doped on the Ta/Al site or Li deficient sites due to the low Li content, however other approaches

and methodologies may be required for exact assignments.

The molar and weight % of each phase derived from ^{31}P NMR is presented in Table 5.2. In $Li_{0.925}Ta_{1.062}Al_{0.938}P_{3.16}O_{12+x}$, both ^{27}Al and ^{31}P NMR show the wt content of the main NASICON phase is approximately 90 wt%, with the impurity phases all consisting < 2 wt% each within the sample. For $Li_{0.734}Ta_{1.187}Ca_{0.108}Al_{0.705}P_3O_{12,}$ the main NASICON phase is derived as > 95 wt% with very small amounts of impurities. These low amounts would not give rise to peaks in the PXRD pattern to allow weight fraction refinement on each phase, and therefore is not derived in both compositions.

5.3.1.3 ^{6}Li

The ^{6}Li MAS NMR data on $Li_{0.925}Ta_{1.062}Al_{0.938}P_{3.16}O_{12+x}$ is shown in Figure 5.6a and shows a complex overlap of multiple resonances arising from the Li containing phases identified in ^{27}Al and ^{31}P NMR (Table 5.1). The large narrow peak at ~–1.3 ppm is assigned as the Li environment in the NASICON structure, similar to $LiTi_2(PO_4)$.[41] The complex overlap of broad resonances can be rationalised as $Li_4P_2O_7$, $Li_9Al_3(P_2O_7)_3(PO_4)_2$ and $Li_{9}Al_{3-n}Ta_n(P_2O_7)_3(PO_4)_2$, however individual assignments would require complementary approaches such as DFT calculations.

The ^{6}Li MAS NMR spectrum for $Li_{0.734}Ta_{1.187}Ca_{0.108}Al_{0.705}P_3O_{12}$ is given in Figure 5.6b. Unlike the undoped phase, this shows a broad peak at ~–0.8 ppm and a sharp peak at ~–2 ppm. The peaks are respectively assigned to the 6-coordinated A_1 Li sites and 8-coordinated A_2 Li site in the NASICON structure using the well established relationship of ^{6}Li shift and Li coordination.[42–44] These features are probably not observed in

$Li_{0.925}Ta_{1.062}Al_{0.938}P_{3.16}O_{12+x}$ due to its faster Li^+ conductivity as observed by impedance spectroscopy[8] and Li^+ dynamics (see below).

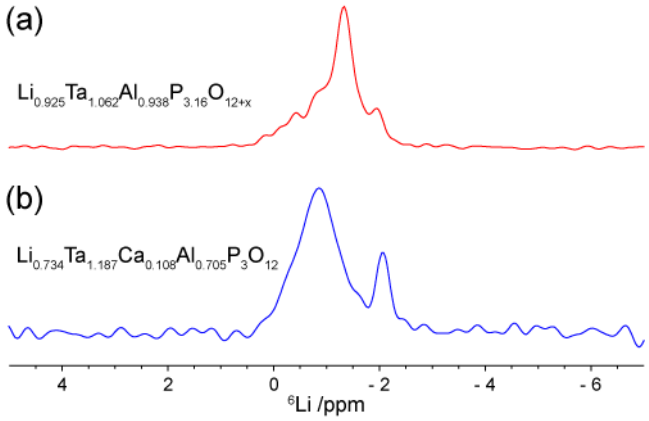

Figure 5.6. ^6Li MAS NMR spectra of (a) $Li_{0.925}Ta_{1.062}Al_{0.938}P_{3.16}O_{12+x}$ and (b) $Li_{0.734}Ta_{1.187}Ca_{0.108}Al_{0.705}P_3O_{12}$ obtained at 9.4 T at a MAS rate of 10 kHz.

5.3.2 Dynamics

5.3.2.1 NMR Li^+ Dynamics: Line Width Analysis

The ^7Li static NMR spectra of $Li_{0.925}Ta_{1.062}Al_{0.938}P_{3.16}O_{12+x}$ obtained in the temperature range of 123 K–1432 K are shown in Figure 5.7. The spectrum at 123 K show a broad ^7Li NMR line shape, consisting of a dipolar broadened central peak corresponding to the +1/2↔–1/2 central transition by ^7Li–^7Li homonuclear dipolar interactions, and the broad resonance spanning ~640 ppm (~100 kHz) corresponding to the +3/2↔+1/2 and -1/2↔-3/2 satellite transitions. The dipolar interactions average out as temperature is increased, increasing Li^+ ions mobility, yielding motional narrowing of NMR line widths (see Chapter 2).

Above 350 K, the motionally narrowed static ^7Li NMR spectra shows the satellite transitions of the NMR spectra widen as temperature increase (Figure 5.7, black dotted lines). The C_Q of ^7Li can be measured as the distance

between the satellite peaks ($\omega_Q/2\pi$) using the equation $C_Q = 2\cdot\omega_Q/2\pi$.[45] At 373 K, the singularities are observed and a quadrupolar constant C_Q of ~43 kHz can be estimated. With further increase in temperature, these signals broaden, indicating increase in C_Q up until ~56 kHz at ~750 K and stay constant at higher temperatures (Figure 5.8). A similar trend was reported in the ^{7}Li NMR study of in the NASICONs $LiTi_2(PO_4)_3$,[39] $Li_{1.3}Al_{0.3}Ti_{1.7}(PO_4)_3$[28,46] and $Li_{1.3}Al_{0.15}Y_{0.15}Ti_{1.7}(PO)_3$,[47] and is ascribed to the distortion of the $M(PO_4)_3$ NASICON skeleton as temperature is increased, induced by anisotropic thermal expansion of the crystal structure along the c-axis. Since the main Li^+ diffusion pathway is along the c-axis (see Chapter 3), one can ascribe the increase in C_Q as the increase in Li^+ diffusion along this axis and increase anisotropy to the quadrupolar interactions in ^{7}Li. As temperature increases, Li^+ mobility would increase and so would the anisotropy, which then increases the C_Q and therefore widens the satellite transitions peaks. Although variable temperature XRD data on our phases are not available, these observations are consistent with those reported in diffraction studies on other various NASICON phases such as $LiZr_2(PO_4)_3$, $LiTi_2(PO_4)_3$ and $Li_{1.3}Al_{0.3}Ti_{1.7}(PO_4)_3$.[48–51] We can therefore assume similarly that, with higher temperatures, the distortion of the $Ta/Al(PO_4)_3$ framework increases, increasing Li^+ mobility in one direction, resulting in an increase in ^{7}Li C_Q. The satellites do not increase after ~750 K, possibly due to the quadrupolar interactions being fully averaged to 0 along the direction of Li^+ motion, but still present in all other directions.

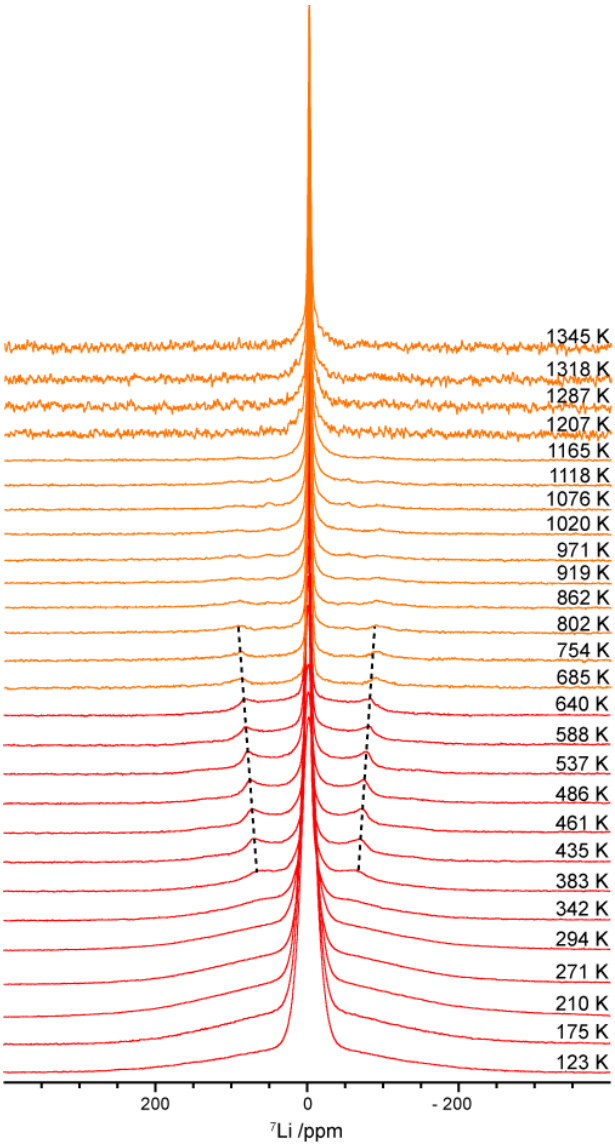

Figure 5.7. Variable temperature static ^{7}Li NMR spectra of $Li_{0.925}Ta_{1.062}Al_{0.938}P_{3.16}O_{12+x}$ obtained at 9.4 T on the MAS probe (red) and static laser probe (orange). Black dotted lines show the widening of the satellite transitions. Spectra above 1165 K have significantly lower S/N ratio compared to those below on the same probe, due to time constraints during experimentation. S/N ratio decrease with increasing temperatures due to the smaller population difference (Equation 2.2) which decreases the intensity of the FID signal.

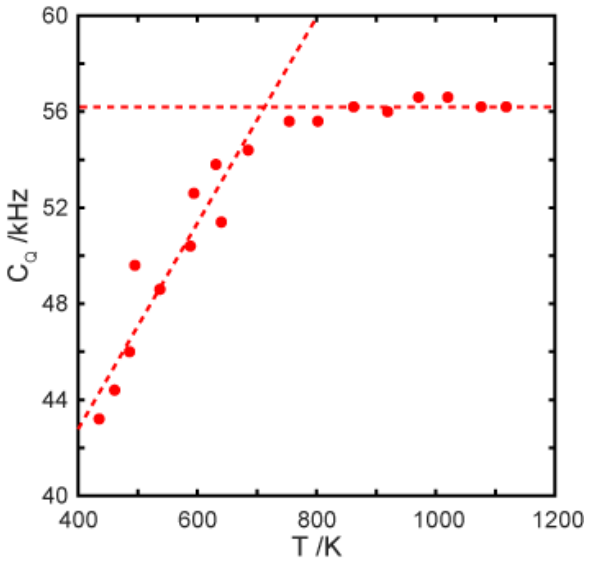

Figure 5.8. Temperature dependence of the C_Q in $Li_{0.925}Ta_{1.062}Al_{0.938}P_{3.16}O_{12+x}$. Dashed lines are guide to the eye.

The static ^7Li NMR spectra for $Li_{0.734}Ta_{1.187}Ca_{0.108}Al_{0.705}P_3O_{12}$ obtained at the same range of temperatures are shown in Figure 5.9. The broad resonances arising from the satellite transitions in the ^7Li NMR spectrum are not observed. A single resonance ^7Li–^7Li homonuclear dipolar broadened (fwhm ~4.1 kHz) is observed at 139 K, and narrows down with increasing temperature, indicating of Li^+ mobility.

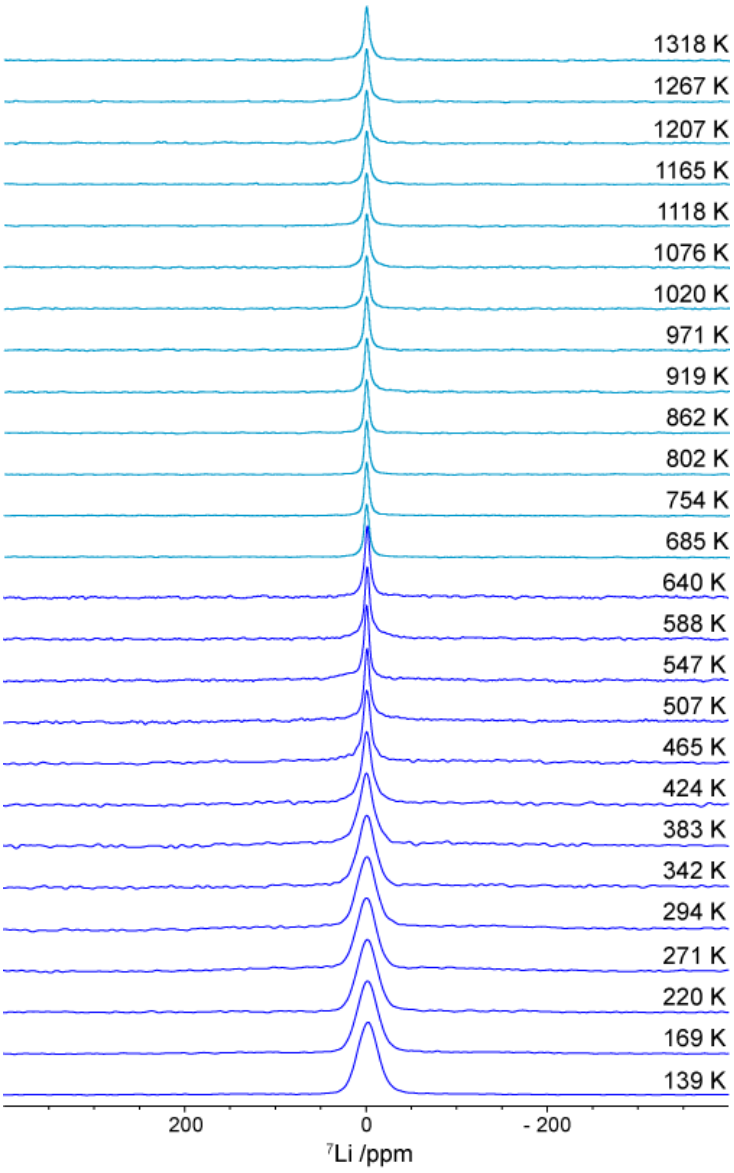

Figure 5.9. Variable temperature static 7Li NMR spectra of $Li_{0.734}Ta_{1.187}Ca_{0.108}Al_{0.705}P_3O_{12}$ obtained at 9.4 T on the MAS probe (blue) and the static laser probe (cyan).

The temperature dependence of ^7Li NMR line widths for $Li_{0.925}Ta_{1.062}Al_{0.938}P_{3.16}O_{12+x}$ and $Li_{0.734}Ta_{1.187}Ca_{0.108}Al_{0.705}P_3O_{12}$ are shown in Figure 5.10. Line width narrows as temperature increase, indicative of Li^+ mobility in both materials. The onset temperature of motional narrowing is lower for $Li_{0.925}Ta_{1.062}Al_{0.938}P_{3.16}O_{12+x}$, signifying the faster Li^+ dynamics in the

undoped sample compared to the Ca-doped sample, complementing the ACIS results. Using the sigmoidal regression fits (Figure 5.10, solid lines), we can estimate the Li^+ jump rates τ^{-1} in the rigid lattice regime $\Delta\omega_{rigid\ lattice}$ from the inflection point of the curve (green circle of the intersecting red and blue dotted lines) as ~2.3(1) x 10^4 s^{-1} and 2.6(1) x 10^{-4} s^{-1} at 266(5) K and 392(5) K for $Li_{0.925}Ta_{1.062}Al_{0.938}P_{3.16}O_{12+x}$ and $Li_{0.734}Ta_{1.187}Ca_{0.108}Al_{0.705}P_3O_{12}$, respectively. Above 500 K, we observe further narrowing of the central transition of ^7Li NMR line width in $Li_{0.925}Ta_{1.062}Al_{0.938}P_{3.16}O_{12+x}$ (Figure 5.10, red dashed line), possibly corresponding to further local structural changes as seen by the change in C_Q (Figure 5.8), or physical changes to the Li-containing impurities – $Li_4P_2O_7$,[40] $Li_9Al_3(P_2O_7)_3(PO_4)_2$ and $Li_{9-2n}Al_{3-n}Ta_n(P_2O_7)_3(PO_4)_2$.

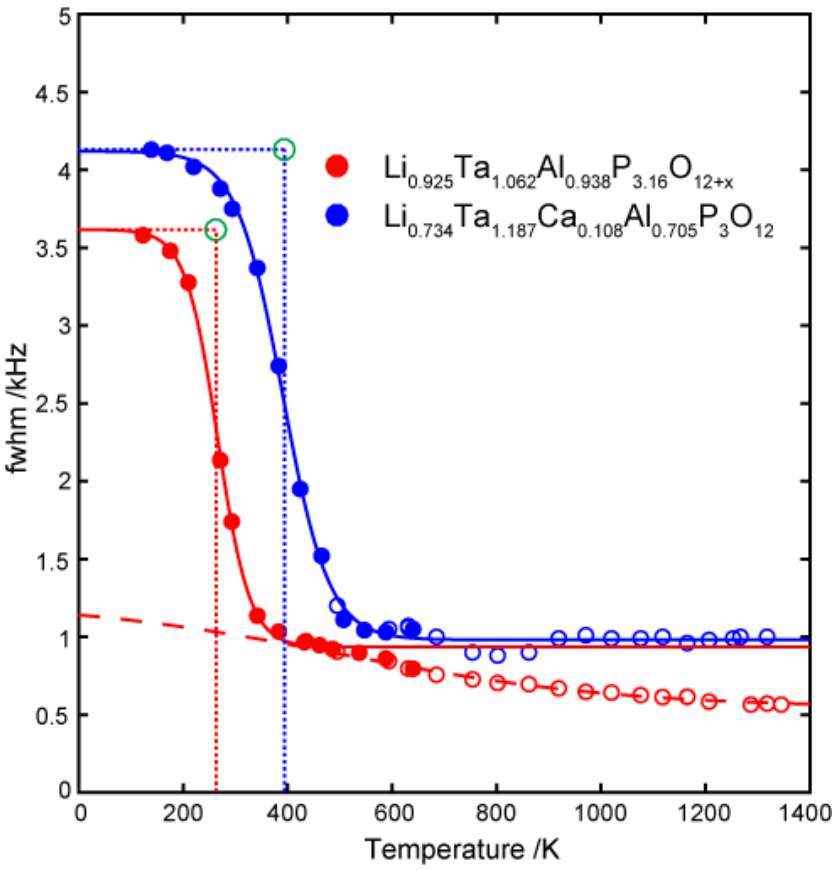

Figure 5.10. Temperature dependence of ^7Li NMR line widths of $Li_{0.925}Ta_{1.062}Al_{0.938}P_{3.16}O_{12+x}$ (red) and $Li_{0.734}Ta_{1.187}Ca_{0.108}Al_{0.705}P_3O_{12}$ (blue)

fitted with sigmoidal regression curves (solid lines). Filled and empty circles refer to data obtained on the MAS probe and the static probe, respectively. The horizontal and vertical red and blue dotted lines give the rigid lattice line width $\Delta\omega_{\text{rigid lattice}}/2\pi$ and the temperature of the inflection point of the regression curve (green circle). The short dashed red and blue lines indicate the onset of Li^+ motion. The long dashed line indicates further narrowing of ^7Li NMR line width, perhaps caused by other samples

5.3.2.2 **NMR Li^+ Dynamics: Spin-Lattice Relaxation**

The temperature dependence of ^7Li spin-lattice relaxation rates (T_1^{-1}) and spin-lattice relaxation rates in the rotating frame ($T_{1\rho}^{-1}$) of $Li_{0.925}Ta_{1.062}Al_{0.938}P_{3.16}O_{12+x}$ and $Li_{0.734}Ta_{1.187}Ca_{0.108}Al_{0.705}P_3O_{12}$ are presented in Figure 5.11.

For $Li_{0.925}Ta_{1.062}Al_{0.938}P_{3.16}O_{12+x}$ at temperatures below 200 K, the T_1^{-1} and $T_{1\rho}^{-1}$ values stay relatively constant, suggesting little Li^+ motion on the scale of the MHz frequency scale. Above 200 K the $T_{1\rho}^{-1}$ values increase, highlighting the material being thermally activated on this time scale. The rates here are indicative of the slow motion regime where $2\pi\nu_0\tau_c$ and $2\pi\nu_1\tau_c >> 1$, where ν_0, ν_1 and τ_c are the ^7Li Larmor frequency, spin-lock frequency and the correlation times of the motion, respectively. In this regime the $T_{1(\rho)}^{-1}$ rates do not probe Li^+ ion translational diffusion[52] but are associated to local processes including hops between local minima and unsuccessful hops to the neighbouring interstitial site. Activation energies E_a on order of 0.16(3) eV and 0.15(1) eV are extracted from T_1^{-1} (200–~500 K) and $T_{1\rho}^{-1}$ (200–~400 K), respectively. These values are similar to what are observed for the best Li^+

conducting oxides[53–57] and are lower than the $Li_{1+x}Al_xTi_{2-x}(PO_4)_3$ series (0 < x < 1.0) studied by Chandran *et al.*[2] in the same motional regime (0.30~0.41 eV). For $Li_{0.734}Ta_{1.187}Ca_{0.108}Al_{0.705}P_3O_{12}$, activation barriers of 0.23(1) and 0.24(2) eV are observed for the same motional regime from 250 K onwards, highlighting the slower Li^+ dynamics in the Ca-doped sample.

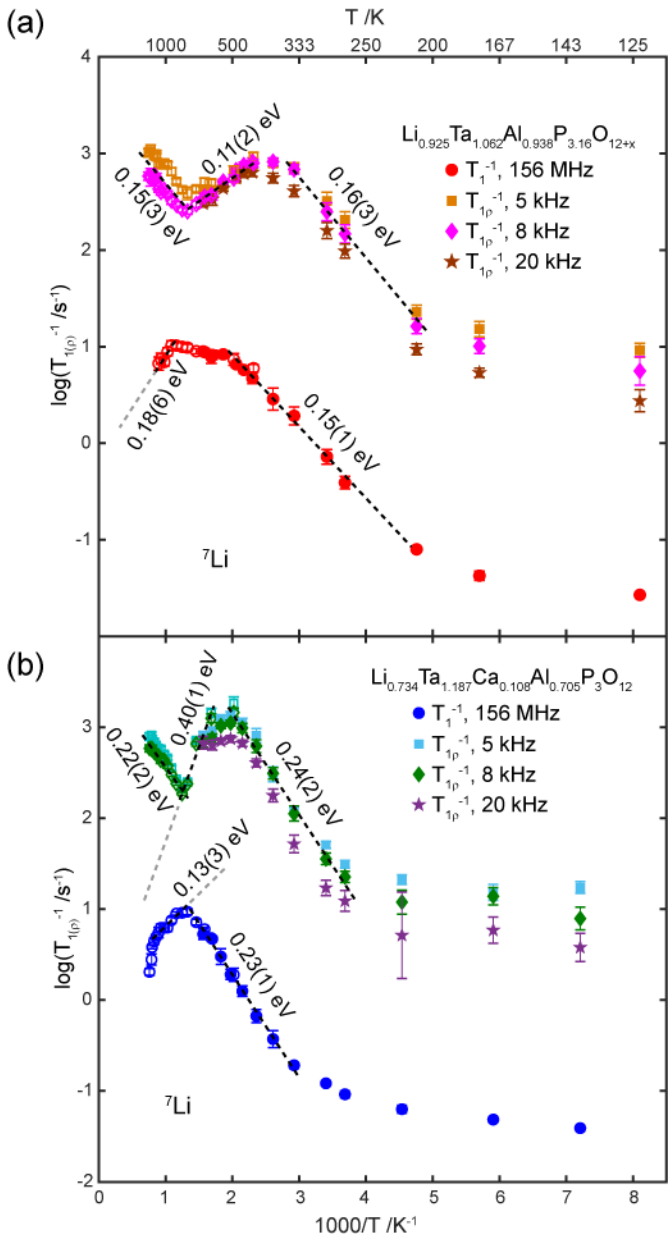

Figure 5.11. Arrhenius plot of ^7Li spin-lattice relaxation (SLR) rates of (a) $Li_{0.925}Ta_{1.062}Al_{0.938}P_{3.16}O_{12+x}$ and (b) $Li_{0.734}Ta_{1.187}Ca_{0.108}Al_{0.705}P_3O_{12}$. SLR rates in the laboratory frame T_1^{-1} (red and blue circle) are obtained at $\nu_0(^7Li)$ = 155.5

and 155.3 MHz on the MAS probe and the static probe, respectively. The SLR rates in the rotating frame ($T_{1\rho}^{-1}$) are obtained at $\nu_1(^7Li)$ = 5 kHz (orange/cyan square), 8 kHz (pink/green diamond) and 20 kHz (brown/purple star). Filled and empty symbols represent data obtained on the MAS probe and on the static probe, respectively. The gap around 1000/T = 1.3 in (b) is arises from the change from MAS to static NMR probe. Black dashed lines refer to the range where activation energies E_a are determined from. Grey dashed lines are extensions of black dashed lines and are guide to the eyes.

As temperature is increased in $Li_{0.925}Ta_{1.062}Al_{0.938}P_{3.16}O_{12+x}$, $T_{1\rho}^{-1}$ maxima is observed at ~400 K. Li^+ ion jump rates τ^{-1} are extracted here on the order of spin-lock frequency ν_1 ($2\pi\nu_1\tau_c \approx 0.5$)[58] yielding values of 6.3(6) x 10^4, 1.0(1) x 10^5 and 2.5(3) x 10^5 s^{-1} at 383, 409 and 435 K, respectively. For $Li_{0.734}Ta_{1.187}Ca_{0.108}Al_{0.705}P_3O_{12}$, the $T_{1\rho}^{-1}$ maxima are found at higher temperatures, highlighting its slower Li^+ dynamics. Values of 6.3(6) x 10^4, 1.0(1) x 10^5 and 2.5(3) x 10^5 at 523, 529 and 541 K are extracted.

At temperatures higher than this maxima, the $T_{1\rho}^{-1}$ rates decrease and the jump rates τ^{-1} relate to translational diffusion of Li^+ ions. A small activation barrier of 0.11(2) eV is extracted between ~420 and ~750 K. The asymmetric nature of these curves are expected as the activation barrier in the slow motion regime deviates from the Bloembergen-Purcell-Pound theory[59] through structural disorder and Coulombic interactions – this is quantified by the model parameter β which ranges between 1 and 2.[58] The lower activation barrier on the high temperature flank, though, is unexpected as the activation barrier here is usually similar or higher than the low temperature flank,[2,53–57] and β becomes

greater than 2; in this case, using the equation $E_{a,low} = (\beta - 1)E_{a,high}$,[58] $\beta \approx 2.5(4)$ for ^{7}Li $T_{1\rho}^{-1}$. One could assume that this is caused by anisotropic thermal expansion of the NASICON framework as observed by the widening of ^{7}Li satellite transitions (Figure 5.7), however no variable temperature PXRD was measured so we cannot observe the expansion direction for this sample directly. If one assumes that the expansion is in the c direction as with other NASICONs in literature,[60–62] this would show an increase in the distance of the main Li diffusion pathway further than that in the a and b directions. As the framework expands, the distance between neighbouring Li sites increases non-uniformly, increasing the residual time τ (time Li resides in a single site) during diffusion compared to structures with uniform structural expansion.

The dimensionality of this diffusion process can be derived from the frequency dependency of $T_{1\rho}^{-1}$ values in this regime. [58] The $T_{1\rho}^{-1}$ rates probed at $\nu_1(^{7}Li)$ = 5, 8 and 20 kHz on the high temperature flanks are independent of frequency, showing characteristics of 3D Li^{+} diffusion, which is in agreement with the crystal structure of NASICONs and other NASICON studies.[1,2,63,64]

The effect of increase in Li^{+} residual time τ for 3D diffusion processes can be observed by using the relationship $J(\omega) \propto \tau$ (see Chapter 2 for details). The resulting spectral density $J(\omega)$ here would be larger than that of a framework with uniform thermal expansion, which would increase the T_1^{-1} values, as observed experimentally (Figure 5.11).

The activation barrier for the high temperature flank in ^{7}Li $T_{1\rho}^{-1}$ data for $Li_{0.734}Ta_{1.187}Ca_{0.108}Al_{0.705}P_3O_{12}$ is found to be 0.40(1) eV, significantly higher compared the undoped composition in the same motional regime, which is consistent with the AC impedance studies.[8] Since the crystal structure is the

same as the undoped composition, one can expect the same diffusion mechanism occurring in this motional regime. The large discrepancy could be caused by the larger ionic radii of Ca^{2+} (1.14 Å) compared to Al^{3+} (0.68 Å) and Ta^{5+} (0.78 Å),[65] which would hinder Li^+ diffusion in the material by both reducing the channel width for the main Li^+ diffusion process (A_1 to A_1 diffusion) and increasing charge repulsion, and also Li^+ trapping effect caused by the negatively charge defects sites with the doping of Ca^{2+} on Al^{3+}/Ta^{5+} sites, which are both observed in first principle studies of Ca doped NASICON $LiZr_2(PO_4)_3$.[66]

As temperature is increased to ~450 K, a change in gradient is observed in T_1^{-1} relaxation rates, with a determined activation barrier of 0.04(1) eV. This value is unrealistically small to consider as the barrier for Li^+ diffusion to occur and could be described as an overlapping of two BPP curves, as observed by París *et al*.[67] and Epp *et al*.,[68] which could include Li^+ ion hopping between A_1 and A_2 sites.

At ~800 K, a change in gradient is observed in ^7Li $T_{1\rho}^{-1}$ values for both $Li_{0.925}Ta_{1.062}Al_{0.938}P_{3.16}O_{12+x}$ and $Li_{0.734}Ta_{1.187}Ca_{0.108}Al_{0.705}P_3O_{12}$ with activation barriers of 0.15(3) and 0.22(2) eV, respectively. These values are the same as what are observed in the same motional regime at lower temperatures and may be caused by local structural changes at high temperature which give additional Li^+ diffusion pathways.

The T_1^{-1} values of $Li_{0.925}Ta_{1.062}Al_{0.938}P_{3.16}O_{12+x}$ and $Li_{0.734}Ta_{1.187}Ca_{0.108}Al_{0.705}P_3O_{12}$ reach maxima between ~750 and ~1100 K. Using the known relationship of $2\pi\nu_0\tau_c \approx 0.62$,[58,69] a Li^+ jump rate τ^{-1} of ~1.6 x 10^9 s^{-1} is obtained at 919 K for $Li_{0.925}Ta_{1.062}Al_{0.938}P_{3.16}O_{12+x}$ and at 754 K for

$Li_{0.734}Ta_{1.187}Ca_{0.108}Al_{0.705}P_3O_{12}$.

On the high temperature flank of the T_1^{-1} maximum, an activation barrier of 0.18(6) eV is obtained for $Li_{0.925}Ta_{1.062}Al_{0.938}P_{3.16}O_{12+x}$. This is within error of the activation barrier of the high temperature flank of the $T_{1\rho}^{-1}$ data of 0.11(2) eV, suggesting that we potentially probe the same 3D diffusion pathway. An activation barrier of 0.13(3) eV is extracted for $Li_{0.734}Ta_{1.187}Ca_{0.108}Al_{0.705}P_3O_{12}$, which, though within error, is lower than what is observed for $Li_{0.925}Ta_{1.062}Al_{0.938}P_{3.16}O_{12+x}$ in the similar temperature range. This could possibly be caused by the thermal expansion of the material increasing the width of the diffusion channel wide enough that Ca-doping does not affect Li^+ diffusion.[28,46]

5.3.2.3 **NMR Jump Rates τ^{-1}**

The jump rates τ^{-1} extracted from ^{7}Li line narrowing experiments (Figure 5.7 and Figure 5.9) and relaxometry (Figure 5.11) are plotted against reciprocal temperature in Figure 5.12 with the Arrhenius formula $\tau^{-1} = \tau_0^{-1} \exp(E_a/RT)$, where τ_0^{-1} is the pre-exponential factor. The activation barrier of the two methods are significantly higher than the barriers found in the SLR plot (Figure 5.11). For the same Li^+ diffusive process, we would expect the same activation barrier observed in the SLR plot, however this is not the case for these materials. In the study of $Li_{12}Si_7$ by Kuhn *et al*. where a similar discrepancy is observed,[45] the authors report that the difference arises from strong anisotropic diffusion processes. This is in agreement ^{7}Li NMR relaxometry and the NMR studies performed by Emery *et al*.[28,46] The significantly higher activation barrier in the Ca-doped sample, however, could

also be caused by the larger ionic radii of Ca^{2+}, as discussed in the SLR section.

The pre-exponential factor τ_0^{-1} is found to be ~3 x 10^{12} and ~2 x 10^{19} s^{-1} for $Li_{0.925}Ta_{1.062}Al_{0.938}P_{3.16}O_{12+x}$ and $Li_{0.734}Ta_{1.187}Ca_{0.108}Al_{0.705}P_3O_{12}$, respectively, which are on the order of magnitude for Li ion conductors (see Chapter 2). Although we do not have any calculated photon frequencies to compare to, the pre-exponential factor is significantly higher for $Li_{0.734}Ta_{1.187}Ca_{0.108}Al_{0.705}P_3O_{12}$ when compared to $Li_{1.5}Al_{0.5}Ti_{1.5}(PO_4)_3$ (3 x 10^{11} and 1 x 10^{10} s^{-1})[68] and other Li^+ ion conductors.[53,70,71] The high pre-exponential factor in $Li_{0.734}Ta_{1.187}Ca_{0.108}Al_{0.705}P_3O_{12}$ may be high due to the addition of Ca^{2+} blocking the diffusion pathways along with the anisotropic nature of the Li^+ diffusion.

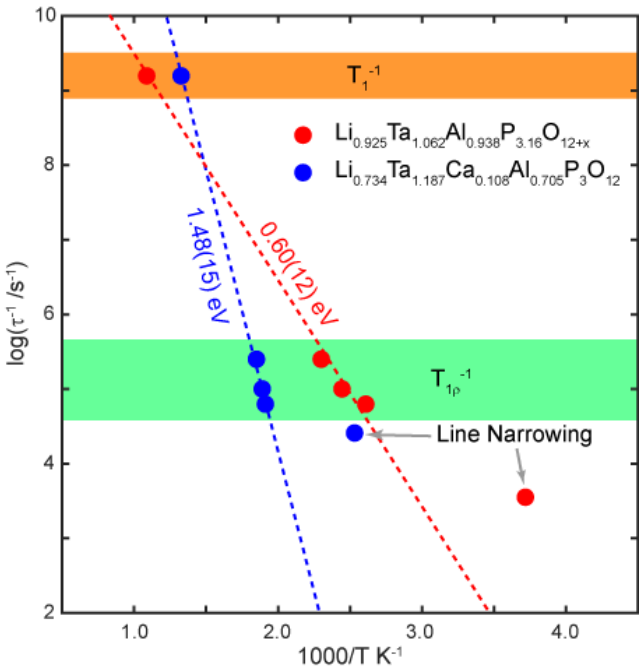

Figure 5.12. Arrhenius plot of ^7Li jump rate τ^{-1} obtained from ^7Li line narrowing experiments (Figure 5.7 and Figure 5.9) and relaxometry data (Figure 5.11). Vertical and horizontal error bars are within the symbol.

5.3.2.4 ^{27}Al NMR After Heating

After the samples were heated to ~1100 K in the static laser heated NMR probe, they were cooled down to room temperature with a fast flow of N_2 and Ar gas flow (see Experimental section), essentially "quenching" the material.[72] Comparison of the ^{27}Al MAS NMR spectra of $Li_{0.925}Ta_{1.062}Al_{0.938}P_{3.16}O_{12+x}$ recorded before and after heating is shown in Figure 5.13. We observe that the main NASICON phase is intact, however, both quartz $AlPO_4$ and $Li_9Al_3(P_2O_7)_3(PO_4)_2$ phases are not observed after heating. The quartz $AlPO_4$ phase has most likely underwent phase transition to the cristobalite and tridymite $AlPO_4$ phases.[73] The $Li_9Al_3(P_2O_7)_3(PO_4)_2$ phase may have melted and become amorphous due to the rapid quenching, and is therefore too broad to observe.

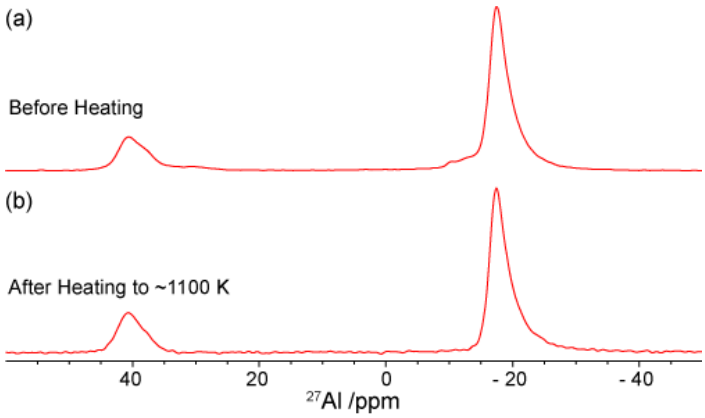

Figure 5.13. ^{27}Al MAS NMR spectra of $Li_{0.925}Ta_{1.062}Al_{0.938}P_{3.16}O_{12+x}$ before heating (a) and after heating to ~1100 K (b) recorded at 9.4 T and at MAS of 12.5 kHz.

5.4 Conclusions

Through the use of multinuclear solid state NMR spectroscopy, we identify the main NASICON phases $Li_{0.925}Ta_{1.062}Al_{0.938}P_{3.16}O_{12+x}$ and

$Li_{0.734}Ta_{1.187}Ca_{0.108}Al_{0.705}P_3O_{12}$ as well as a range of impurities (cristobalite $AlPO_4$, quartz $AlPO_4$, tridymite $AlPO_4$, $Li_4P_2O_7$, $Li_9Al_3(P_2O_7)_3(PO_4)_2$ and $Li_{9-n}Al_{3-n}Ta_n(P_2O_7)_3(PO_4)_2$, Table 5.2). The large distribution of quadrupolar interactions seen in the ^{27}Al NMR in the octahedral Al region in $Li_{0.925}Ta_{1.062}Al_{0.938}P_{3.16}O_{12+x}$ was assigned to the distorted NASICON framework caused by the distorted $[PO_4]^{3-}$ tetrahedra caused bonded to different amounts of Ta^{5+}, consistent with literature findings using multiple analytical techniques.

The main NASICON phase was found to be intact even after measuring Li^+ dynamics at extreme temperatures of up to 1350 K. The undoped $Li_{0.925}Ta_{1.062}Al_{0.938}P_{3.16}O_{12+x}$ showed significantly better Li^+ ion conductivity compared to the Ca-doped sample, which is consistent with impedance spectroscopy.[8] The difference in activation barrier between the ^7Li relaxometry and Li^+ jump rate Arrhenius plot is found to be consistent with the anisotropic nature of Li^+ diffusion in NASICON type materials.

The aim of obtaining higher Li^+ conductivity by doping with Ca^{2+} was not achieved, with the Li^+ dynamics of the doped sample being consistently lower than that of the undoped composition. Reasons for this could be hypothesised as the larger ionic radii of Ca^{2+} increasing the size of the MO_6 octahedra which in turn in decreases the size of Li^+ diffusion channel, hindering Li^+ diffusion through the material, Li^+ trapping effect by Ca^{2+}, or the lower Li content of the sample.

5.5 References

1 D. Rettenwander, A. Welzl, S. Pristat, F. Tietz, S. Taibl, G. J.

Redhammer and J. Fleig, *J. Mater. Chem. A*, 2016, **4**, 1506–1513.

2 C. Vinod Chandran, S. Pristat, E. Witt, F. Tietz and P. Heitjans, *J. Phys. Chem. C*, 2016, **120**, 8436–8442.

3 J. C. Bachman, S. Muy, A. Grimaud, H.-H. Chang, N. Pour, S. F. Lux, O. Paschos, F. Maglia, S. Lupart, P. Lamp, L. Giordano and Y. Shao-Horn, *Chem. Rev.*, 2016, **116**, 140–162.

4 A. Manthiram, X. Yu and S. Wang, *Nat. Rev. Mater.*, 2017, **2**, 1–16.

5 V. Thangadurai, A. K. Shukla and J. Gopalakrishnan, *J. Mater. Chem.*, 1999, **9**, 739–741.

6 J. G. Kim, B. Son, S. Mukherjee, N. Schuppert, A. Bates, O. Kwon, M. J. Choi, H. Y. Chung and S. Park, *J. Power Sources*, 2015, **282**, 299–322.

7 Y. Wang, W. D. Richards, S. P. Ong, L. J. Miara, J. C. Kim, Y. Mo and G. Ceder, *Nat. Mater.*, 2015, **14**, 1026–1031.

8 L. Enciso-Maldonado, University of Liverpool, 2017.

9 L. Frydman and J. S. Harwood, *J. Am. Chem. Soc.*, 1995, **117**, 5367–5368.

10 A. Medek, J. S. Harwood and L. Frydman, *J. Am. Chem. Soc.*, 1995, **117**, 12779–12787.

11 J.-P. Amoureux, C. Fernandez and S. Steuernagel, *J. Magn. Reson. Ser. A*, 1996, **123**, 116–118.

12 G. Le Caër and R. A. Brand, *J. Phys. Condens. Matter*, 1998, **10**, 10715–10774.

13 J.-B. d'Espinose de Lacaillerie, C. Fretigny and D. Massiot, *J. Magn. Reson.*, 2008, **192**, 244–251.

14 G. Le Caër, B. Bureau and D. Massiot, *J. Phys. Condens. Matter*, 2010,

22, 065402.

15 G. Czjzek, J. Fink, F. Götz, H. Schmidt, J. M. D. Coey, J. P. Rebouillat and a. Liénard, *Phys. Rev. B*, 1981, **23**, 2513–2530.

16 D. Massiot, F. Fayon, M. Capron, I. King, S. Le Calvé, B. Alonso, J.-O. Durand, B. Bujoli, Z. Gan and G. Hoatson, *Magn. Reson. Chem.*, 2002, **40**, 70–76.

17 V. Lacassagne, C. Bessada, P. Florian, S. Bouvet, B. Ollivier, J.-P. Coutures and D. Massiot, *J. Phys. Chem. B*, 2002, **106**, 1862–1868.

18 V. Lacassagne, C. Bessada, B. Ollivier, D. Massiot, P. Florian and J.-P. Coutures, *Comptes Rendus l'Académie des Sci. - Ser. IIB*, 1997, **325**, 91–98.

19 A. Bielecki and D. P. Burum, *J. Magn. Reson. Ser. A*, 1995, **116**, 215–220.

20 P. A. Beckmann and C. Dybowski, *J. Magn. Reson.*, 2000, **146**, 379–380.

21 K. D. Becker, *J. Chem. Phys.*, 1978, **68**, 3785–3793.

22 J. Wu, N. Kim and J. F. Stebbins, *Solid State Nucl. Magn. Reson.*, 2011, **40**, 45–50.

23 M. Forsyth, S. Wong, K. M. Nairn, A. S. Best, P. J. Newman and D. R. MacFarlane, *Solid State Ionics*, 1999, **124**, 213–219.

24 P. Maldonado-Manso, M. C. Martín-Sedeño, S. Bruque, J. Sanz and E. R. Losilla, *Solid State Ionics*, 2007, **178**, 43–52.

25 C. Schröder, J. Ren, A. C. M. Rodrigues and H. Eckert, *J. Phys. Chem. C*, 2014, **118**, 9400–9411.

26 Z. Liu, S. Venkatachalam and L. van Wüllen, *Solid State Ionics*, 2015,

276, 47–55.

27 M. Smith, *Prog. Nucl. Magn. Reson. Spectrosc.*, 1999, **34**, 159–201.

28 J. Emery, T. Šalkus, A. Abramova, M. Barré and A. F. Orliukas, *J. Phys. Chem. C*, 2016, **120**, 26173–26186.

29 S. Sukenaga, P. Florian, K. Kanehashi, H. Shibata, N. Saito, K. Nakashima and D. Massiot, *J. Phys. Chem. Lett.*, 2017, **8**, 2274–2279.

30 L. Baggetto, V. Sarou-Kanian, P. Florian, A. N. Gleizes, D. Massiot and C. Vahlas, *Phys. Chem. Chem. Phys.*, 2017, **19**, 8101–8110.

31 S. Poisson, F. d'Yvoire, NGuyen-Huy-Dung, E. Bretey and P. Berthet, *J. Solid State Chem.*, 1998, **138**, 32–40.

32 D. Massiot, F. Fayon, M. Capron, I. King, S. Le Calvé, B. Alonso, J.-O. Durand, B. Bujoli, Z. Gan and G. Hoatson, *Magn. Reson. Chem.*, 2002, **40**, 70–76.

33 C. Schröder, J. Ren, A. C. M. Rodrigues and H. Eckert, *J. Phys. Chem. C*, 2014, **118**, 9400–9411.

34 Y.-X. Xiang, G. Zheng, G. Zhong, D. Wang, R. Fu and Y. Yang, *Solid State Ionics*, 2018, **318**, 19–26.

35 D. Müller, E. Jahn, G. Ladwig and U. Haubenreisser, *Chem. Phys. Lett.*, 1984, **109**, 332–336.

36 K. T. Mueller, J. H. Baltisberger, E. W. Wooten and A. Pines, *Isotropic chemical shifts and quadrupolar parameters for oxygen-17 using dynamic-angle spinning NMR*, 1992, vol. 96.

37 J. H. Baltisberger, S. L. Gann, A. Pines, E. W. Wooten, T. H. Chang and K. T. Mueller, *87Rb Dynamic-Angle Spinning NMR Spectroscopy of Inorganic Rubidium Salts*, 1992, vol. 114.

38 K. Arbi, S. Mandal, J. M. Rojo and J. Sanz, *Chem. Mater.*, 2002, **14**, 1091–1097.

39 K. Arbi, J. M. Rojo and J. Sanz, *J. Eur. Ceram. Soc.*, 2007, **27**, 4215–4218.

40 V. I. Voronin, E. A. Sherstobitova, V. A. Blatov and G. S. Shekhtman, *J. Solid State Chem.*, 2014, **211**, 170–175.

41 R. Kahlaoui, K. Arbi, I. Sobrados, R. Jimenez, J. Sanz and R. Ternane, *Inorg. Chem.*, 2017, **56**, 1216–1224.

42 K. J. D. MacKenzie and M. E. Smith, *Multinuclear Solid-State Nuclear Magnetic Resonance of Inorganic Materials*, Elsevier, Oxford, 2002.

43 Z. Xu and J. F. Stebbins, *Science (80-.).*, 1995, **270**, 1332–1334.

44 Z. Xu and J. F. Stebbins, *Solid State Nucl. Magn. Reson.*, 1995, **5**, 103–112.

45 A. Kuhn, P. Sreeraj, R. Pöttgen, H. D. Wiemhöfer, M. Wilkening and P. Heitjans, *J. Am. Chem. Soc.*, 2011, **133**, 11018–11021.

46 J. Emery, T. Šalkus and M. Barré, *J. Phys. Chem. C*, 2016, **120**, 26235–26243.

47 T. Šalkus, E. Kazakevičius, A. Kežionis, A. Dindune, Z. Kanepe, J. Ronis, J. Emery, A. Boulant, O. Bohnke and A. F. Orliukas, *J. Phys. Condens. Matter*, 2009, **21**, 185502.

48 D. Petit, P. Colomban, G. Collin and J. P. Boilot, *Mater. Res. Bull.*, 1986, **21**, 365–371.

49 D. T. Qui, S. Hamdoune, J. L. Soubeyroux and E. Prince, *J. Solid State Chem.*, 1988, **72**, 309–315.

50 M. Catti, A. Comotti and S. Di Blas, *Chem. Mater.*, 2003, **15**, 1628–1632.

51 M. Monchak, T. Hupfer, A. Senyshyn, H. Boysen, D. Chernyshov, T. Hansen, K. G. Schell, E. C. Bucharsky, M. J. Hoffmann and H. Ehrenberg, *Inorg. Chem.*, 2016, **55**, 2941–2945.

52 R. Böhmer, K. R. Jeffrey and M. Vogel, *Prog. Nucl. Magn. Reson. Spectrosc.*, 2007, **50**, 87–174.

53 J. Emery, J. . Buzare, O. Bohnke and J. . Fourquet, *Solid State Ionics*, 1997, **99**, 41–51.

54 O. Bohnke, J. Emery and J. L. Fourquet, *Solid State Ionics*, 2003, **158**, 119–132.

55 H. Buschmann, J. Dölle, S. Berendts, A. Kuhn, P. Bottke, M. Wilkening, P. Heitjans, A. Senyshyn, H. Ehrenberg, A. Lotnyk, V. Duppel, L. Kienle and J. Janek, *Phys. Chem. Chem. Phys.*, 2011, **13**, 19378.

56 W. Bucheli, K. Arbi, J. Sanz, D. Nuzhnyy, S. Kamba, A. Várez and R. Jimenez, *Phys. Chem. Chem. Phys.*, 2014, **16**, 15346–15354.

57 A. B. Santibáñez-Mendieta, C. Didier, K. K. Inglis, A. J. Corkett, M. J. Pitcher, M. Zanella, J. F. Shin, L. M. Daniels, A. Rakhmatullin, M. Li, M. S. Dyer, J. B. Claridge, F. Blanc and M. J. Rosseinsky, *Chem. Mater.*, 2016, **28**, 7833–7851.

58 P. Heitjans, A. Schirmer and S. Indris, *NMR and β-NMR Studies of Diffusion in Interface-Dominated and Disordered Solids*, Springer-Verlag Berlin Heidelberg, The Netherlands, 2005.

59 N. Bloembergen, E. M. Purcell and R. V Pound, *Phys. Rev.*, 1948, **73**, 679–712.

60 D. T. Qui, J. J. Capponi, M. Gondrand, M. Saïb, J. C. Joubert and R. D. Shannon, *Solid State Ionics*, 1981, **3**–**4**, 219–222.

61 F. E. Mouahid, M. Bettach, M. Zahir, P. Maldonado-Manso, S. Bruque, E. R. Losilla and M. A. G. Aranda, *J. Mater. Chem.*, 2000, **10**, 2748–2757.

62 D. Safanama, N. Sharma, R. P. Rao, H. E. A. Brand and S. Adams, *J. Mater. Chem. A*, 2016, **4**, 7718–7726.

63 H. Aono, E. Sugimoto, Y. Sadaoka, N. Imanaka and G.-Y. Adachi, *J. Electrochem. Soc.*, 1990, **137**, 1023–1027.

64 P. Knauth, *Solid State Ionics*, 2009, **180**, 911–916.

65 R. D. Shannon, *Acta Crystallogr. Sect. A*, 1976, **A32**, 751–767.

66 Y. Noda, K. Nakano, M. Otake, R. Kobayashi, M. Kotobuki, L. Lu and M. Nakayama, 2018, **6**, 60702.

67 M. A. París, A. Martínez-Juárez, J. M. Rojo and J. Sanz, *J. Phys. Condens. Matter*, 1996, **8**, 5355–5366.

68 V. Epp, Q. Ma, E.-M. Hammer, F. Tietz and M. Wilkening, *Phys. Chem. Chem. Phys.*, 2015, **17**, 32115–32121.

69 A. Abragam, *The Principles of Nuclear Magnetism*, Oxford University Press, Oxford, 1961.

70 V. Epp, O. Gün, H.-J. Deiseroth and M. Wilkening, *Phys. Chem. Chem. Phys.*, 2013, **15**, 7123–7132.

71 A. Kuhn, V. Duppel and B. V. Lotsch, *Energy Environ. Sci.*, 2013, **6**, 3548.

72 K. K. Inglis, J. P. Corley, P. Florian, J. Cabana, R. D. Bayliss and F. Blanc, *Chem. Mater.*, 2016, **28**, 3850–3861.

73 W. R. Beck, *J. Am. Ceram. Soc.*, 1949, **32**, 147–151.

6. New Sulfide Li^+ Ion Conductors – $Li_{4.4}Al_{0.4}Ge_{0.6}S_4$ and $Li_{4.4}Al_{0.4}Sn_{0.6}S_4$[1]

Sulfide based conductors have higher ionic conductivity compared to their oxide counterparts largely due to the larger ionic radii and higher polarizability characteristics of the S^{2-} ions,[2–5] which increases channel size and reduces Li–framework interaction. These advantages give sulfide based solid Li^+ ion conductors competing conductivities to liquid electrolytes – e.g.; $Li_{10}GeP_2S_{12}$ by Kanno *et al*.[6] and its related compounds[7,8] – with room temperature conductivities of ~1 x 10^{-2} S cm^{-1}. These advantages also come with a disadvantage, however, as these sulfide based conductors react with moisture to form H_2S and therefore must be handled in inert atmospheres,[9] whereas oxide based conductors are more chemically stable. The lower redox stability of the sulfide anion is also an issue (see Chapter 3), as $Li_{10}GeP_2S_{12}$ reduces into Li_3P, Li_2S, $Li_{15}Ge_4$ and Ge, and the argyrodite Li_6PS_5Cl (Chapter 3) reduces into Li_3P, Li_2S and LiCl when in contact with Li metal.[10,11] In contrast, $Li_{11}AlP_2S_{12}$, analogous in structure to $Li_{10}GeP_2S_{12}$, has been reported to be stable against Li metal, with a decrease in room temperature conductivity to 8.02 x 10^{-4} S cm^{-1}.[12]

Li_5AlS_4 is a lithium containing metal sulfide of interest as it consists of Li and Al occupying the tetrahedral site and Li on the “octahedral” layer, which consists of two distinct Li sites – a near-regular octahedron and a five-coordinate Li site which is displaced from the centre of the six sulfides.[13] All the sites are fully occupied giving this material a low conductivity of 10^{-9} S cm^{-1}.[14] One approach to improve conductivity is to introduce multiple species on

the tetrahedral site to control the Li distribution and diffusion pathways. Combination of other lithium-containing metal sufides, such as Li_4GeS_4 and Li_4SnS_4, that consist of Li occupying a mixture of the tetrahedral and octahedral sites[14,15] are used to improve Li^+ conductivity as studied by Kanno *et al*.[2,14] The authors investigated the Li_5AlS_4-Li_4SiS_4 and Li_5GaS_4-Li_4GeS_4 thio-LISICON systems and report a new orthorhombic phase with improved conductivity, suggesting the existence of a new structural family that has not been reported, however no atomic coordinates of this was reported.

Therefore the Li_5AlS_4-Li_4GeS_4 system was investigated synthetically, reporting the lithium-containing metal sulfides $Li_{4.4}M_{0.4}M'_{0.6}S_4$ (*M*= Al^{3+}, Ga^{3+} and *M'*= Ge^{4+}, Sn^{4+}) phases and their crystal structures were refined from powder X-ray and neutron diffraction data (Figure 6.1a).[1] The crystal structure found all phases isostructural, containing isolated MS_4 and $M'S_4$ tetrahedral layers on the same site, with the tetrahedrons facing opposite directions along the layer. The S^{2-} is corner shared with two tetrahedral and one octahedral Li site. The two tetrahedral Li, labelled Li1 and Li2, are face shared and never simultaneously occupied, complemented by their combined occupancy of 0.992(6). The octahedral Li labelled Li3, has an occupancy of 0.441, highlighting the presence of Li^+ vacancies along the octahedral layer, showing promising prospects for Li diffusion.

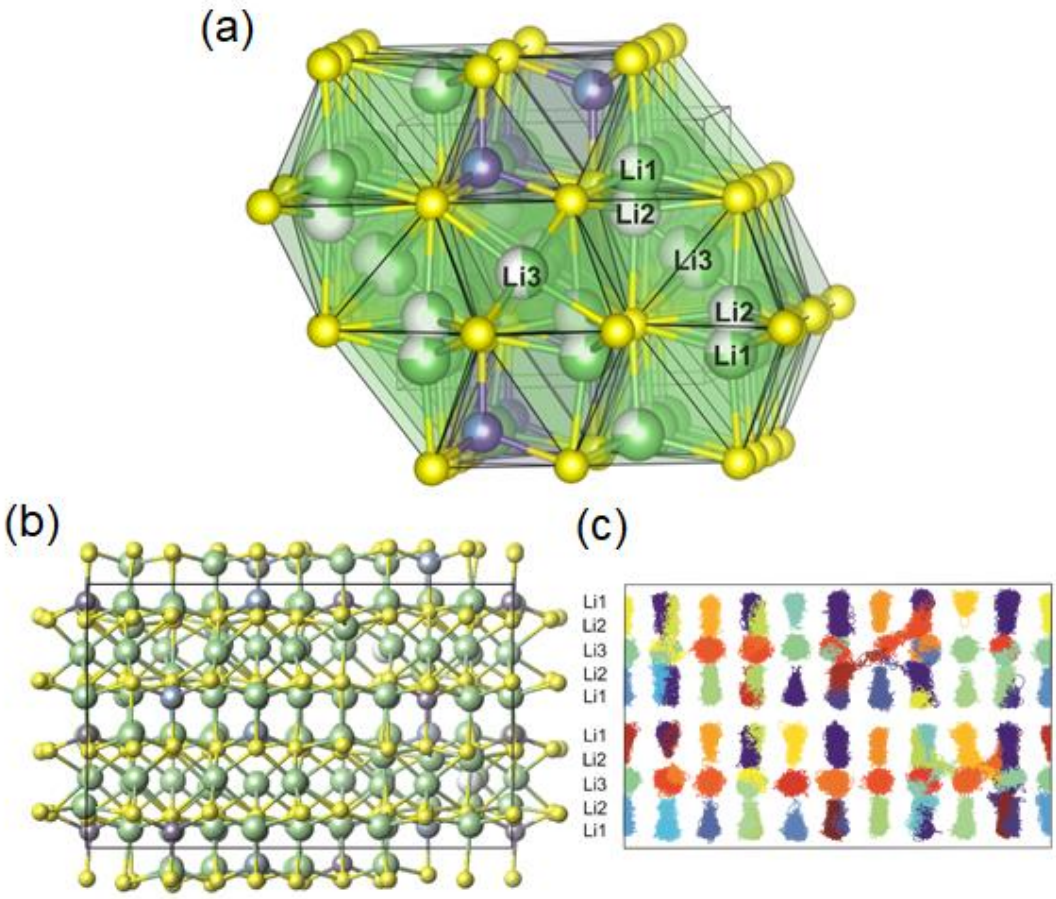

Figure 6.1. (a) Crystal structure of $Li_{4.4}Al_{0.4}Ge_{0.6}S_4$ determined at 10 K.[1] Atom colour: Li (green), Al (blue), Ge (purple), S (yellow). Pie charts denote occupancy of the site. (b) Structure of supercell used for AIMD. (c) Changes in Li positions during AIMD runs.

Lithium ion transport of the phases $Li_{4.4}Al_{0.4}Ge_{0.6}S_4$ and $Li_{4.4}Al_{0.4}Sn_{0.6}S_4$ were investigated by AC impedance spectroscopy and *ab initio* molecular dynamics (AIMD).[1] Impedance experiments showed the faster Li^+ dynamics in $Li_{4.4}Al_{0.4}Ge_{0.6}S_4$ compared to $Li_{4.4}Al_{0.4}Sn_{0.6}S_4$ with room temperature conductivity of 4.3(3) x 10^{-5} and 4.3(9) x 10^{-6} S cm^{-1} and activation barriers of 0.38(1) and 0.42(1) eV, respectively. AIMD runs identified Li^+ transport between Li2 and Li3 sites along the octahedral layer, with no transport along

the Li1/AlS_4/GeS_4 containing tetrahedral layer (Figure 6.1c). This incidentally results in a two dimensional Li^+ diffusive motion along the octahedral layer and the energy barrier was determined to be 0.17 eV. The resulting two-dimensional diffusion pathways connected to the vacancy order imposed by the different tetrahedral non-lithium species in the newly observed structure. The activation barriers discrepancy between impedance spectroscopy and AIMD show that they may probe different Li diffusion processes, and would require other experimental approaches, such as variable temperature solid-state NMR spectroscopy, to understand the material further.

In this chapter, solid-state NMR studies of $Li_{4.4}Al_{0.4}Ge_{0.6}S_4$ and $Li_{4.4}Al_{0.4}Sn_{0.6}S_4$ are discussed.[1] Local structural information of this new structure is investigated using ^6Li, ^{27}Al and ^{119}Sn MAS NMR. Li^+ dynamics are investigated with variable temperature ^7Li static NMR to determine the activation barrier for Li^+ diffusion and its dimensionality. NMR data are compared to the crystal structure determined by diffraction experiments and AC impedance spectroscopy and AIMD approaches.

6.1 Experimental

^6Li, ^{27}Al and ^{119}Sn magic angle spinning (MAS) NMR spectra were recorded using a 4 mm HXY MAS Probe in double resonance mode on a 9.4 T Bruker DSX solid-state NMR spectrometer. All samples were packed in HRMAS inserts in a He glove box to eliminate air exposure. All data acquisitions were quantitative using recycle delays longer than 5 times the spin-lattice relaxation times T_1 unless noted otherwise. ^6Li NMR data were obtained with a pulse of length 4 μs at a radio-frequency (rf) field amplitude of

62.5 kHz and at a MAS rate of ν_r = 10 kHz. ^{27}Al NMR data were all obtained with a short 30^o pulse flip angle of pulse length 0.33 μs at rf amplitude of $\omega_1/2\pi(^{27}Al)$ = 83 kHz and at a MAS rate of ν_r = 8 kHz. Excitation and reconversion pulses for the two dimensional z-filtered triple quantum MAS (3QMAS)[16–18] experiments were performed at rf amplitudes of $\omega_1/2\pi(^{27}Al)$ = 100 kHz and 833 Hz for the soft pulse, respectively. The ^{119}Sn NMR spectrum was obtained with a 90^o pulse of pulse length 3 μs at rf amplitude of $\omega_1/2\pi(^{119}Sn)$ = 83 kHz and at a MAS rate of ν_r = 10 kHz. ^{27}Al and ^{6}Li shifts were referenced to 0.1 M $Al(NO_3)_3$ in H_2O and 10 M in LiCl in D_2O at 0 ppm, respectively. ^{119}Sn shifts were referenced to SnO_2 at -604.3 ppm (equivalent to trimethyltin at 0.0 ppm).[19]

Variable temperature ^{7}Li NMR experiments were recorded on a 4 mm HXY MAS probe in double resonance mode (between 110 K – 400 K) and a 4 mm HX High Temperature MAS Probe (above room temperature), both on a 9.4 T Bruker Avance III HD spectrometer under static conditions with the X channel tuned to ^{7}Li at $\omega_0/2\pi(^7Li)$ = 156 MHz. All samples were flame sealed in Pyrex inserts under He atmosphere. All ^{7}Li NMR spectra were obtained with a hard 90^o pulse of 1.5 μs at rf amplitude of $\omega_1/2\pi(^7Li)$ = 83 kHz. Spin-lattice relaxation rates in the laboratory frame (T_1^{-1}) were obtained using a saturation recovery pulse sequence and the data was fitted to a stretch exponential function of form $1 - \exp[-(\tau/T_1)^{\alpha}]$ where τ are the variable delays and α is the stretch exponential (values between 0.3 and 1) . Spin-lattice relaxation rates in the rotating frame ($T_{1\rho}^{-1}$) were recorded using a standard spin-lock pulse sequence at frequencies of $\omega_1/2\pi(^7Li)$ = 20, 33 and 50 kHz and data were fitted to a stretch exponential function of form $\exp[-(\tau/T_{1\rho}^{-1})^{\beta}]$ where β values are

between 0.5 and 1. Temperature calibrations were performed using the chemical shift thermometers $Pb(NO_3)_2$ using ^{207}Pb NMR and CuI and CuBr using ^{63}Cu NMR.[20–23] ^{7}Li NMR shifts were referenced to 10 M LiCl in D_2O at 0 ppm.

6.2 Results

6.2.1 NMR: ^{6}Li, ^{27}Al and ^{119}Sn

^{6}Li MAS NMR spectra measured at room temperature for $Li_{4.4}Al_{0.4}Ge_{0.6}S_4$ and $Li_{4.4}Al_{0.4}Sn_{0.6}S_4$ are presented in Figure 6.2a. The ^{6}Li NMR spectrum of $Li_{4.4}Al_{0.4}Sn_{0.6}S_4$ (Figure 6.2a, red) displays three overlapping resonances – a sharp peak at ~1.1 ppm, a broad resonance at ~1.1 ppm and a shoulder at ~1.3 ppm in a 1.3(1):1:1.1(1) ratio, representing three Li sites in the structure, where two are likely to have the same coordination number. The diffraction derived crystal structure observes 3 Li sites – labelled Li1, Li2 and Li3. The three NMR resonances are respectively assigned to the tetrahedral Li1, Li2 and octahedral Li3 based on the 1.4:1:1.1 ratio obtained from the sites occupancies.

Although $Li_{4.4}Al_{0.4}Ge_{0.6}S_4$ and $Li_{4.4}Al_{0.4}Sn_{0.6}S_4$ are isostructural, the ^{6}Li NMR spectrum of the former phase only shows a single narrow peak at ~1.2 ppm (with a full width at half maximum fwhm of ~30 Hz). It is likely that this arises from fast motional narrowing on the NMR time scale at room temperature of the ^{6}Li NMR resonances due to the higher Li^+ conductivity of $Li_{4.4}Al_{0.4}Ge_{0.6}S_4$ *vs.* $Li_{4.4}Al_{0.4}Sn_{0.6}S_4$ as revealed by the Li^+ dynamics probed (see below), preventing the resolution of the three individual Li1, Li2, and Li3 sites. The presence of low-level lithium-containing impurities seen by

crystallography[1] are not observed clearly in the NMR spectra of either compound. This is likely due to a combination of their small phase fractions (<1 mol%) and the limited range of the ^{6}Li chemical shifts (tetrahedral Li in $LiAlS_2$ with an estimated shift around 1 ppm).[24]

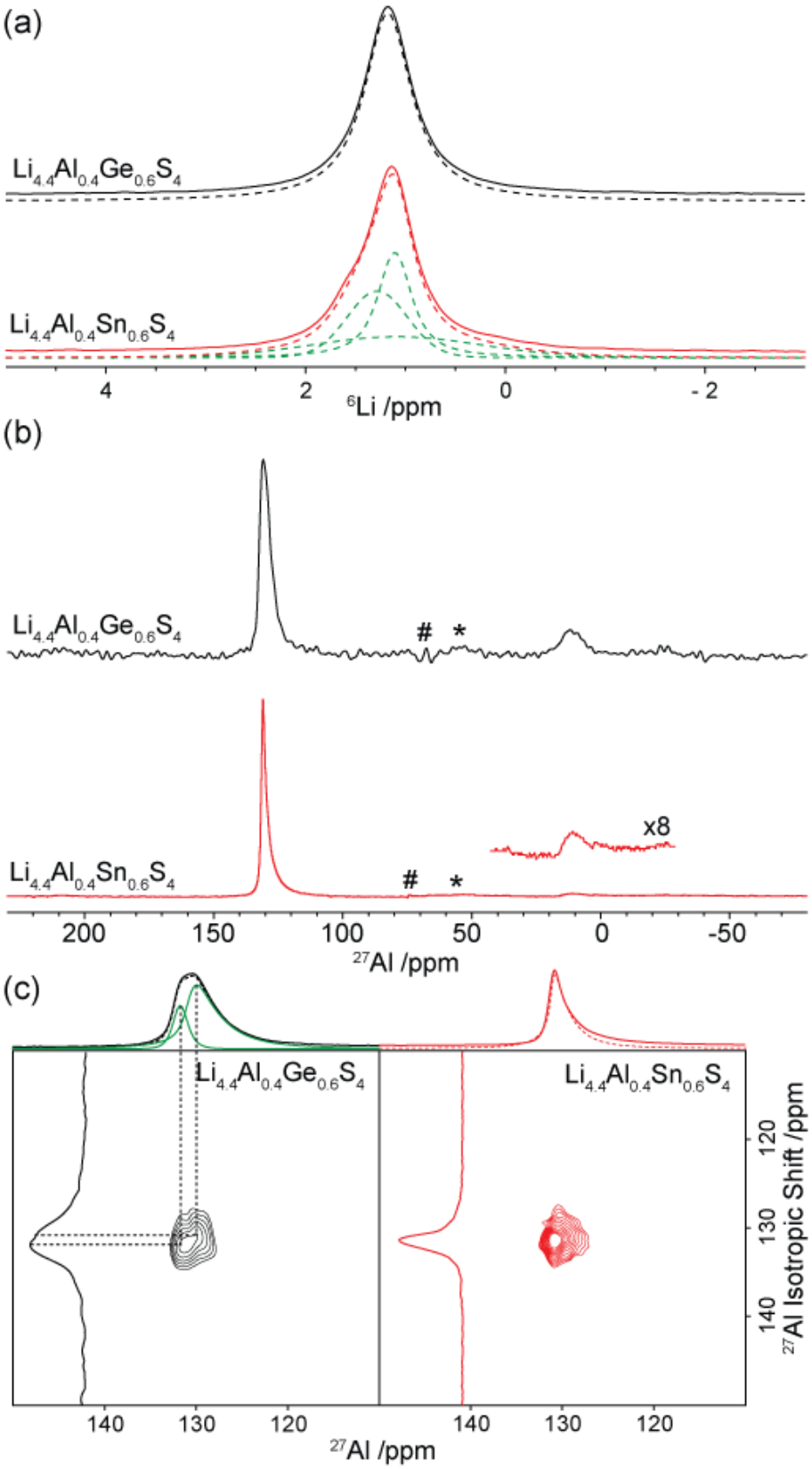

Figure 6.2. (a) ^{6}Li MAS NMR spectra of $Li_{4.4}Al_{0.4}Ge_{0.6}S_4$ (black) (synthesised using commercial Li_2S and Ge) and $Li_{4.4}Al_{0.4}Sn_{0.6}S_4$ (red) (synthesised purified reagents) at MAS rate of ν_r = 10 kHz. The black dotted line represents a single

line shape simulation. Red dotted lines represent the sum of simulated peaks (green dotted lines). Simulation for ^{6}Li NMR spectra were done using the SOLA package in Bruker TopSpin®. (b) ^{27}Al MAS NMR spectra. The small peak at ~15 ppm corresponds to a small amount of α-Al_2O_3 impurity. Note: The ^{27}Al spectrum for $Li_{4.4}Al_{0.4}Sn_{0.6}S_4$ (red) is not recorded at $5xT_1$ of the phase at ~15 ppm. (c) ^{27}Al 3QMAS NMR of $Li_{4.4}Al_{0.4}Ge_{0.6}S_4$ and $Li_{4.4}Al_{0.4}Sn_{0.6}S_4$ at MAS frequency of ν_r = 8 kHz. Top spectra: 30^o flip angle MAS NMR spectra. Solid black and red lines denote the experimental spectra, dotted lines are the sum of the simulated spectra (solid green lines). The fits for ^{27}Al NMR data were performed using the Czjzek function in dmfit using the CzSimple model (see Chapter 2 for details about the model). Asterisks (*) denote spinning sidebands. Hash sign (#) denote centre spike from carrier frequency.

The room temperature ^{27}Al MAS NMR spectra of $Li_{4.4}Al_{0.4}Ge_{0.6}S_4$ and $Li_{4.4}Al_{0.4}Sn_{0.6}S_4$ are given in Figure 6.2b. Both spectra are dominated by a resonance with an isotropic chemical shift at ~130 ppm attributed to AlS_4 tetrahedra based on known literature values for this environment[25] and in agreement with the Al^{3+} occupying the tetrahedral layer of these phases (Figure 6.1a). The two-dimensional ^{27}Al 3QMAS NMR spectrum of $Li_{4.4}Al_{0.4}Ge_{0.6}S_4$ (Figure 6.2c) around the AlS_4 region shows the presence of two slightly different Al environments (Al1: δ_{iso} = 131.8(1) ppm, C_Q = 0.5(1) MHz; Al2: δ_{iso} = 130.8(1) ppm, C_Q = 1.9(1) MHz), corresponding to two partially occupied Al^{3+} sites with integrals of ~28.1(2):71.9(2). A single AlS_4 peak is observed in the 3QMAS NMR spectrum of $Li_{4.4}Al_{0.4}Sn_{0.6}S_4$ and indicates that the NMR shifts and quadrupolar parameters (δ_{iso} = 131.2 ppm, C_Q = 1.3(2)

MHz) of both Al^{3+} sites are too close to enable their resolution under the experimental condition used to acquire these data.

The presence of two AlS_4 sites in $Li_{4.4}Al_{0.4}Ge_{0.6}S_4$ and not in $Li_{4.4}Al_{0.4}Sn_{0.6}S_4$ is normally irregular, as with ^6Li NMR data above, one would assume that the material with faster Li dynamics would show a narrow peak in comparison to that with slower Li dynamics – which is not the case here. However, one reason for the two Al resonances in $Li_{4.4}Al_{0.4}Ge_{0.6}S_4$ may be well explained by its crystal structure and the occupancies of Li sites. Li^+ ions move through the crystal structure by migrating between Li2 and Li3 sites, as observed by the fast motion regime on the NMR time scale (see relaxometry section) and molecular dynamics calculation.[1] Normally this would result in the environments neighbouring Li to also narrow due to averaging of heteronuclear dipolar and quadrupolar interactions. For $Li_{4.4}Al_{0.4}Ge_{0.6}S_4$, Li2 migrates to Li3, which leaves the Li2 and the corresponding Li1 sites vacant. These AlS_4 tetrahedra would have a different local environment to those with no vacant Li1/2 site. The occupancies of Li1 and Li2 are 0.738 and 0.254, respectively, which suggests only ~25% of Li migrates through the structure. The ratio is similar to the integrals of the Al resonances, and so one could suggest that Al2 has all its neighbouring Li1/2 sites occupied, while Al1 would have a fast moving Li^+ ion nearby, averaging out the quadrupolar interactions, which can be seen by the smaller quadrupolar coupling constant. For $Li_{4.4}Al_{0.4}Sn_{0.6}S_4$, two Al sites would also be expected, however Li is still in the slow motion regime which would not enable Li2-Li3 migration on the NMR time scale. The resulting spectra arises from the fast Li1-Li2 diffusion process, which would give a single narrow resonance, average of the resonances for each occupied Li site, which

is what is observed.

The much smaller ^{27}Al signals at ~15 ppm are assigned to a small amount of corundum (α-Al_2O_3) impurity (Figure 6.2b) based on the literature value for octahedral Al in this phase.[26,27] The experimental value of ~2.4(1) wt% of Al_2O_3 in the sample obtained by NMR is consistent with the value of 2.2 wt% observed in PXRD analysis.[1] A very small amount of α-Al_2O_3 (see insert) is also seen in $Li_{4.4}Al_{0.4}Sn_{0.6}S_4$ that was not observed in PXRD. The NMR spectrum for $Li_{4.4}Al_{0.4}Sn_{0.6}S_4$ (Figure 6.2b, red) is not quantitative (recycle delay << $5\times T_1$ for α-Al_2O_3) due to time constraints during this project, and thus experimental amounts cannot be determined from this spectrum.

The room temperature ^{119}Sn MAS NMR spectrum of $Li_{4.4}Al_{0.4}Sn_{0.6}S_4$ is given in Figure 6.3 and shows resonances between 40 and 90 ppm in a region similar to the tetrahedral SnS_4 in $Li_{10}SnP_2S_{12}$.[28] A single ^{119}Sn resonance would be expected from the symmetrical Sn tetrahedra with identical Sn-S bond lengths (of 2.324(2) Å) and an average S-Sn-S bond angle of 109.5(1)^o, however at least 6 ^{119}Sn signals are detected with relative ratios of each resonance from upfield to downfield is approximately 3:3:2:1:1:3, which suggests the presence of local disorder undetected by PXRD analysis. Based on basic NMR shielding theory, we can deduce these peaks arise from short range ordering of Li based on varying Sn–Li distances range from 3.0(1) to 4.2(1) Å of the three Li sites and exact Li positions. The relative occupancies of each Li site, however, makes exact assignments of each resonance non-trivial and therefore would greatly benefit from DFT-GIPAW calculations. However, one could assign the broad resonance at 65.8(4) ppm as the SiS_4 in close proximity to mobile Li3 (see Li^+ dynamics section) undergoing multiple

environments on the NMR time scale.

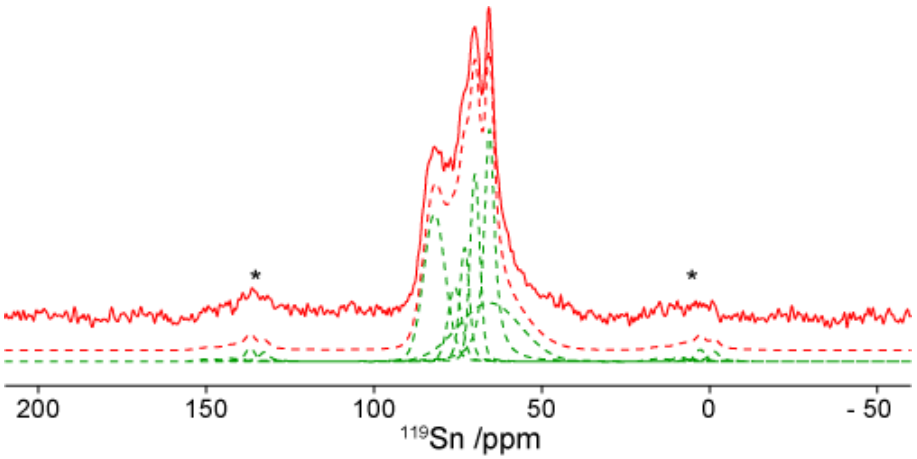

Figure 6.3. ^{119}Sn MAS NMR spectrum of $Li_{4.4}Al_{0.4}Sn_{0.6}S_4$ at MAS rate of 10 kHz. Red dotted line represents the sum of the simulated peaks (dotted green). Asterisks (*) denote spinning sidebands. Simulation was performed using the SOLA package in Bruker TopSpin®.

6.2.2 Li^+ Dynamics: Line narrowing

The temperature dependences of the ^{7}Li static NMR spectra of $Li_{4.4}Al_{0.4}Ge_{0.6}S_4$ and $Li_{4.4}Al_{0.4}Sn_{0.6}S_4$ are shown in Figure 6.4a and b. In static ^{7}Li (spin 3/2) NMR spectra of Li-containing materials and in the absence of Li^+ mobility, the 1/2↔-1/2 central transition is broadened in the kHz regime by the ^{7}Li-^{7}Li homonuclear dipolar interactions as seen at 121 K here where fwhm of ~5.5 kHz are obtained for $Li_{4.4}Al_{0.4}Sn_{0.6}S_4$. Although a plateau is not observed at low temperature for $Li_{4.4}Al_{0.4}Ge_{0.6}S_4$, similar fwhm is expected for both materials as the density of ^{7}Li spins is identical in isostructural $Li_{4.4}Al_{0.4}Ge_{0.6}S_4$ and $Li_{4.4}Al_{0.4}Sn_{0.6}S_4$ phases at ~15.8 Li per unit cell. The unit cell volumes are 333.1 Å^3 and 346.2 Å^3 for $Li_{4.4}Al_{0.4}Ge_{0.6}S_4$ and $Li_{4.4}Al_{0.4}Sn_{0.6}S_4$, respectively, and therefore a fwhm of ~5.7 kHz would be expected for $Li_{4.4}Al_{0.4}Ge_{0.6}S_4$.

Upon heating, line narrowing of the central transition is observed and this results from an averaging to zero of the ^{7}Li dipolar coupling interaction indicative of increasing Li^{+} mobility. At 411 K for $Li_{4.4}Al_{0.4}Ge_{0.6}S_4$ and 538 K for $Li_{4.4}Al_{0.4}Sn_{0.6}S_4$, the NMR spectra show the expected line shape from a spin 3/2 nucleus, with broad shoulders on either side of the central transition arising from the 3/2↔1/2 and -3/2↔-1/2 satellite transitions that permit the determination of quadrupolar coupling constants of ~15-17 kHz. The quadrupolar coupling constant did not change with increase in temperature, highlighting the Li^{+} dynamics are below ~15 kHz at 611 K.

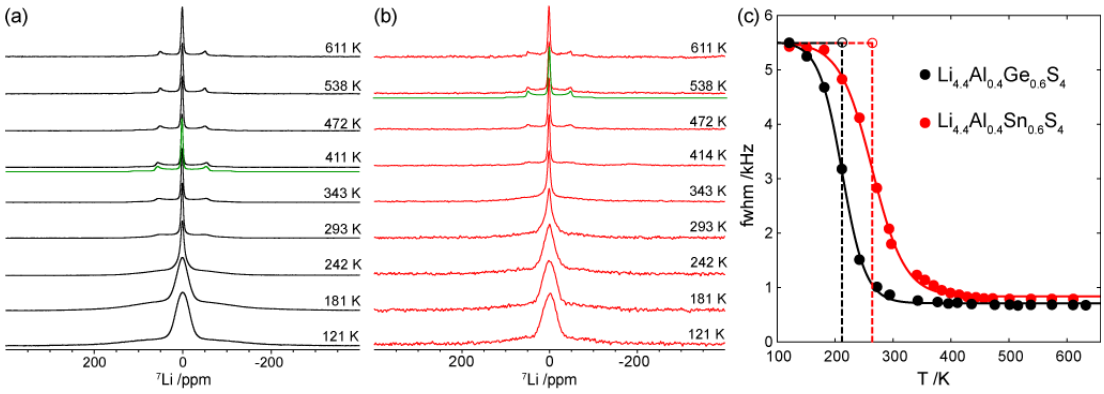

Figure 6.4. ^{7}Li NMR spectra as a function of temperature for (a) $Li_{4.4}Al_{0.4}Ge_{0.6}S_4$ and (b) $Li_{4.4}Al_{0.4}Sn_{0.6}S_4$. The green spectra are the line shape simulations of a single Li environment with quadrupole coupling constants C_Q of ~17 kHz (for $Li_{4.4}Al_{0.4}Ge_{0.6}S_4$) and ~15 kHz (for $Li_{4.4}Al_{0.4}Sn_{0.6}S_4$) with null asymmetry parameters η. Simulation was performed using the SOLA package in Bruker TopSpin®. (c) Temperature dependence of ^{7}NMR line width of $Li_{4.4}Al_{0.4}Ge_{0.6}S_4$ (black) and $Li_{4.4}Al_{0.4}Sn_{0.6}S_4$ (red) fitted with sigmoidal regression curve (solid lines). The vertical and horizontal dashed lines give the temperatures corresponding to the inflection point of the regression curve and the NMR line width used to determine the Li^{+} jump rates τ^{-1}, respectively.

The room temperature ^{7}Li central transition of the static NMR spectrum of $Li_{4.4}Al_{0.4}Sn_{0.6}S_4$ is much broader than that of $Li_{4.4}Al_{0.4}Ge_{0.6}S_4$ (fwhm ~2 kHz vs ~860 Hz), demonstrating that Li^+ ions in the latter phase are in the fast motion regime and more mobile than in $Li_{4.4}Al_{0.4}Ge_{0.6}S_4$. This could also be quantified in Figure 6.4c by comparing the temperature dependence of the ^{7}Li central transition NMR line widths for both $Li_{4.4}Al_{0.4}Ge_{0.6}S_4$ and $Li_{4.4}Al_{0.4}Sn_{0.6}S_4$. The inflection point of this regression curve defines the Li^+ jump rates τ^{-1}, which are of the order of the central transition NMR line width in the rigid lattice regime (fwhm ~5.5-7 kHz), yielding values of ~3.6 x 10^4 s^{-1} and ~3.5 x 10^4 s^{-1} at 212(10) and 264(5) K for $Li_{4.4}Al_{0.4}Ge_{0.6}S_4$ and $Li_{4.4}Al_{0.4}Sn_{0.6}S_4$, respectively. The onset of motional narrowing therefore occurs at a lower temperature for the Ge phase than for the Sn phase, indicating faster Li^+ ion dynamics in the former phase.

6.2.3 NMR Dynamics: Relaxometry

Further information on Li^+ dynamics on the MHz and kHz timescale were obtained by monitoring the temperature dependence of the ^{7}Li spin-lattice relaxation rates (SLR) in the laboratory frame (T_1^{-1}) and rotating frame ($T_{1\rho}^{-1}$) under static conditions (Figure 6.5). The room temperature $T_1(^7Li)/T_1(^6Li)$ ratio was measured as 1.2 for $Li_{4.4}Al_{0.4}Ge_{0.6}S_4$ and 0.9 for $Li_{4.4}Al_{0.4}Sn_{0.6}S_4$, signifying a predominantly dipolar mechanism for Li diffusion in these samples, allowing application of the Bloembergen-Purcell-Pound (BPP) theory.[29]

Upon heating, the SLR T_1^{-1} values for both $Li_{4.4}Al_{0.4}Ge_{0.6}S_4$ and $Li_{4.4}Al_{0.4}Sn_{0.6}S_4$ materials increase with temperature with an activation barrier

of 0.19(2) eV below room temperature and 0.11(1) eV above room temperature for $Li_{4.4}Al_{0.4}Ge_{0.6}S_4$ (blue circles in Figure 6.5a) and 0.26(3) eV above 250 K for $Li_{4.4}Al_{0.4}Sn_{0.6}S_4$ (red circles in Figure 6.5b), and are indicative of the slow motion regime (where $\omega_0\tau_c >> 1$, where ω_0 is the Larmor frequency and τ_c is the correlation time of Li motion), characterising local hopping processes between local energy minima and unsuccessful jumps to the neighbouring sites.

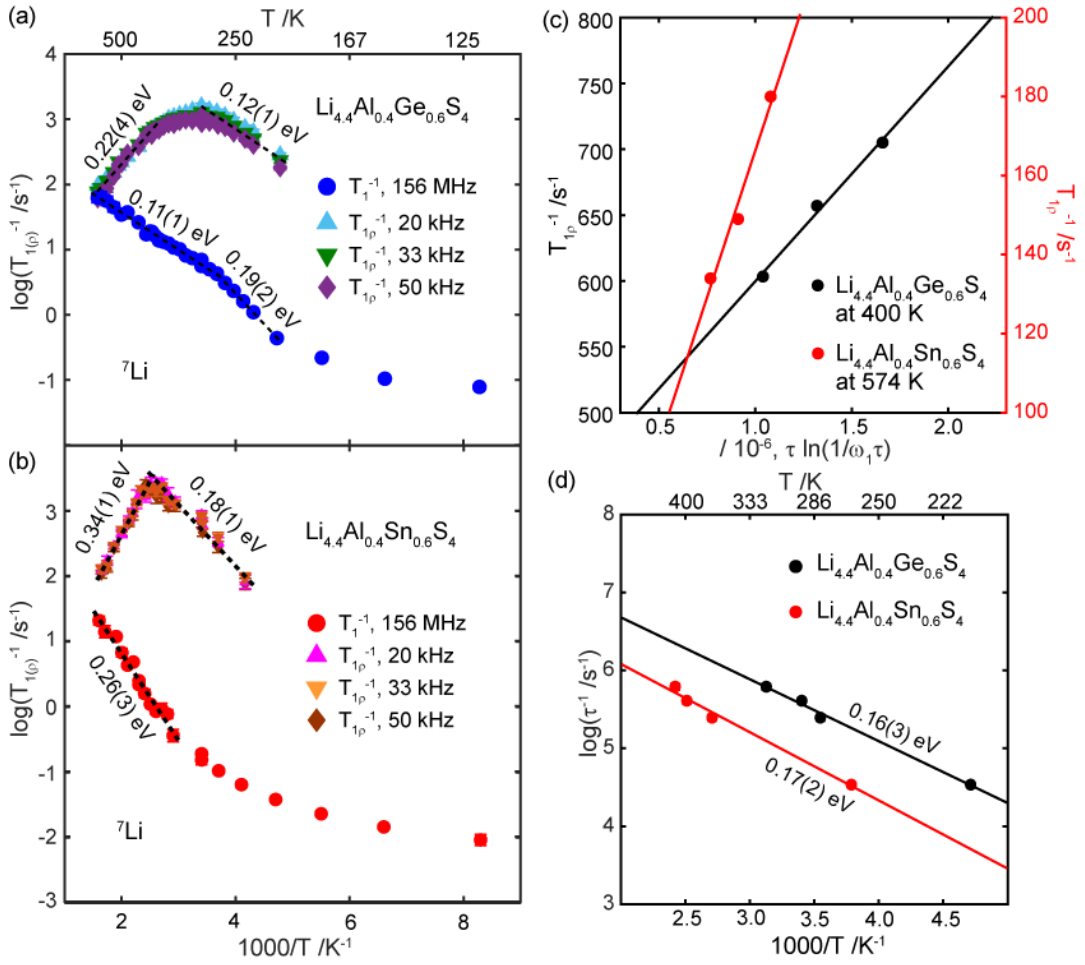

Figure 6.5. Arrhenius plot of spin-lattice relaxation (SLR) rates in the laboratory frame (T_1^{-1}) and the rotating frame ($T_{1\rho}^{-1}$) for (a) $Li_{4.4}Al_{0.4}Ge_{0.6}S_4$ and (b) $Li_{4.4}Al_{0.4}Sn_{0.6}S_4$. The black dotted lines represent the temperature range where the activation energy E_a is determined. (c) Frequency dependence of $T_{1\rho}^{-1}$ for $Li_{4.4}Al_{0.4}Ge_{0.6}S_4$ (black) and $Li_{4.4}Al_{0.4}Sn_{0.6}S_4$ (red). (d) Arrhenius plot of Li^+ jump

rates τ^{-1} extracted from ^{7}Li line width analysis and SLR experiments for $Li_{4.4}Al_{0.4}Ge_{0.6}S_4$ (black) and $Li_{4.4}Al_{0.4}Sn_{0.6}S_4$ (red).

In $Li_{4.4}Al_{0.4}Ge_{0.6}S_4$, the SLR $T_{1\rho}^{-1}$ values increase with temperature between 200 K and room temperature with an activation barrier of 0.12(1) eV and suggests that this hopping process occurring in the ms time scale is similar to the one observed in the ns time scale in the SLR T_1^{-1} data above. In $Li_{4.4}Al_{0.4}Sn_{0.6}S_4$, the SLR $T_{1\rho}^{-1}$ values measured up to 370 K give an activation barrier of 0.18(1) eV and describe a much slower diffusion process that the one probed in the T_1^{-1} data. Note that the $T_{1\rho}^{-1}$ values for $Li_{4.4}Al_{0.4}Sn_{0.6}S_4$ are larger than the ones obtained for $Li_{4.4}Al_{0.4}Ge_{0.6}S_4$, highlighting the more favourable hopping process found with the Ge phase. The fast motional regime characterised by $\omega_1\tau_c << 1$ (where ω_1 is the spin-lock frequency) and corresponding translational diffusion of Li^+ ions evidenced by $T_{1\rho}^{-1}$ values decreasing with increasing temperatures is observed above 320 and 414 K for $Li_{4.4}Al_{0.4}Ge_{0.6}S_4$ and $Li_{4.4}Al_{0.4}Sn_{0.6}S_4$, respectively (Figure 6.5a, b). The lower temperature of these $T_{1\rho}^{-1}$ maxima for the Ge phase show that the Li^+ ions are more mobile in this phase than in the Sn phase. This is also associated with a smaller activation barrier for Li^+ hopping of 0.22(4) eV for $Li_{4.4}Al_{0.4}Ge_{0.6}S_4$ and 0.34(1) eV for $Li_{4.4}Al_{0.4}Sn_{0.6}S_4$.

$T_{1\rho}^{-1}$ maxima are observed where Li^+ ion jump rates τ^{-1} are on the order of the probe frequency ω_1 and followed the following equation $2\omega_1\tau_c \approx 1$.[30] Jump rates in the order of 2–7 x 10^5 s^{-1} in the 280-320 K and 370-420 K temperature range for $Li_{4.4}Al_{0.4}Ge_{0.6}S_4$ and $Li_{4.4}Al_{0.4}Sn_{0.6}S_4$, respectively, are therefore obtained.

The dimensionality of the Li^+ ion diffusion can be accessed from the

frequency-dependence of the high temperature limits of the SLR $T_{1\rho}^{-1}$ values with one, two and three dimensional diffusion in solids being proportional to $(\tau/\omega)^{0.5}$, $\tau \ln(1/\omega\tau)$ or τ, respectively (where τ and ω are the correlation times and probe frequencies, see Chapter 2).[31,32] A plot of $T_{1\rho}^{-1}$ values against $\tau \ln(1/\omega\tau)$ at 400 K for $Li_{4.4}Al_{0.4}Ge_{0.6}S_4$ and at 574 K for $Li_{4.4}Al_{0.4}Sn_{0.6}S_4$ (Figure 6.5c), which are in the fast motion regime for the respective samples, reveals a clear linear trend, demonstrating two dimensional lithium diffusion in this family of materials.

The BPP theory of relaxation predicts a quadratic dependence of the SLRs with the probe frequency (*i.e.* $T_{1\rho}^{-1} \propto \omega^{-\beta}$ with $\beta = 2$), however this is often not the case in fast Li^+ ion conductors.[31] This results in an asymmetric behaviour of $T_{1\rho}^{-1}$ rates in the fast and slow motional regimes, as indeed observed for both $Li_{4.4}Al_{0.4}Ge_{0.6}S_4$ and $Li_{4.4}Al_{0.4}Sn_{0.6}S_4$ (Figure 6.5a,b), which arises from local interactions including repulsive Coulomb interactions and structural disorder. The deviation from BPP can be characterised from a correlation factor β which is determined by $E_{a,low} = E_{a,high}(\beta - 1)$, where $E_{a,low}$ and $E_{a,high}$ are the activation barriers in the slow and fast motion regimes, respectively; here similar β values were obtained for $Li_{4.4}Al_{0.4}Ge_{0.6}S_4$ ($\beta(Li_{4.4}Al_{0.4}Ge_{0.6}S_4) \approx 1.55$) and $Li_{4.4}Al_{0.4}Sn_{0.6}S_4$ ($\beta(Li_{4.4}Al_{0.4}Sn_{0.6}S_4) \approx 1.53$) also suggesting a similar Li^+ diffusion pathway.

NMR-derived jump rates τ^{-1} from NMR line narrowing experiments and relaxometry experiments are plotted against reciprocal temperature in Figure 6.5d. Fitting to $\tau^{-1} = \tau_0^{-1} \exp(-E_a/RT)$ yields activation barriers of 0.16(3) and 0.17(2) eV and pre-exponential factors τ_0^{-1} of 1.9(1.4) x 10^8 and 6.8(2.7) x 10^7 s^{-1} for $Li_{4.4}Al_{0.4}Ge_{0.6}S_4$ and $Li_{4.4}Al_{0.4}Sn_{0.6}S_4$, respectively. The activation barrier

for $Li_{4.4}Al_{0.4}Ge_{0.6}S_4$ is within error of the value extracted from the high temperature flank of the relaxometry plot (0.22(4) eV), suggesting the same two dimensional Li^+ diffusion process is measured in the line narrowing and relaxometry experiments. However, in the case of $Li_{4.4}Al_{0.4}Sn_{0.6}S_4$, the activation barrier of 0.17(2) eV is not within the range of the long range Li^+ diffusion of the $T_{1\rho}^{-1}$ rates (0.34(1) eV, Figure 6.5b) and suggests that a much slower dynamics process than two dimensional diffusion is also present, explaining the lower conductivity of this phase compared to $Li_{4.4}Al_{0.4}Ge_{0.6}S_4$. *Ab initio* molecular dynamics studies of $Li_{4.4}Al_{0.4}Ge_{0.6}S_4$ show a two dimensional Li^+ ion diffusion process between Li2 and Li3 with an energy barrier of 0.17 eV.[1] These complement NMR data well in both activation barrier values (0.16(3) eV) and diffusion dimensionality.

The τ_0^{-1} values of $Li_{4.4}Al_{0.4}Ge_{0.6}S_4$ and $Li_{4.4}Al_{0.4}Sn_{0.6}S_4$ are lower by a few orders of magnitude compared to that observed for crystal lattice vibration (~10^{13} s^{-1}). This could be explained with a similar explanation described in Chapter 4 where the shallow potential wells of Li reduce these values. This motion could be attributed to the Li moving between Li1 and Li2, where the activation barrier for diffusion is approximately 0.055 and 0.01 eV for Li1–Li2 and Li2–Li1 diffusion, respectively, observed by molecular dynamics calculations.[1]

NMR conductivity σ_{NMR} can be estimated from the Li^+ jump rates τ^{-1} using the combined Nernst-Einstein and Einstein-Smoluchowski equations (Equation 2.32) where f/H_R is the correlation factor and Haven ratio (1 for uncorrelated motion), N_{CC} is the number of charge carriers per unit cell volume (335.5(2)-337.8(2) $Å^3$ for $Li_{4.4}Al_{0.4}Ge_{0.6}S_4$ and 349.6(2)-352.9(2) $Å^3$ for

$Li_{4.4}Al_{0.4}Sn_{0.6}S_4$ in this temperature range), q is the ionic charge of Li^+, a is the closest Li2–Li3 jump distance at room temperature (3.1(1) Å for $Li_{4.4}Al_{0.4}Ge_{0.6}S_4$ and $Li_{4.4}Al_{0.4}Sn_{0.6}S_4$), N_{NN} is the number of neighbouring Li sites (4 for the two dimensional diffusion here).[33] The extrapolated conductivity values at 303 K for $Li_{4.4}Al_{0.4}Ge_{0.6}S_4$ and $Li_{4.4}Al_{0.4}Sn_{0.6}S_4$ are 1.9(1) x 10^{-5} S cm^{-1} and 3.6(4) x 10^{-6} S cm^{-1} respectively (see Figure 6.6) with activation barriers of 0.14(2) and 0.15(3) eV. AC impedance finds similar conductivity values,[1] however the activation barriers are significantly lower when measured by NMR spectroscopy, as NMR determines the barrier of diffusion of Li to its neighbouring site, whereas impedance measurements probe longer range translational Li^+ diffusion.[7,34–38]

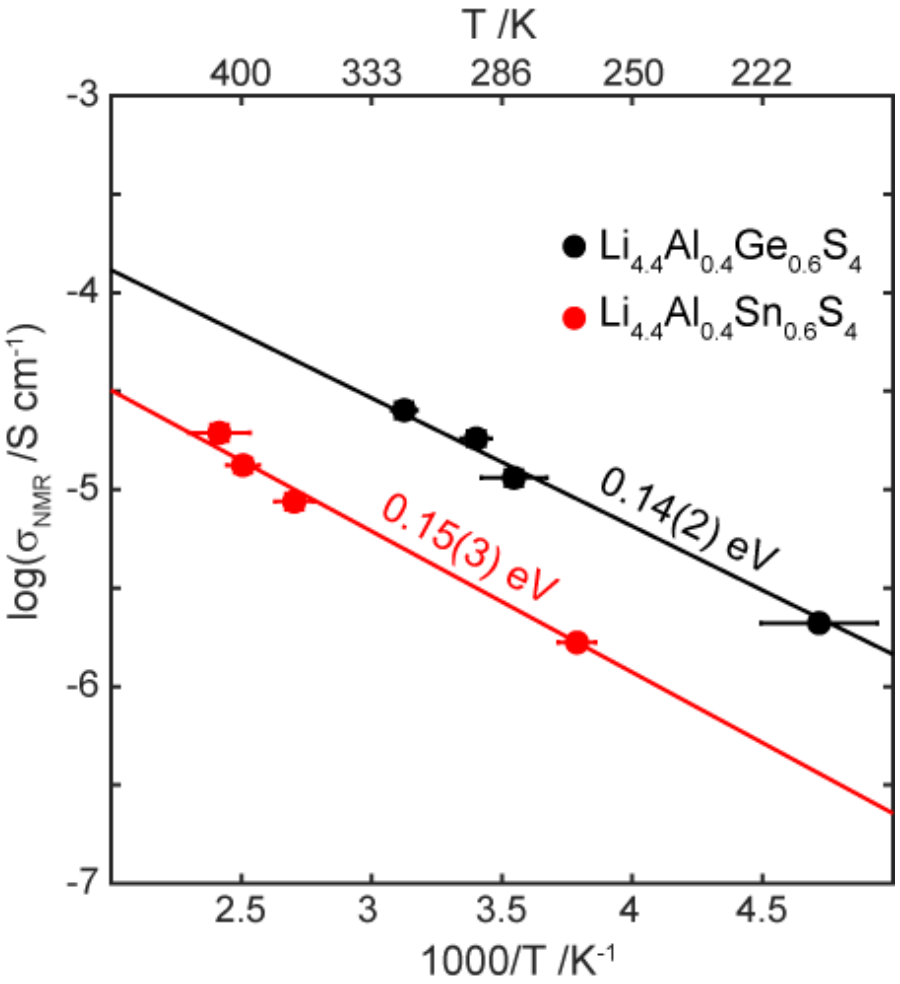

Figure 6.6. Arrhenius plot of NMR conductivity of $Li_{4.4}Al_{0.4}Ge_{0.6}S_4$ (black) and $Li_{4.4}Al_{0.4}Sn_{0.6}S_4$ (red). Horizontal error bars denote the sample temperature gradient in the NMR probe.

6.3 Conclusions

In this chapter, we identified the local structure of both $Li_{4.4}Al_{0.4}Ge_{0.6}S_4$ and $Li_{4.4}Al_{0.4}Sn_{0.6}S_4$ phases. All Li environments were observed in ^{6}Li MAS NMR and the relative intensities of each site was found to be in agreement with the structure obtained by diffraction. ^{27}Al and ^{119}Sn MAS NMR highlighted the presence of multiple AlS_4 and SnS_4 environments in $Li_{4.4}Al_{0.4}Ge_{0.6}S_4$ and $Li_{4.4}Al_{0.4}Sn_{0.6}S_4$ respectively, which may be attributed to the distribution of local

Li sites, especially with regards to Li1 and Li2, and the occupancies of Li3 sites.

Li^+ dynamics studied using ^7Li relaxometry identified the long range ionic diffusion is two dimensional with an activation barrier of ~0.17 eV in both $Li_{4.4}Al_{0.4}Ge_{0.6}S_4$ and $Li_{4.4}Al_{0.4}Sn_{0.6}S_4$, complemented by computational results. $Li_{4.4}Al_{0.4}Ge_{0.6}S_4$ was found to have faster Li^+ dynamics compared to $Li_{4.4}Al_{0.4}Sn_{0.6}S_4$, in agreement with AC impedance studies. The low activation barrier observed by NMR is comparable to the LGPS family (see Chapter 3).[7,39,40] Therefore with further control of defect chemistry, faster Li^+ dynamics may be achieved, giving rise to a fast Li^+ ion conductor with high stability to Li metal. One such approach that could be taken is to replace Ge with Si, as Kuhn *et al*. reported faster Li^+ dynamics in $Li_{11}Si_2PS_{12}$ and $Li_{10}SiP_2S_{12}$ compared to $Li_{10}GeP_2S_{12}$.[39]

Further work could be performed regarding Li dynamics in both phases such as variable temperature EXSY and spin alignment echo NMR to understand the Li^+ diffusion process on another NMR time scale, predominantly identifying the cause of the difference between activation barriers in $Li_{4.4}Al_{0.4}Sn_{0.6}S_4$ between different methods. ^6Li–^{119}Sn HMQC experiments on $Li_{4.4}Al_{0.4}Sn_{0.6}S_4$ could also be used to understand the origins of the multiple peaks observed in ^{119}Sn NMR, in order to understand the local structure of these phases further, which could then allow one to further understand the diffusion process along the diffusion plane.

6.4 References

1 B. T. Leube, K. K. Inglis, E. J. Carrington, P. M. Sharp, J. F. Shin, A. R. Neale, T. D. Manning, M. J. Pitcher, L. J. Hardwick, M. S. Dyer, F. Blanc,

J. B. Claridge and M. J. Rosseinsky, *Chem. Mater.*, 2018, **30**, 7183–7200.

2 R. Kanno, T. Hata, Y. Kawamoto and M. Irie, *Solid State Ionics*, 2000, **130**, 97–104.

3 R. Kanno and M. Murayama, *J. Electrochem. Soc.*, 2001, **148**, A742–A746.

4 P. Knauth, *Solid State Ionics*, 2009, **180**, 911–916.

5 R. Chen, W. Qu, X. Guo, L. Li and F. Wu, *Mater. Horiz*, 2016, **3**, 487–516.

6 N. Kamaya, K. Homma, Y. Yamakawa, M. Hirayama, R. Kanno, M. Yonemura, T. Kamiyama, Y. Kato, S. Hama, K. Kawamoto and A. Mitsui, *Nat. Mater.*, 2011, **10**, 682–686.

7 A. Kuhn, V. Duppel and B. V. Lotsch, *Energy Environ. Sci.*, 2013, **6**, 3548.

8 A. Kuhn, O. Gerbig, C. Zhu, F. Falkenberg, J. Maier and B. V. Lotsch, *Phys. Chem. Chem. Phys.*, 2014, **16**, 14669–14674.

9 H. Muramatsu, A. Hayashi, T. Ohtomo, S. Hama and M. Tatsumisago, *Solid State Ionics*, 2011, **182**, 116–119.

10 S. Wenzel, S. Randau, T. Leichtweiß, D. A. Weber, J. Sann, W. G. Zeier and J. Janek, *Chem. Mater.*, 2016, **28**, 2400–2407.

11 T. Cheng, B. V Merinov, S. Morozov and W. A. Goddard, *ACS Energy Lett.*, 2017, **2**, 1454–1459.

12 P. Zhou, J. Wang, F. Cheng, F. Li and J. Chen, *Chem. Commun.*, 2016, **52**, 6091–6094.

13 H. Lim, S.-C. Kim, J. Kim, Y.-I. Kim and S.-J. Kim, *J. Solid State Chem.*, 2018, **257**, 19–25.

14 M. Murayama, R. Kanno, M. Irie, S. Ito, T. Hata, N. Sonoyama and Y. Kawamoto, *J. Solid State Chem.*, 2002, **168**, 140–148.

15 J. H. MacNeil, D. M. Massi, J.-H. Zhang, K. A. Rosmus, C. D. Brunetta, T. A. Gentile and J. A. Aitken, *J. Alloys Compd.*, 2014, **586**, 736–744.

16 L. Frydman and J. S. Harwood, *J. Am. Chem. Soc.*, 1995, **117**, 5367–5368.

17 A. Medek, J. S. Harwood and L. Frydman, *J. Am. Chem. Soc.*, 1995, **117**, 12779–12787.

18 J.-P. Amoureux, C. Fernandez and S. Steuernagel, *J. Magn. Reson. Ser. A*, 1996, **123**, 116–118.

19 N. J. Clayden, C. M. Dobson and A. Fern, *J. Chem. Soc. Dalt. Trans.*, 1989, **0**, 843.

20 A. Bielecki and D. P. Burum, *J. Magn. Reson. Ser. A*, 1995, **116**, 215–220.

21 P. A. Beckmann and C. Dybowski, *J. Magn. Reson.*, 2000, **146**, 379–380.

22 K. D. Becker, *J. Chem. Phys.*, 1978, **68**, 3785–3793.

23 J. Wu, N. Kim and J. F. Stebbins, *Solid State Nucl. Magn. Reson.*, 2011, **40**, 45–50.

24 K. J. D. MacKenzie and M. E. Smith, *Multinuclear Solid-State Nuclear Magnetic Resonance of Inorganic Materials*, Elsevier, Oxford, 2002.

25 M. Haouas, F. Taulelle and C. Martineau, *Prog. Nucl. Magn. Reson. Spectrosc.*, 2016, **94**–**95**, 11–36.

26 H. J. Jakobsen, J. Skibsted, H. Bildsøe and N. C. Nielsen, *J. Magn. Reson.*, 1989, **85**, 173–180.

27 M. Choi, K. Matsunaga, F. Oba and I. Tanaka, *J. Phys. Chem. C*, 2009, **113**, 3869–3873.

28 M. Kaus, H. Stöffler, M. Yavuz, T. Zinkevich, M. Knapp, H. Ehrenberg and S. Indris, *J. Phys. Chem. C*, 2017, **121**, 23370–23376.

29 N. Bloembergen, E. M. Purcell and R. V Pound, *Phys. Rev.*, 1948, **73**, 679–712.

30 A. Abragam, *The Principles of Nuclear Magnetism*, Oxford University Press, Oxford, 1961.

31 P. Heitjans, A. Schirmer and S. Indris, *NMR and β-NMR Studies of Diffusion in Interface-Dominated and Disordered Solids*, Springer-Verlag Berlin Heidelberg, The Netherlands, 2005.

32 A. Kuhn, P. Sreeraj, R. Pöttgen, H. D. Wiemhöfer, M. Wilkening and P. Heitjans, *J. Am. Chem. Soc.*, 2011, **133**, 11018–11021.

33 H. Mehrer, *Diffusion in solids: fundamentals, methods, materials, diffusion-controlled processes*, Springer Berlin Heidelberg, Berlin, Heidelberg, 2007, vol. 155.

34 L. Enciso-Maldonado, M. S. Dyer, M. D. Jones, M. Li, J. L. Payne, M. J. Pitcher, M. K. Omir, J. B. Claridge, F. Blanc and M. J. Rosseinsky, *Chem. Mater.*, 2015, **27**, 2074–2091.

35 L. Latie, G. Villeneuve, D. Conte and G. Le Flem, *J. Solid State Chem.*, 1984, **51**, 293–299.

36 Y. Deng, C. Eames, J.-N. Chotard, F. Lalère, V. Seznec, S. Emge, O. Pecher, C. P. Grey, C. Masquelier and M. S. Islam, *J. Am. Chem. Soc.*, 2015, **137**, 9136–9145.

37 K. Arbi, M. G. Lazarraga, D. Ben Hassen Chehimi, M. Ayadi-Trabelsi, J.

M. Rojo and J. Sanz, *Chem. Mater.*, 2004, **16**, 255–262.

38 A. B. Santibáñez-Mendieta, C. Didier, K. K. Inglis, A. J. Corkett, M. J. Pitcher, M. Zanella, J. F. Shin, L. M. Daniels, A. Rakhmatullin, M. Li, M. S. Dyer, J. B. Claridge, F. Blanc and M. J. Rosseinsky, *Chem. Mater.*, 2016, **28**, 7833–7851.

39 A. Kuhn, O. Gerbig, C. Zhu, F. Falkenberg, J. Maier and B. V. Lotsch, *Phys. Chem. Chem. Phys.*, 2014, **16**, 14669–14674.

40 Y.-X. Xiang, G. Zheng, G. Zhong, D. Wang, R. Fu and Y. Yang, *Solid State Ionics*, 2018, **318**, 19–26.

7. Overall Conclusions and Outlook

In this thesis, new Li^+ ion conductors from three crystallographic families spanning perovskites, NASICONs and sulfides were studied using solid state NMR spectroscopy.

A new family of Li^+ ion conductors was identified in the study of the perovskite $La_3Li_3W_2O_{12}$.[1] This is the first material consisting of the perovskite family that contains Li^+ on both the A- and B-site of the crystal structure, and showed computational evidence of motion between the two distinct sites which has not been previously observed. ^6Li solid state NMR was used to experimentally identify the two distinct Li^+ sites present in this material with a 1:2 A-:B-site ratio per unit cell, and the large disorder observed in the diffraction derived crystal structure was verified by ^{17}O MAS NMR with the NMR line widths not being affected by the change in magnetic field. The distribution of the ^{17}O resonances were related to the number of A-site Li surrounding a single O atom, complemented by DFT GIPAW calculations. ^6Li exchange spectroscopy NMR experiments was then used to identify Li^+ mobility between the A- and B-sites. Increase in cross peak signal intensity were observed and were assigned as site migration of Li between the two sites, as the MAS rate was significantly larger than the ^6Li–^6Li homonuclear dipolar coupling. The rate of exchange was not determined, however one could measure it with a larger number of mixing times. ^7Li–^{17}O heteronuclear multiple quantum NMR experiments showed some correlation between ^7Li and ^{17}O nuclei, however hardware issues prevented full acquisition of the data in the F_1 dimension, not allowing full analysis of the data.

Li^+ dynamics investigation of $La_3Li_3W_2O_{12}$ was performed by using

variable temperature ^{6,7}Li NMR spectroscopy. ^{6,7}Li NMR relaxometry found the activation barrier for 3D Li^+ diffusion as 0.29(17) eV, consistent with the value determined by molecular dynamics calculations of the A-site to A-site Li^+ hopping process. This low activation barrier is comparable to the best oxide-based Li^+ ion conductors currently known in literature such as the perovskite $La_{2/3-x}Li_{3x}TiO_3$ family and the garnet Al-doped $Li_7La_3Zr_2O_{12}$, highlighting the high potential of $La_3Li_3W_2O_{12}$. The activation barrier seen by NMR is significantly lower in comparison to AC impedance spectroscopy and is consistent with literature and could be attributed to AC impedance measuring resistance, with its value containing contributions from processes such as defect formation and percolation issues of Li^+ in the material. Therefore, if defects are introduced prior to probing conductivity to improve Li^+ percolation, a smaller activation barrier to Li^+ diffusion similar to that observed by NMR may be possible. The study on $La_3Li_3W_2O_{12}$ was published in Chemistry of Materials in 2016.

In chapter 5, structural and Li^+ dynamics analysis of the two NASICON materials of compositions $Li_{0.925}Ta_{1.062}Al_{0.938}P_{3.16}O_{12+x}$ and $Li_{0.734}Ta_{1.187}Ca_{0.108}Al_{0.705}P_3O_{12}$ were performed. ^{27}Al MAS NMR of both materials showed the presence of octahedral Al assigned to the main NASICON phases with further resonances assigned as multiple $AlPO_4$ impurities arising from synthesis, and to $Li_9Al_3(P_2O_7)_3(PO_4)_2$, both of which are observed in literature. ^{31}P NMR also reveals these impurities, with additional resonances arising from $Li_4P_2O_7$ in $Li_{0.925}Ta_{1.062}Al_{0.938}P_{3.16}O_{12+x}$. ^{6}Li NMR, a complex NMR line shape is observed for the undoped composition, which are assigned to the multiple Li-containing impurities derived from ^{27}Al and ^{31}P NMR,

with a sharp resonance at *ca.* 0 ppm, which is assigned to fast Li motion in the NASICON framework, as observed by variable temperature ^{7}Li NMR. ^{6}Li NMR spectrum for $Li_{0.734}Ta_{1.187}Ca_{0.108}Al_{0.705}P_3O_{12}$ showed two resonances assigned to the 6- and 8-coordinated A_1 and A_2 Li sites in the NASICON structure.

Variable temperature ^{7}Li NMR relaxometry highlighted the slower Li^+ dynamics in $Li_{0.734}Ta_{1.187}Ca_{0.108}Al_{0.705}P_3O_{12}$ compared to $Li_{0.925}Ta_{1.062}Al_{0.938}P_{3.16}O_{12+x}$. The undoped composition was found to have an onset temperature of Li^+ mobility as ~190 K, significantly lower than that of the Ca^{2+} doped sample at ~290 K. In the undoped composition, the satellite transitions of ^{7}Li NMR spectra widened as temperature increased, which indicates anisotropic thermal expansion of the NASICON framework and is observed in other NASICONs of varying compositions. This trend was not observed with $Li_{0.734}Ta_{1.187}Ca_{0.108}Al_{0.705}P_3O_{12}$ as the ^{7}Li satellite transitions were not observed.

Activation barriers to Li^+ motion were derived as 0.11(2) and 0.40(1) eV for $Li_{0.925}Ta_{1.062}Al_{0.938}P_{3.16}O_{12+x}$ and $Li_{0.734}Ta_{1.187}Ca_{0.108}Al_{0.705}P_3O_{12}$, respectively – a relationship consistent with AC impedance studies. The difference in activation barrier values deduced from relaxometry was found to be significantly different to that derived from Li^+ jump rate against reciprocal temperature while retaining the relationship between compositions. This suggests the anisotropic nature of Li^+ diffusion are present in both NASICON materials, while keeping consistent that $Li_{0.734}Ta_{1.187}Ca_{0.108}Al_{0.705}P_3O_{12}$ has significantly slower Li^+ dynamics compared to that of the undoped composition.

Chapter 6 described a new family of Li^+ ion conductors of compositions $Li_{4.4}Al_{0.4}Ge_{0.6}S_4$ and $Li_{4.4}Al_{0.4}Sn_{0.6}S_4$.[2] NMR structural analysis complemented

the powder diffraction studies by identifying the AlS_4 tetrahedra and the three Li sites using in ^{27}Al and ^{6}Li NMR spectroscopy, respectively. ^{119}Sn MAS NMR on $Li_{4.4}Al_{0.4}Sn_{0.6}S_4$ showed a complex spectrum, showing the presence of at least 6 Sn environments. Individual assignments of these peaks are not trivial as these could arise from multiple possible local ordering of Li sites, disorder of the tetrahedron not detected in by diffraction methods and therefore may require other techniques such as DFT GIPAW calculations.

Li^+ dynamics of the $Li_{4.4}Al_{0.4}Ge_{0.6}S_4$ and $Li_{4.4}Al_{0.4}Sn_{0.6}S_4$ were studied using variable temperature ^{7}Li NMR. Line narrowing experiments showed the onset of motional narrowing was at a lower temperature in $Li_{4.4}Al_{0.4}Ge_{0.6}S_4$ compared to $Li_{4.4}Al_{0.4}Sn_{0.6}S_4$ and is therefore determined as the faster Li^+ dynamics, consistent with AC impedance spectroscopy. ^{7}Li NMR relaxometry study highlighted the 2D nature of Li^+ diffusion along the two-dimensional Li3 plane with $T_{1\rho}^{-1}$ values following the τ $\ln(1/\omega\tau)$ relationship at a single temperature. A relaxometry derived activation barrier seen in $Li_{4.4}Al_{0.4}Ge_{0.6}S_4$ was lower compared to $Li_{4.4}Al_{0.4}Sn_{0.6}S_4$ at 0.22(4) and 0.34(1) eV, respectively. The extracted Li^+ jump rates from line narrowing and relaxometry plotted in an Arrhenius fashion showed a very small activation barrier of 0.16(3) and 0.17(2) eV for $Li_{4.4}Al_{0.4}Ge_{0.6}S_4$ and $Li_{4.4}Al_{0.4}Sn_{0.6}S_4$, respectively. The value here determined for $Li_{4.4}Al_{0.4}Ge_{0.6}S_4$ is within error of the relaxometry derived value but differs by a factor of 2 for $Li_{4.4}Al_{0.4}Sn_{0.6}S_4$ which suggests the presence of a process with slower Li^+ dynamics. The jump rate Arrhenius plot derived values, however, are in agreement with values obtained from molecular dynamics calculations of Li^+ diffusion along the Li3 plane, consistent with the 2D nature of the diffusion process observed in relaxometry. This value is

smaller than those observed in $Li_{10}GeP_2S_{12}$ and its related family which have activation barriers of ~0.20 eV, highlighting the large potential of $Li_{4.4}Al_{0.4}Ge_{0.6}S_4$ and $Li_{4.4}Al_{0.4}Sn_{0.6}S_4$ for battery applications. This project was published in Chemistry of Materials in 2018, and consecutive research have been conducted within the research groups to further enhance the conductivity, to achieve a suitable material for application while retaining high stability against Li metal.

Overall, the solid state NMR spectroscopy study of five different new solid state Li^+ ion conductors of three distinct crystallographic families have been presented in this thesis. In each case, the local ordering of Li sites, unattainable experimentally by diffraction methods, were determined. Probing of Li^+ dynamics information over wide range of time scales from ns to s inaccessible by other experimental techniques were performed through the analysis of variable temperature NMR on ^6Li and ^7Li and proved invaluable to understanding the diffusion process. Improvements in the NMR studies could be made as common methods such as pulse-field gradient NMR spectroscopy to determine Li^+ diffusion constants at longer time scales were not performed due to the unavailability of a gradient probe, and with the use of automated equipment and scripts, variable temperature experiments could be recorded more efficiently.

Although none of the materials were able to obtain the target conductivity of 10^{-2} S cm^{-1} at room temperature by AC impedance, two of the crystallographic families were newly discovered and their activation energy to Li^+ diffusion probed my NMR were low, which opens many possibilities in the future. The conductivities of these materials could be improved further with

structural and chemical modifications to match or perhaps surpass the current best solid state Li^+ ion conductors known, though careful considerations would be required as by the significance of Ca^{2+} doping on the NASICON $Li_{0.734}Ta_{1.187}Ca_{0.108}Al_{0.705}P_3O_{12}$ where doping ultimately worsened Li^+ conductivity. In the case of $Li_{4.4}Al_{0.4}Ge_{0.6}S_4$, improvement of conductivity and barrier to Li^+ diffusion while retaining Li metal stability would revolutionise solid Li ion batteries, as this would allow Li metal to be used as an anode while retaining its crystal structure. For example, Si substitution on the Ge site in $Li_{10}GeP_2S_{12}$ showed a lower activation barrier and higher Li^+ ion conductivity,[3] so a similar approach could be taken. Solid state NMR will surely play a key role in realising that aim by understanding how chemical and structural modifications change the material's properties, assisting the development of methods and processes in achieving target materials.

References

1 A. B. Santibáñez-Mendieta, C. Didier, K. K. Inglis, A. J. Corkett, M. J. Pitcher, M. Zanella, J. F. Shin, L. M. Daniels, A. Rakhmatullin, M. Li, M. S. Dyer, J. B. Claridge, F. Blanc and M. J. Rosseinsky, *Chem. Mater.*, 2016, **28**, 7833–7851.

2 B. T. Leube, K. K. Inglis, E. J. Carrington, P. M. Sharp, J. F. Shin, A. R. Neale, T. D. Manning, M. J. Pitcher, L. J. Hardwick, M. S. Dyer, F. Blanc, J. B. Claridge and M. J. Rosseinsky, *Chem. Mater.*, 2018, **30**, 7183–7200.

3 A. Kuhn, O. Gerbig, C. Zhu, F. Falkenberg, J. Maier and B. V. Lotsch, *Phys. Chem. Chem. Phys.*, 2014, **16**, 14669–14674.